CMTM5 – a novel CNS myelin protein involved in preserving axonal integrity

Dissertation

for the award of the degree

“Doctor rerum naturalium”

of the Georg-August-Universität Göttingen

within the doctoral program Cellular and Molecular Physiology of the Brain

of the Georg-August University School of Science (GAUSS)

submitted by

Tobias Justus Ulrich Buscham

from Walsrode

Göttingen, 02.02.2022

Thesis Committee

Dr. Hauke B. Werner (1st Reviewer)

Department of Neurogenetics

Max-Planck-Institute for Multidisciplinary Sciences, Göttingen

Prof. Dr. Susann Boretius (2nd Reviewer)

Functional Imaging Laboratory

German Primate Center, Leibniz Institute for Primate Research, Göttingen

Prof. Dr. Wolfgang Brück

Chair of the Executive Board

Dean of the Medical Faculty

University Medicine Göttingen

Further members of the Examination Board

Prof. Dr. Ralf Heinrich

Department of Cellular Neurobiology

Georg-August University Göttingen

Prof. Dr. Christine Stadelmann-Nessler

Institute for Neuropathology

University Medicine Göttingen

Prof. Dr. Nicola Strenzke

Institute for Auditory Neuroscience

University Medicine Göttingen

Date of oral examination: 07.04.2022

“What day is it?” asked Pooh.

“It´s today.” squeaked Piglet.

“My favorite day.” said Pooh

-Winnie the Pooh (1926), A. A. Milne

Acknowledgements

What a journey this PhD and the associated projects have been, full of opportunities and challenges and great people along the way:

First, I would like to thank my supervisor Dr. Hauke B. Werner. Most importantly for me is that you enabled an environment in which I could grow personally and professionally during the last years, which I am very grateful for. If I find myself in the position of leading a team, I hope I can do it in the way you have done it over the past years that I enjoyed in the group.

I would like to thank the members of the "Werner Lab" for making my PhD an exceptional time in and outside of the lab, especially Sophie Siems, Ramona Jung, Vasiliki-Ilya Gargareta and Dr. Maria Eichel-Vogel. Here, I would also like to again thank Maria for being a great mentor and an inspiration in and outside the academic field (Outside the comfort zone is where the magic happens). Further, I would like to thank Anna Bretschneider for supporting me with all the mouse genotyping. A big thank you to Franziska Fries and Gurjit Kaur Theara for the work in this project. I learned a lot in the time I supervised you and really enjoyed the collaboration.

I want to thank Prof. Dr. Klaus-Armin Nave for the opportunity to learn and work on my projects in such a great environment as provided in the Neurogenetics department.

I would like to thank Prof. Dr. Susann Boretius and Prof. Dr. Wolfgang Brück for their commitment as members of my thesis advisory committee as well as Prof. Dr. Nicola Strenzke, Prof. Dr. Christine Stadelmann-Nessler and Prof. Dr. Ralf Heinrich for volunteering as my thesis examination committee.

I would like to thank all our collaborators for their contributions and support of the project and the publication: Dr. Maria Eichel-Vogel, Dr. Anna Steyer, Dr. Olaf Jahn, Prof. Dr. Nicola Strenzke, Rakshit Dardawal, Tor Rasmus Memhave, Sophie Siems, Dr. Christina Müller, Dr. Martin Meschkat, Dr. Ting Sun, Torben Ruhwedel, Dr. Wiebke Möbius, Prof. Dr. Eva-Maria Krämer-Albers, Prof. Dr. Susann Boretius and Prof. Dr. Klaus-Armin Nave.

The animal unit and transgenic facility is the backbone of our work. Therefore, I would like to thank our animal caretakers, especially Marion Peine and Sarah Schulze for their tremendous support over the years and the smooth collaboration. I further thank Dr. Ursula Fünfschilling for her help regarding transgenic mice as well as Dr. Sarah Kimmina and Dr. Anke Schräpler for their support concerning animal licenses and animal experiments.

I would like to thank Dr. Wiebke Möbius, Dr. Anna Steyer, Torben Ruhwedel (I hope the Bingo chart is not full yet) and Boguslawa Sadowski for all the insights and support in the world of electron microscopy.

I would like to thank Annette Fahrenholz and Uschi Kutzke for their great technical support. Further Dr. Kathrin Kusch and Ulli Bode for all their help regarding troubleshooting in questions related to cell culture and biochemistry and being such great colleagues inside the lab and great trainers outside the lab.

To the PhD community of the institute and especially the Neurogenetics department: one hopes to find such a great group of colleagues and friends again. Christin Kappert, Lena Spieth, Dr. Martin Meschkat, Dr. Tim Düking, Dr. Ting Sun, Dr. Swati Subramanian, Dr. Jan Seidel, Dr. Niklas Michel, Dr. Stefan Berghoff. Thank you for the great time, support and discussions!

I would like to thank Michaela Schmalstieg for all the help with the bureaucratic and administrative tasks along the way.

I had a great time working and learning from my PhDnet projects in association with the Planck Academy. For this I would like to thank Felipe Nathan de Oliveira, Viviane Münzing and especially Anne Grewlich-Gercke and Dr. Marta Porniece Kumar. I am curious and looking forward to see what develops out of our projects in the future.

I would like to thank my family for their support and interest in the project over the years. A big thanks to the “Rasselbande” aka all my lovely friends as well as Kathi for the constant support and lovely distractions in the past years and for sure in the future (“Was vor uns liegt sind nur unsere Fragen… ;)”).

Content

List of figures

Abbreviations

AD	Axial diffusivity
AEF	Axogliasome enriched fraction
APP	Amyloid-precursor-protein
ATP	Adenosine triphosphate
ATP1a1	ATPase NA+/K+ Transporting Subunit Alpha1
BAC	Bacterial artificial chromosome
BOS	Base of support
CAII	Carbonic anhydrase II
Cd107b/MAC3	Cluster of differentiation 107b
cKO	conditional knock-out
CMTM	Chemokine-like factor-like MARVEL transmembrane domain containing family
CNP	2´3´-cyclic nucleotide 3´phoshodiesterase
CNS	Central nervous system
CTRL	Control
Dhh	Desert hedgehog
dKO	double knock-out
EGFR	Epidermal growth factor receptor
et al.	and others
EV	Extracellular vesicle
ERG	Electroretinography
FA	Fractional anisotropy
FIB-SEM	Focused ion beam-scanning electron microscopy
GFAP	Glial fibrillary acidic protein
GLUT1	Glucose transporter 1
IBA1	Ionized calcium-binding adapter molecule 1
iKO	Inducible knock-out
KO	knock-out
MBP	Myelin basic protein

MD	Mean diffusivity
MOL	Mature/Myelinating oligodendrocyte
MPI_EM	Max-Planck Institute of Experimental Medicine
MRI	Magnetic resonance imaging
MRS	Magnetic resonance spectroscopy
mRNA	messenger RNA
MS	Multiple sclerosis
MT	Magnetization transfer
MTsat	Magnetization transfer saturation
NAD^+	Nicotinamide adenine dinucleotide
NMDAR	*N*-Methyl-D-aspartate receptor
NFO	Newly formed oligodendrocytes
n.s.	not significant
ON	Optic nerve
OPC	Oligodendrocyte precursor cell
PNS	Peripheral nervous system
PMD	Pelizaeus-Merzbacher disease
PLP	Myelin proteolipid protein 1
PCR	Polymerase chain reaction
RD	Radial diffusivity
RGC	Retinal ganglion cell
RNA	Ribonucleic acid
Rps13	Ribosomal protein S13
Rplp0	Ribosomal protein lateral stalk subunit P0
Slc16a1/MCT1	Solute carrier family 16 member 1
SIRT2	Sirtuin 2
sEV	synaptic extracellular vesicles
TEM	Transmission electron microscopy
UMAP	Uniform Manifold Approximation and Projection
VEP	Visually evoked potentials

Wld^{s}	Wallerian degeneration slow (mutation)

Compounds and methods related

ANOVA	Analysis of variance
BSA	Bovine serum albumin
cDNA	Complementary single stranded DNA
dATP	Desoxyadenosin triphosphate
dCTP	Desoxycytosine triphosphate
$_{dd}H_2O$	Double-distilled water/H_2O
dGTP	Desoxyguanine triphosphate
DIA	Data-independent acquisition
DNA	Deoxyribonucleic acid
dNTP	Deoxyribonucleoside triphosphate
DTT	Dithiothreitol
dTTP	Desoxythymine triphosphate
DWI	Double-weighted image
ECL	Enhanced chemiluminescence
FDR	False detection range
FASP	Filter-aided sample preparation
fl or flox	floxed (allele)
HBSS	Hank´s balanced salt solution
HRP	Horseradish peroxidase
IB	Immunoblot
IHC	Immunohistochemistry
K&S	Karlsson-Schultz fixative
LC-MS	Liquid chromatography-mass spectrometry
MS	Mass-spectrometry
PTI	Post Tamoxifen injection
PVDF	Polyvinylidene difluoride
PFA	Paraformaldehyde

qRT-PCR	quantitative real time PCR
rec	recombined (allele)
rel.	relative
RPE	Retinal pigment epithelium
SDS-PAGE	Sodium dodecyl sulfate-polyacrylamide gel electrophoresis
TBE	TRIS-Borat-EDTA buffer
TBS	Tris buffered saline
TEMED	N, N, N´, N´-Tetramethylethylendiamin
TFA	Trifluoroacetic acid
Wt	Wildtype

Quantities and units

[cd-s/m^2]	Candela per second per square meter
cm	Centimeter
cm/s	Centimeter/second
FC	Fold change
fmol/ µl	Femtomol per microliter
FPKM	Fragments per kilobase per million reads mapped
G	Gram
g	Centrifugal force
h	Hours
Hz	Hertz
kDA	kilo Dalton
kg	Kilogram
l	Liter
log_2FG	Log_2 fold change
M	Molar
mg	Milligram
mg/kg	Milligram per kilogram
min	minute(s)

ml	Milliliter
mM	millimolar
mo	month(s)
ms	Millisecond
m/s	meter per second
µM	Micromolar
µm	Micrometer
µl	Microliter
µV	Micro Volt
n	Number of experimental animals
nA	Nanoampere
ng	Nanogram
ng/µl	Nanogram per microliter
nl/min	Nanoliter per minute
nm	Nanometer
o/n	over-night
pA	Pikoampere
pmol/µl	Picomol per microliter
ppm	parts per million
p	p-value
rpm	revolutions per minute
U/µl	Units per microliter
UPLC	Ultra high-performance liquid chromatography
V	Volts
[v/v]	Volume per volume
[w/v]	Weight per volume
[w/w]	Weight per weight
°C	Degree Celsius
[#/mm^2]	Number per millimeter squared
%	Percent

1 Abstract

Myelination of axons in the nervous system facilitates rapid, saltatory signal propagation, accelerating nerve conduction speed manyfold. Additionally, myelinating glia support the long-term integrity of axons they enwrap. However, the relevance of many myelin proteins in these processes has remained elusive. In this study we identify CMTM5 (Chemokine-like factor-like MARVEL-transmembrane domain containing protein 5) as a low abundant but highly specific constituent of CNS myelin. We find that genetic disruption of the *Cmtm5*-gene in myelinating glial cells in mice does not alter myelin development or ultrastructure. However, deletion of *Cmtm5* in oligodendrocytes causes a progressive axonopathy in the CNS that is ameliorated by presence of the *Wld*^{s} mutation, suggesting a Wallerian-like mechanism of axon degeneration. Ablation of *Cmtm5* in myelinating Schwann cells of the PNS leads to a reduction in axonal diameters without evident axonal pathology, suggesting that CMTM5 serves different roles in the CNS and the PNS, respectively. Our results indicate that CMTM5 is not crucial for myelin biogenesis, structure, or composition but contributes to the functions of oligodendrocytes in maintaining axonal integrity in the CNS.

2 Introduction

2.1 Myelination of axons in the CNS and PNS

Myelination of axons by oligodendrocytes in the central and Schwann cells in the peripheral nervous system (CNS, PNS) facilitates diverse cell-cell interactions, which are critical for nervous system function in vertebrates (Figure 1A) (Nave and Werner, 2021). The selection process for axonal myelination differs between the CNS and PNS. Myelination of PNS axons is mainly regulated by neuregulin-1 type 3 expressed on the axonal surface as well as extracellular matrix constituents including laminins and collagens (Salzer, 2015). The diameter of an axon plays an important role as axons with a threshold diameter of 1 µm are selected for myelination by Schwann cells, while smaller axons are ensheathed by non-myelinating Schwann cells (Nave and Trapp, 2008; Nave and Werner, 2014).

In contrast to the PNS no main regulator of myelination is known for the CNS (Simons and Nave, 2016) and the axonal threshold diameter is less precise for the initiation of myelination by oligodendrocytes. Although larger fibers are more likely to be myelinated than smaller ones, axons as small as 0.2µm in diameter can potentially be myelinated (Lee et al., 2012). Neuronal activity was reported to play a role in myelination and elevated activity coincided with increased myelination of active neuronal networks (Gibson et al., 2014; Mitew et al., 2018). In contrast to Schwann cells in the PNS, oligodendrocytes depend less on external stimuli to initiate myelination and are rather repressed by axonal or glial surface molecules to regulate their myelination activity (Redmond et al., 2016; Schmandke et al., 2014).

Ultimately, the formation of lipid rich myelin sheaths in the CNS and PNS restricts action potential generation to the unmyelinated nodes of Ranvier (Hartline and Colman, 2007; Tasaki, 1939). This facilitates saltatory signal propagation along myelinated axons, which enhances conduction speed manyfold compared to unmyelinated axons of the same size (Figure 1B).

Myelination in vertebrates allowed for different adaptations of the nervous system. For example, the conduction speed could be enhanced without the need for axonal gigantism as observed in other species like squid (Figure 1B). However, the axonal diameter is also an important factor for signal propagation speed in vertebrates and myelinating glia cells were reported to alter axonal diameters, at least in the PNS, potentially finetuning neuronal networks (Eichel et al., 2020; Yin et al., 1998). Another measure to finetune signal propagation and enhance the precision of neuronal networks might be the reduction of ephaptic coupling (Figure 1C). Unmyelinated neighboring axons can be electrically coupled when active. Myelination may hinder electrical crosstalk between active

neighboring axons by providing a barrier for ion-flow and thus reduce ephaptic coupling (Nave and Werner, 2021).

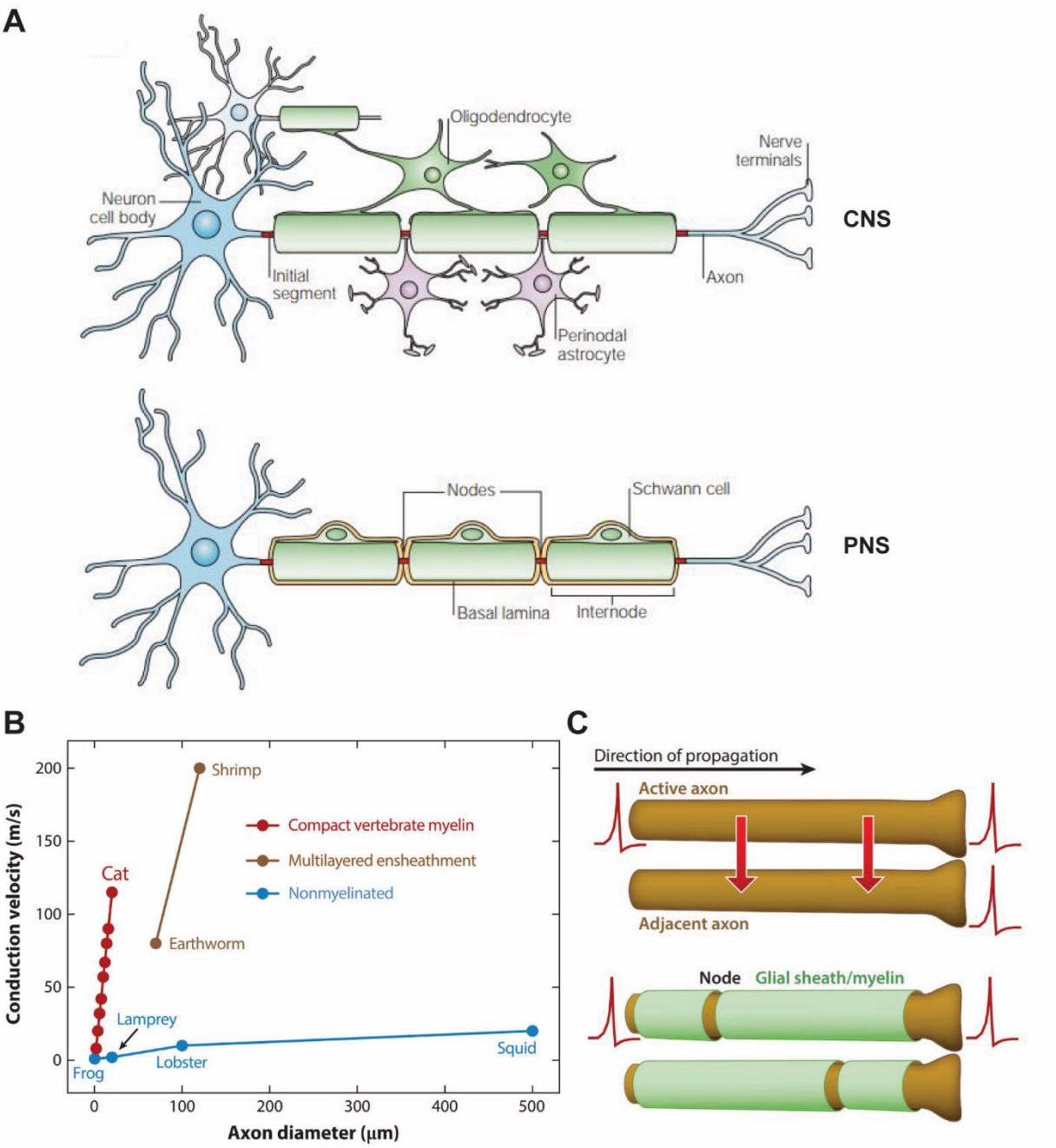

Figure 1: Myelination in the CNS and PNS and its role in the regulation of axonal signal propagation. (A) Oligodendrocytes and Schwann cells form myelin sheaths in the CNS and PNS respectively. While oligodendrocytes form multiple internodes on different axons, an individual Schwann cell only forms one internode around an axon in the PNS. In the CNS, nodes of Ranvier are contacted by Perinodal astrocytes. In the PNS, internodes are covered by a basal lamina. Figure from (Poliak and Peles, 2003). **(B)** Axonal conduction velocity in relation to their myelination status and axonal diameter in different species. Conduction velocity increases with axonal diameter but myelination with compacted myelin leads to a strong increase in conduction speed in vertebrates. Note that also multilayered, but not compacted ensheathment of axons can facilitate a steep increase in conduction velocity for example in shrimp. **(C)** Cartoon showing the principle of ephaptic coupling between non-myelinated and myelinated fibers. Myelin provides a barrier against electrical crosstalk of

neighboring fibers, reducing ephaptic coupling (Nave and Werner, 2021). Figure for **(B & C)** from (Nave and Werner, 2021).

In summary, myelination of axons in the CNS and PNS allowed for a steep increase in conduction velocity as well as different measures to finetune signaling in the nervous system of vertebrates. Of note, myelination in the CNS is not static after development and myelination patterns can be actively adapted by adding and removing individual myelin sheaths for example following training of motor skills (Williamson and Lyons, 2018). This adaptation is not only important with respect to the finetuning of neuronal networks, but also regarding the supportive function to the axon that myelinating glia can facilitate via their myelin sheaths.

2.2 Axonal support by oligodendrocytes

Neurons need a constant energy supply along the axon to perform action potential generation. In fact, much of the energy in the nervous system is consumed by Na/K-ATPases that keep the respective ion levels at a homeostatic level and allow for re-excitation of the axon (Attwell and Laughlin, 2001). Active transport or diffusion along the axon is relatively slow and it would take mitochondria or nutrients a long time travelling along the axons of spinal cord motor neurons even in smaller animals like mice (Maday et al., 2014).

Further, myelinated axons are secluded from the extracellular milieu by the multilayered, compact myelin sheath. Thus, tacking up metabolites from the extracellular space, astrocytes or endothelia might be difficult for longer myelinated stretches, especially in highly myelinated fiber tracts like the optic nerve where axons are myelinated almost over their entire length (Bélanger et al., 2011; Simons and Nave, 2016). It is thus not surprising that neurons rely on support from oligodendrocytes to meet their high energy demand along the axon.

Indeed, oligodendrocytes can respond to the activity of an axon they enwrap by shuttling metabolites to it via designated monocarboxylate transporters (Figure 2). This demonstrates, that oligodendrocytes support axons metabolically and that this process can be modulated according to the metabolic needs of the enwrapped axon (Fünfschilling et al., 2012; Y. Lee et al., 2012; Philips et al., 2021; Saab et al., 2016).

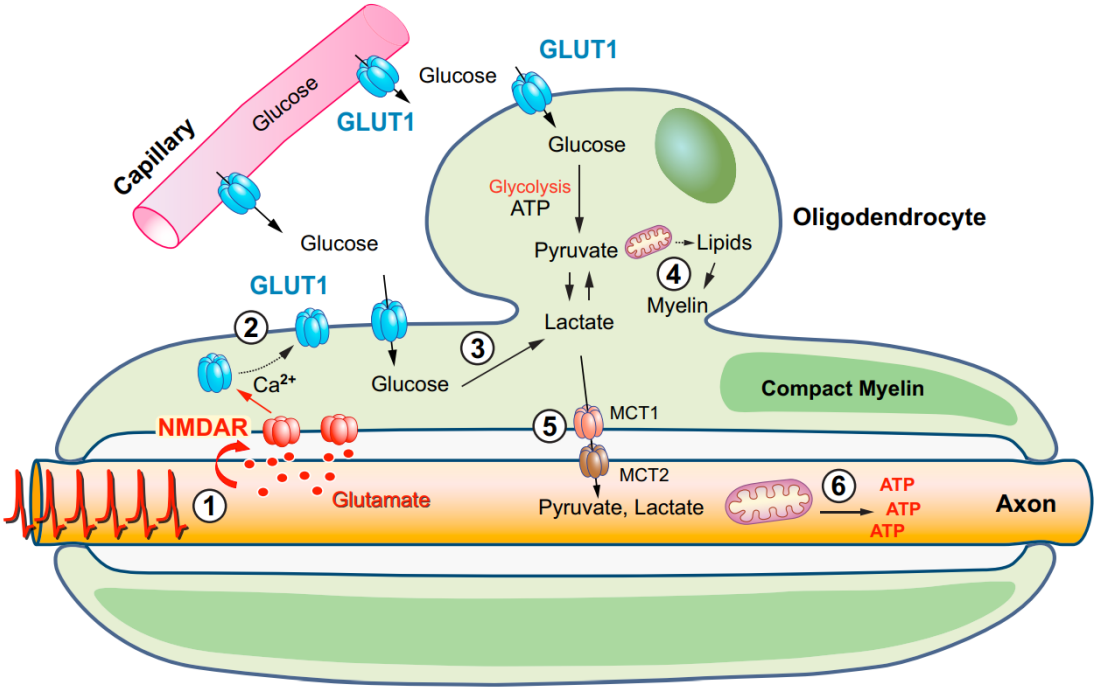

Figure 2: Scheme depicting a potential role of oligodendrocytes in the support of axons with metabolites. Hypothetical model in which oligodendrocytes support axons with metabolites following axonal activity. (1) Axonal activity leads to the release of glutamate which binds to NMDA receptors at the adaxonal myelin compartment. (2) This leads to an increased uptake of glucose via GLUT1 in oligodendrocytes which fuels glycolysis in oligodendrocytes (3 & 4). Lactate and pyruvate are then transported to the axonal compartment via MCTs to support mitochondrial ATP production in the axon (5 & 6). Figure from (Saab et al., 2016).

Additionally, oligodendrocytes support axons via the release of extracellular vesicles containing antioxidative proteins and other enzymes (Chamberlain et al., 2021; Frühbeis et al., 2020; Mukherjee et al., 2020) and are further able to modulate axonal transport (Edgar et al., 2004; Frühbeis et al., 2020).

Considering the susceptibility of axons to extracellular stress or energy deficiency as well as the different mechanism by which oligodendrocytes engage with axons and support their integrity, it is not surprising that disturbances of the axon-myelin unit or oligodendrocytes *per se* can cause detrimental effects for myelinated axons and thus impact nervous system function (Edgar et al., 2009; Griffiths I et al., 1998).

The significance of the axon-myelin unit becomes thus especially apparent under disease situations in humans or when its function is disturbed chemically or genetically in the respective animal models. For example, myelin pathologies in the CNS like Pelizaeus-Merzbacher disease (PMD) or multiple sclerosis (MS) are often associated with axonal degeneration and ultimately impaired nervous system function (Franklin et al., 2012; Stadelmann et al., 2019; Wolf et al., 2021).

Importantly though, re-establishing a functional axon-myelin unit by quick and efficient remyelination was shown to be beneficial and linked to a better outcome of axonal survival for example in a model of MS (Mei et al., 2016). This emphasizes, that fatal axon degeneration can be averted by support of oligodendrocytes, which is particularly important given the low regenerative capacity of mammalian CNS axons and neurons.

Combined, these findings emphasize the importance of a functional axon-myelin unit with regards to long-term preservation of axonal integrity and ultimately CNS function. Therefore, it is important to identify relevant molecules in the process of oligodendrocyte-axon signaling involved in supporting axonal integrity.

2.3 Identifying the function of novel CNS myelin proteins

Different pathways by which axons and oligodendrocytes interact are known, yet many of the underlying molecular mechanism of axonal support by oligodendrocytes remain obscure. Further, this process is even more complex considering that myelination and the myelin composition can be dynamic and change during development and aging (Williamson and Lyons, 2018). Myelination and myelin composition differs between white matter regions (currently unpublished proteomic data) and oligodendrocytes are heterogenous regarding their gene expression profiles (Dimou and Simons, 2017; van Bruggen et al., 2017). It is thus plausible to hypothesize that not only myelination *per se* is an adaptive process, but that this adaptation also includes the composition of the myelin sheaths itself, potentially being tailored to the specific needs of certain axonal sub populations.

To identify novel myelin candidates for characterization, mass spectrometric (MS) analysis of biochemically purified myelin or the axogliasome enriched fraction (AEF, contact point of the innermost myelin layer and the axonal membrane) proves a promising starting point. In fact, by proteomic analysis hundreds of different proteins have been identified in purified myelin, of which only few were analyzed in depth so far (Jahn et al., 2020). For example, the most abundant proteins in CNS myelin, proteolipid protein 1 (PLP), myelin basic protein (MBP) and 2´,3´-cyclic nucleotide 3´-phophodiesterase (CNP) are studied intensely since decades (Edgar et al., 2009, 2004; Griffiths I et al., 1998; Roach et al., 1985; Rosenbluth, 1980). However, knowledge about the functional relevance of the majority of proteins in myelin remains limited, especially for those of low abundance. This becomes even more clear with recent advancements in MS workflows, peptide detection and annotation, allowing for the identification of hundreds of new low abundant candidates over the past years. One interesting example are members of the chemokine-like-factor-like MARVEL-transmembrane

containing protein family (CMTM), namely CMTM5 and CMTM6, which show a generally low abundance but a high enrichment in myelin or the AEF, respectively (Eichel et al., 2020). Further, a suggested chemokine-like motif could imply the potential for signaling capabilities (Han et al., 2003). Interestingly, the functional relevance of CMTM6 in the peripheral nervous system was recently shown (Eichel et al., 2020).

2.4 The CMTM Protein family and its relevance for nervous system function

The CMTM family consists of eight members (Han et al., 2003) which are mainly known in the context of mediating cancer immunity (Burr et al., 2017; Mezzadra et al., 2017; Shao et al., 2007; Xiao et al., 2015) and male fertility (Fujihara et al., 2018; Liu et al., 2019). Further, most insights about CMTMs come from correlative cancer studies or *in vitro* work with cancer cell lines but *in vivo* studies assessing the functions of CMTMs remain limited, especially in the context of the nervous system.

Intriguingly, expression of CMTM6 by Schwann cells regulates axonal diameters in the PNS and thus demonstrated the principal involvement of at least one CMTM protein in the function of the nervous system *in vivo* (Eichel et al., 2020). The study showed that Schwann cells expressing CMTM6 restrict axonal diameters via a yet unknown mechanism, a newly identified function of myelinating glial cells.

Following these findings, we tested whether we can also identify CMTM proteins expressed by oligodendrocytes potentially fulfilling a similar function in the central nervous system. We found only CMTM5 to be expressed by oligodendrocytes in the CNS (Figure 3A, B) where it shows a high specificity for cells of the oligodendrocyte lineage (Zhang et al., 2014). Of note, CMTM5 was detected in the PNS before: *Cmtm5* mRNA expression was shown in the sciatic nerve as well as Schwann cells and CMTM5 protein abundance in PNS myelin was also reported (Eichel et al., 2020; Gerber et al., 2021; Patzig et al., 2011).

In the CNS, CMTM5 was used as a marker for oligodendrocytes before, where its gene promoter was used to drive BAC-Cre (Bacterial artificial chromosome) expression and label oligodendrocytes (Gong et al., 2007). Further, CMTM5 is expressed by oligodendrocytes of mice and humans (Figure 3C, F) (Jäkel et al., 2019; Zhou et al., 2020) and was also mass-spectrometrically identified in purified CNS myelin before (Jahn et al., 2020). Additionally, we identified CMTM5 in myelin derived from wildtype mice and non-diseased humans (Fig 3G) and found the abundance to be roughly equal between the two species (Gargareta et al., 2022).

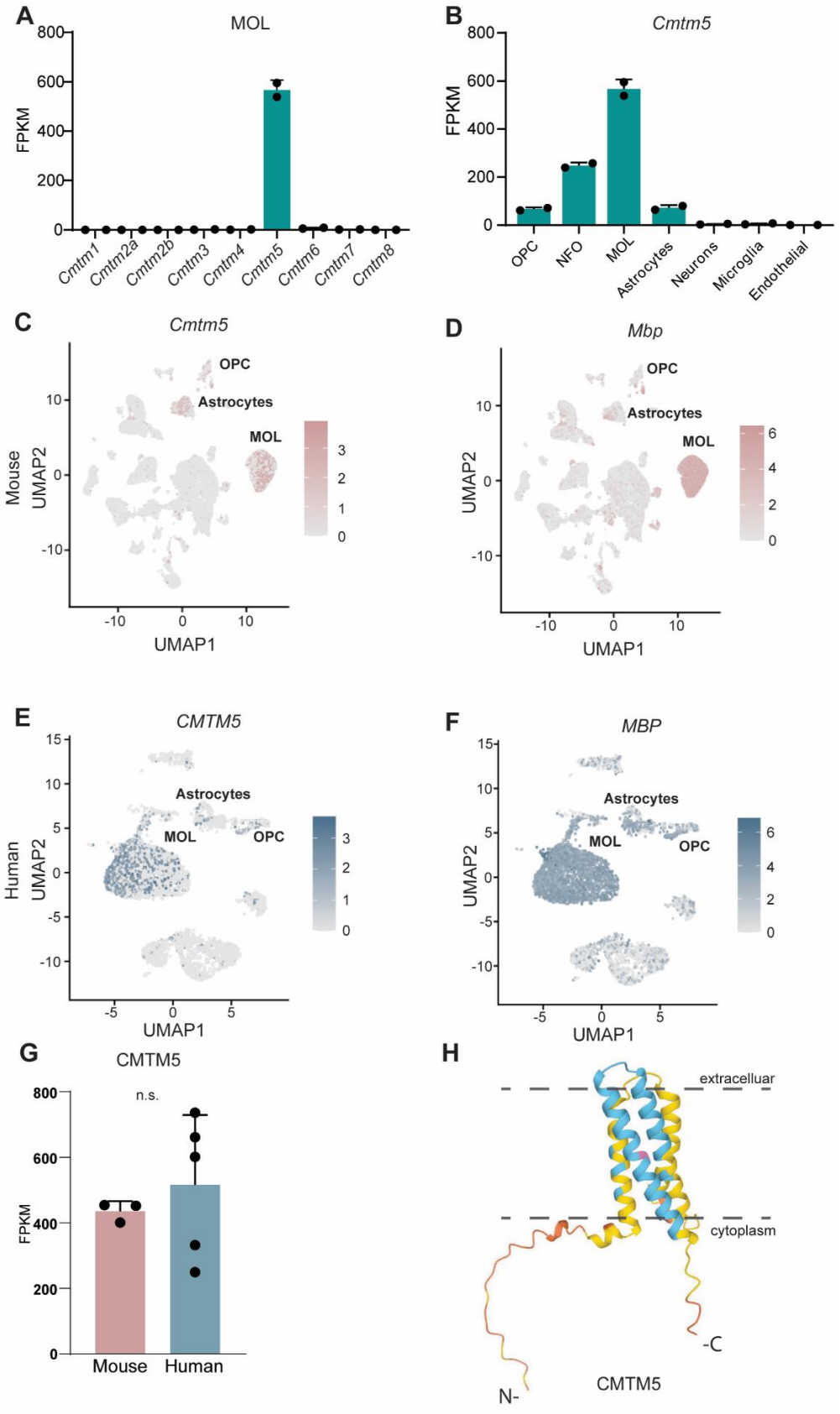

Figure 3: *Cmtm5* mRNA is expressed in mature oligodendrocytes of mice and humans. (A, B) Abundance of *Cmtm5* mRNA according to bulk RNAseq data of cells immunopanned from mouse cortices (Zhang et al., 2014). Note that among all members of the CMTM family, only *Cmtm5* mRNA is considerably expressed in MOL **(A)**.

Increasing *Cmtm5* mRNA expression coincides with maturation of cells of the oligodendrocyte lineage **(B)**. OPC, oligodendrocyte precursor cells; NFO, newly formed oligodendrocyte; MOL, Mature oligodendrocytes; FPKM, fragments per kilobase per million mapped fragments. Data represented as mean ± SEM. **(C, D)** Uniform manifold approximation and projection (UMAP) feature plots of scRNAseq data derived from a previously published dataset (Zhou et al., 2020) shows enriched expression of *Cmtm5* mRNA in mature oligodendrocytes (MOL) of mice **(C)**. *Mbp* serves as marker gene for MOL in mice **(D)**. **(E, F)** UMAP feature plots of scRNAseq data derived from a previously published dataset (Jäkel et al., 2019) shows enriched expression of *CMTM5* mRNA in mature oligodendrocytes (MOL) of the white matter in disease-unaffected human control samples **(E)**. *MBP* serves a marker gene for human MOL **(F)**. **(G)** Mass spectrometric analysis of brain myelin derived from wildtype C57Bl/6N mice and non-diseased humans. Abundance of CMTM5 is relatively similar in both species. Data from (Gargareta et al., 2022). **(H)** Structure prediction of CMTM5 in mice according to AlphaFold2 (Jumper et al., 2021). Blue colors indicate high confidence of the predicted structure while yellow and red indicate low confidence. Dashed lines indicate hypothetical membrane locations.

We were thus intrigued to assess the function of CMTM5 in the CNS. Structure prediction of CMTM5 indicates 4 transmembrane domains with 2 short extracellular domains and N- and C-terminal sequences protruding into the cytoplasm (Figure 3H) (Jumper et al., 2021) and despite its name, no chemokine-like sequence motif is apparent that could be involved in direct cell-cell signaling.

However, previous studies showed that at least some members of the CMTM protein family are capable to stabilize the abundance of key signaling proteins at the cell surface and facilitate cell-cell interactions (Burr et al., 2017; Mezzadra et al., 2017; Zheng et al., 2020). Thus, the signaling capabilities of CMTM5 could also be mediated by indirect effects rather than direct cell-cell interactions via a chemokine-like motif.

As other members of the CMTM protein family, CMTM5 was reported to be involved in mediating cancer immunity and its absence in tumors or cancer cells was correlated to worse disease outcomes and increased metastasis (Shao et al., 2007; Xiao et al., 2015). A disease modifying effect of CMTM5 via the epidermal growth factor receptor 1 (EGFR) was suggested, however, the exact mechanism by which CMTM5 could mediate its functions remains elusive (Yuan et al., 2020).

This study presents the first assessment of the functional relevance of CMTM5 *in vivo*, focusing on myelinating glial cells in the CNS.

2.5 Aim of the study

We aim to identify myelin proteins with a plausible function in glia-axon signaling in the nervous system. We here follow the recent discovery that one member of the CMTM protein family, CMTM6, is involved in the function of Schwann cells to restrict axonal calibers. In the present study we will assess the functional relevance of CMTM5, another member of the CMTM protein family. We will

determine whether CMTM5 has a role in the CNS similar to that of CMTM6 in the PNS and further analyze its relevance for glia-axon signaling.

To achieve this, we will first establish CMTM5 as a novel CNS myelin protein in wildtype mice by:

1. Confirming its abundance in biochemically purified CNS myelin from wildtype mice
2. Analyzing its expression dynamics during early postnatal brain development in comparison to known myelin proteins
3. Confirming its localization in myelin sheaths in the CNS using confocal microscopy.

To further investigate the functional relevance of CMTM5 in the CNS we will create mouse lines in which *Cmtm5* is conditionally deleted in oligodendrocytes using $Cnp^{Cre/Wt}$ (Lappe-Siefke et al., 2003), as well as $Plp^{CreERT2}$ driver mice (Leone et al., 2003) for deletion of CMTM5 in oligodendrocytes of adult animals to assess its function independent from brain development. We will confirm the successful deletion of CMTM5 using biochemical methods.

We follow the hypothesis that CMTM5 might be involved in regulating of axonal diameters. We will therefor analyze axonal morphology and diameters using transmission electron microscopy (TEM). In case we observe structural or pathological abnormalities, we will further assess them using TEM as well as focused ion beam-scanning electron microscopy (FIB-SEM) for an in-depth characterization and 3D reconstruction of relevant profiles.

In case deletion of CMTM5 causes a neuropathology, we will evaluate its onset and progression using the appropriate markers in immunohistochemistry stainings.

We will assess whether deletion of CMTM5 alters the myelin proteome using label-free quantitative mass spectrometry, analyze the influence of CMTM5 on myelination using TEM and FIB-SEM for a detailed analyzes on a microscopic scale, and perform Magnetic Resonance Imaging (MRI) of mouse brains to determine the effect of CMTM5 deletion on white matter volume, structure and integrity.

In case deletion of *Cmtm5* causes relevant changes in myelin or axonal integrity, we will further analyze the consequences on a functional level using appropriate behavioral tests and nerve conduction velocity measurements.

Together, we expect that our analysis will allow deciphering the functional relevance of the expression of CMTM5 by myelinating oligodendrocytes in the CNS.

3 Material and Methods

3.1 Material

3.1.1 Chemicals

All Chemicals and laboratory materials were purchased from BioRad (Munich, Germany), Eppendorf (Hamburg, Germany), Sigma-Aldrich GmbH (Munich, Germany), Merck KGaA (Darmstadt, Germany), Sartorius (Göttingen, Germany) and SERVA (Heidelberg, Germany) unless stated otherwise.

3.1.2 Genotyping PCR buffers and reagents

Description	Content	
Digestion buffers	50 mM NaOH Tris/HCl pH 8.0	67mM
10 mM dNTP (50x stock)	dATP dCTP dGTP dTTP 200 µM final concentration in a PCR reaction	2.5 mM 2.5 mM 2.5 mM 2.5 mM

Description	Manufacturer
GoTaq DNA polymerase	Promega (Mannheim, Germany)
GoTaq buffer 5x	Promega (Mannheim, Germany)
dNTPs	Boehringer GmbH (Mannheim, Germany)
GeneRuler 100bp DNA ladder	Thermo Fisher Scientific (St. Leon-Rot, Germany)

3.1.3 Genotyping primers

Description	Number	Sequence
Cmtm5 Genotyping	34179	5'- AGTAGTGGCCCATTGCCATC-3'
	34180	5'- TGGTTAGGGGGCTCCTCTTC -3'
	32002	5'- GAGCTCAGACCATAACTTCG -3'
$Cnp^{Cre/Wt}$	2016	5'- GCCTTCAAACTGTCCATCTC -3'

	4192	5’- CAGGGTGTTATAAGCAATCCC -3’
	4193	5’- CCTGGAAAATGCTTCTGTCCG -3’
	7315	5’- CCCAGCCCTTTTATTACCAC -3’
Plp^{CreERT2}	10099	5’- TGGACAGCTGGGACAAAGTAAGC -3’
	7963	5’- CGTTGCATCGACCGGTAATGCAGGC -3’
Wlds	36307	5’- CGTTGGCTCTAAGGACAGCAC -3’
	36308	5’- CTGCAGCCCCCACCCCTT -3’
Cmtm6	33516	5’- GCTGCTGTTT CTCATTGCTG -3’
	33517	5’- TGTGTCAAAC GCTAAGACTCAG -3’
Cmtm6 Recombined	33516	5’- GCTGCTGTTT CTCATTGCTG -3’
	32202	5’- GAGCTCAGAC CATAACTTCG -3’
Dhh-Cre recombinase	10967	5’- CCTGCGGAGATGCCCAATTG -3’
	15793	5’- CAGCCCGGACCGACGATGAA -3’

3.1.4 Genotyping PCRs

PCR	**Content**	**Amount (µl/sample)**	**Expected bandsize**
Cmtm5 Genotyping	Go-Taq buffer (5x)	4.2	Flox – 626 bp
	dNTP (2nM)	2.1	Wt- 437 bp
	Primer 34179	0.75	Rec- 313 bp
	Primer 34180	0.5	
	Primer 32002	0.5	
	Primer		
	GoTaq DNA polymerase	0.07	
	$_{dd}H_2O$	11.88	
Cnp$^{Cre/Wt}$	Go-Taq buffer (5x)	4.2	Wt- 700 bp
	dNTP (2nM)	2.1	*Cre* – 350bp
	Primer 2016	1	
	Primer 4192	0.3	
	Primer 4193	0.3	
	Primer 7315	1	
	GoTaq DNA polymerase	0.07	
	$_{dd}H_2O$	11.03	
Plp^{CreERT2}	Go-Taq buffer (5x)	4.2	*Cre* positive – 250 bp
	dNTP (2nM)	2.1	
	Primer 10099	0.2	
	Primer 7963	0.2	
	GoTaq DNA polymerase	0.07	
	$_{dd}H_2O$	13.4	

Wlds	Go-Taq buffer (5x)	4.2	*Wlds* – 182 bp
	dNTP (2nM)	2.1	
	Primer 36307	0.5	
	Primer 36308	0.5	
	GoTaq DNA polymerase	0.07	
	$_{dd}H_2O$	12.63	
Cmtm6	Go-Taq buffer (5x)	4.2	Flox – 450 bp
	dNTP (2nM)	2.1	Wt - 292 bp
	Primer 33516	0.5	
	Primer 33517	0.5	
	GoTaq DNA polymerase	0.07	
	$_{dd}H_2O$	12.63	
Cmtm6 Recombined	Go-Taq buffer (5x)	4.2	Rec – 350 bp
	dNTP (2nM)	2.1	
	Primer 33516	0.5	
	Primer 32202	0.5	
	GoTaq DNA polymerase	0.07	
	$_{dd}H_2O$	12.63	
Dhh-Cre recombinase	Go-Taq buffer (5x)	4.2	*Cre* – 400 bp
	dNTP (2nM)	2.1	
	Primer 10967	0.5	
	Primer 15793	0.5	
	GoTaq DNA polymerase	0.07	
	$_{dd}H_2O$	12.63	

3.1.5 Primer for quantitative real-time PCR

Gene	Direction	Sequence
Cmtm5	Forward	5´-TTC CTG TCT TCC CTC AAA GG -3´
	Reverse	5´-GCC GRG AAG CAA ATG AAG AT -3´
Slc16a1/Mct1	Forward	5´-GGA TAT CAT CTA TAA TGT TGG CTG TC -3´
	Reverse	5´-TGA GAG CCA GAC CCA AGC -3´
Rps13	Forward	5´-CGA AAG CAC CTT GAG AGG AA -3´
	Reverse	5´-TTC CAA TTA GGT GGG AGC AC -3´
Rplp0	Forward	5´-GAT GCC CAG GGA AGA CAG -3´
	Reverse	5´-ACA ATG AAG CAT TTT GGA TAA TCA -3´

3.1.6 SDS PAGE and Immunoblot

Description	Content	
10x Tris-buffered saline (TBS)	Tris/HCl, pH 7.5	500 mM
	NaCl	1.5 M
4x SDS sample buffer	Glycerol	40% [w/v]
	Tris/HCl, pH 6.8	240 mM
	SDS	8% [w/v]
	Bromophenol blue	0.04% [w/v]
SDS separating gel	Acrylamid/Bisacrylamid 29:1	10/12/15% [v/v]
	Tris/HCl pH 8.8	0.4 M
	SDS	0.1% [w/v]
	APS	0.03% [w/v]
	TEMED	0.08% [v/v]
SDS stacking gel	Acrylamid/Bisacrylamid 29:1	10/12/15% [v/v]
	Tris/HCl pH 8.8	0.4 M
	SDS	0.1% [w/v]
	APS	0.03% [w/v]
	TEMED	0.08% [v/v]
10x SDS running buffer (Laemmli buffer)	Tris/Cl	250 mM
	Glycine	1.92 M
	SDS	1% [w/v]
SDS transfer buffer	Tris base	96 mM
	Glycine	78 mM
	Methanol	10% [v/v]
20x Tris buffered saline (TBS)	Tris/HCl, pH 7.4	1 M
	NaCl	3 M
1x TBS with Tween-20 (TBST)	Tris/HCl, pH 7.4-7.6	50 mM
	NaCl	150 mM
	Tween-20	0.05% [v/v]
Blocking buffer	nonfat dry milk powder in 1x TBST	5% [w/v]

Description	Manufacturer
Complete Mini Protease inhibitor	Roche Diagnostics GmbH (Mannheim, Germany)
PageRuler^{TM} Plus Prestained Protein Ladder	Thermo Fisher Scientific (St. Leon-Rot, Germany)
PVDF Membrane Amersham Hybond P0.45µm	GE Healthcare Life Science (Chicago, USA)

3.1.7 Perfusion and fixation solutions

Description	Content	
Avertin	Tribromethanol 99%	2% [w/v]
	Amylalkohol	2% [v/v]
	Mixed at 40°C for 30 minutes while stirring and subsequently filtered (pore size 0.45µm/m, Nalgene, Sigma-Aldrich Gmbh, Taufkirchen, Germany, Stored at -20°C	
0.2 M Phosphate buffer	Sodiumdihydrogenphophate (NaH_2PO_4)	0.36% [w/v]
	di-Sodiumhydrogenphosphate (Na_2HPO_4)	3.1% [w/v]
	Sodium Chloride (NaCl)	1% [w/v]
	Solubilized in 1l $_{dd}H_2O$	
16% Paraformaldehyde (PFA)	PFA	16% [w/v]
	NaOH	5N
	PFA cooked at 65°C until dissolved, NaOH added until solution went clear. Solution was filtered and stored at -20°C	
4% Paraformaldehyde (PFA)	PFA	16% [w/v]
	Phosphate buffer	0.1 M
Karlsson-Schultz fixative (K&S)	PFA	16% [w/v]
	Glutaraldehyde	2.5% [w/v]
	Phosphate buffer	0.1 M

3.1.8 Immunohistochemistry

Description	Content	
PBS, Phosphate buffered saline (0.2 M, PH 7.2	NaCl	1.7 M
	KCl	34 mM
	Na_2HPO_4 x 2 H_2O	40 mM
	K_2HPO_4	18 mM
	pH 7.2 with 1 N NaOH	
Permeabilization solution	Triton X-100	2% [v/v]
	In PBS	
Citrat Buffer (0.01 M, pH 6.0)	Citric acid ($C_6H_8O_7$ x H_2O)	1.8 mM
	Sodium citrate ($C_6H_5O_7Na_3$ x $2H_2O$)	8.2 mM
Tris-Buffer (0.05 M, pH 7.6)	Tris/HCl, pH 7.6	50 mM
	Sodium chloride (NaCl)	0.9% [w/v]
Tris-Buffer + 2% Skim Milk	Skim Milk powder (Frema)	2% [w/v]
	In 0.05 M Tris-Buffer	
Mayer´s haematoxylin solution	Haematoxylin	0.1% [w/v]
	Sodium iodate	0.02% [w/v]
	Potassium aluminium sulphate ($K_2AL_2(SO_4)_4$ x 24 H_2O) 5% [w/v]	
	Chloralhydrate	5% [w/v]
	Citric acid	0.1% [w/v]
PBS/BSA	Sodiumdihydrogenphosphate (NaH_2PO_4)	0.04 M
	di-Sodiumhydrogenphosphate (Na_2HPO_4)	0.16 M
	Sodium chloride (NaCl)	1.8% [w/v]
	Bovine serum albumin (BSA)	1.0% [w/v]
Scott´s solution	Potassiumhydrogencarbonate	0.2% [w/v]
	Magnesium sulphate	2% [w/v]

Description	Manufacturer
Eukitt	Kindler (Freiburg, Germany)
Aqua-Poly/Mount	Polysciences (Eppelheim, Germany)
Dako-Antibody diluent	Dako (Carpintería, USA)

3.1.9 Electron microscopy

Description	Content	
Epon	171.3g Glycidether 100 115g DDSA (Dodecenyl succinic anhydride) 89g MNA (Methyl nadic anhydride) Are mixed using a magnet stirrer for 10 minutes and then 6.5 ml DMP-30 Are added and mixed using magnet stirrer for another 20 minutes	
Methylene Blue	Na-tetraborat (Borax) Methylenblau	1% [w/v] 1% [w/v]
Azure II	Azure II	1% [w/v]
Methylene blue – Azure II Staining solution	Methylene blue Azure II Freshly prepared before use	50% [v/v] 50% [v/v]
Contrasting solution	UranyLess (Science Services, Munich, Germany)	

3.1.10 Assays & Kits

Immunohistochemistry for Paraffin sections

Description	Manufacturer, Catalog number #
DAB Zytomed Kit	Zytomed System GmbH (Berlin, Germany); Cat# DAB057
LSAB2 Kit	DAKO (Hamburg, Germany); Cat# K0609
Vector Elite ABC Kit	Vector Labs (Lörrach, Germany); Cat# PK-6100
DC Protein Assay (Lowry)	Bio-Rad (Munich, Germany); Cat# 5000111
Western Lightning® Plus-ECL	Perkin Elmer (Waltham, USA); Cat# NEL105001EA
RNA Purification “RNeasy mini prep”	Qiagen (Portland, USA); Cat#74104

3.1.11 Antibodies

3.1.11.1 Custom CMTM5 Antibodies

Two CMTM5 antibodies were newly developed and ordered from Proteintech (Manchester, United Kingdoms) and Pineda (Berlin, Germany). Antibodies were raised in 2-3 rabbits against the C-terminal domain of CMTM5 (Proteintech: YRTELMPSTTEGD; Pineda: CAFKIYRTELMPSTTEGDQQ). Antibody sera were validated using control and CMTM5 knock-out samples in immunoblot and IHC experiments.

3.1.11.2 Further antibodies used

Table 1: Primary Antibodies

Antigen	Host species	Method & dilution	Vendor & Catalog #
α-APP	Mouse	IHC 1:1000	Chemicon (#MAB348)
α-ATP1a1	Mouse	IB 1:5000	Abcam (#ab7671)
α-CAII	Rabbit	IB 1:500, IHC 1:300	Said Gandhour, Strasbourg, France;
α-CD9	Rat	IB 1:1000	BD (KMC8, #940200)
α-CD81	Mouse	IB 1:1000	Santa Cruz (#sc-166029)
α-CMTM5	Rabbit	IB 1:1000, IHC 1:200	Proteintech, Pineda (Custom made)
α-CNP	Mouse	IB 1:1000	Sigma Aldrich (#SAB1405637)
α-GFAP	Mouse	IHC 1:200	Novo Castra (#NCL-L-GFAP-GA5)
α-IBA1	Goat	IHC 1:1000	abcam (#ab5076)
α-MAC3	Rat	IHC 1:400	Pharmingen (#553322)
α-MCT1/Slc16a1	Rabbit	IB 1:1000	Kathrin Kusch, Göttingen, Germany
α-MVP	Rabbit	IB 1:1000	abcam (#ab97311)
α-PLP	Rabbit	IB 1:2000	Clone A431, (Jung et al., 1996)
α-PLP	Rat	IB 1:1000	Clone aa3
α-RBPMS	Guinea Pig	IHC 1:300	Sigma Aldrich (#ABN1376)
α-SIRT2	Rabbit	IB 1:500	abcam (#ab67299)
α-TUJ1	Mouse	IHC 1:1000	Covance (#MMS-435P)
α-SMI31	Mouse	IB 1:500	Covance (# SMI31P)
α-SMI32	Mouse	IB 1:500	Covance (# SMI32-P)

Table 2: Secondary Antibodies

Antigen	Host species	Method & dilution	Vendor & Catalog #
α-mouse HRP	Goat	IB 1:10000	Dianova (# 115-03-003)
α-rabbit HRP	Goat	IB 1:10000	Dianova (# 111-035-003)
α-rat HRP	Goat	IB 1:10000	Dianova (# SEC-183466)
α-rabbit Alexa555	Donkey	IHC 1:1000	Dianova (#SBA-3030-32)
α-guinea pig Alexa555	Donkey	IHC 1:1000	Dianova
α-mouse STAR RED	Goat	IHC 1:200	abberior (# STRED-1001-500UG)
α-rabbit STAR ORANGE	Goat	IHC 1:200	abberior (# STORANGE-1002-500UG)

3.1.12 Software

Decription	Manufacturer
GraphPad Prism 8	GraphPad Software, Inc.
Fiji/ImageJ	Schindelin et al., 2012
LAS X	Leica
IMOD v 4.9.12	University of Colorado
Zen 1.0	Zeiss
Adobe Photoshop	Adobe
Itk-SNAP 3.8.0	University of Pennsylvania
CatWalk XT 10.6	Noldus
Viewer2	Biobserve
Excel 2016	Microsoft
Matlab (v 2019b)	The Mathworks, Inc

3.1.14 Mouse lines

Line/Genotype	Description	Reference/Origin
Cmtm5$^{fl/fl}$	Mice carrying the *Cmtm5*$^{tm1a(KOMP)Wtsi}$ allele	The Mouse Genetics Project (Wellcome Trust Sanger Institute, Hinxton, UK)
Cnp$^{Cre/Wt}$	Mice expressing *Cre* under the *Cnp* promoter	Lappe-Siefke et al., 2003
Cmtm5$^{fl/fl}$**Cnp*$^{Cre/Wt}$	Conditional deletion of Cmtm5 in oligodendrocytes and Schwann cells (also termed *Cmtm5* cKO)	This study
Plp^{CreERT2}	Mice expressing and inducible *Cre* driver under the *Plp* promoter	Leone et al., 2003
Cmtm5$^{fl/fl}$** Plp*^{CreERT2}	Inducible knock-out of *Cmtm5* in oligodendrocytes following Tamoxifen injection (also termed *Cmtm5* iKO)	This Study
Cmtm5$^{-/-}$	Constitutive knock-out of *Cmtm5* following germline recombination	This Study
Wlds	Mice carrying the Wallerian degeneration slow "*Wlds*" mutation	Coleman et al., 2001
Cmtm5$^{-/-}$**Wlds*	Mice lacking *Cmtm5* and carry the *Wlds* mutation	This Study
Cmtm6$^{fl/fl}$	Mice with floxed *Cmtm6* allele	Eichel et al., 2020
Dhh^{Cre}	Mice expressing *Cre* under the *Dhh* promoter	Jaegle et al., 2003
Cmtm5$^{fl/fl}$**Cmtm6*$^{fl/fl}$**Dhh*^{Cre}	Conditional double knock-out of *Cmtm5* and *Cmtm6* in Schwann cells	This Study

3.2 Methods

3.2.1 Experimental animals

Mice were bred and kept in the mouse facility of the Max Planck Institute of Experimental medicine. 3-5 mice were housed per cage in a 12-hour dark/light cycle. Animals had access to food and water ad libitum. Experimental mutant mice were analyzed with littermate controls as far as possible. Mice were sacrificed by cervical dislocation or perfusion using anesthetics. All animal experiments were performed in accordance with the German animal protection law (TierSchG) and approved by the Niedersächsisches Landesamt für Verbraucherschutz und Lebensmittelsicherheit (LAVES) under license 33.19-42502-04-15/1833 and 33.8-42502-04-19/3172.

3.2.1.1 Generation of conditional and constitutive *Cmtm5* knock-out mice lines

Frozen sperm of mice carrying the 'knockout-first´-allele of the *Cmtm5* gene (C57BL/6N-A^{tm1Brd} *Cmtm5*$^{tm1a(KOMP)Wtsi}$*/Wtsi*) was acquired from The Mouse Genetics Project (Wellcome Trust Sanger Institute, Hinxton, UK). *Cmtm5*$^{tm1a(KOMP)Wtsi}$ mice were generated by the transgene facility of the Max Planck Institute of Experimental Medicine (Göttingen, Germany) by *in vitro* fertilization using standard procedures. The LacZ/neo cassette was deleted by crossbreeding these mice with *Gt(ROSA)26Sor*$^{tm1(FLP1)Dym}$ mice expressing flippase (Farley et al., 2000) yielding mice heterozygous for the floxed *Cmtm5* allele (*Cmtm5*$^{tm1c(KOMP)Wtsi}$ mice, also termed *Cmtm5*$^{fl/+}$) which were bred to homozygosity. To delete *Cmtm5* in oligodendrocytes, *Cmtm5*$^{fl/fl}$ mice were crossbred with mice expressing *Cre* under the *Cnp* promoter (*Cnp1*$^{tm(cre\ puro)Kan}$ mice, also termed *Cnp*$^{Cre/WT}$; Lappe-Siefke et al., 2003) yielding *Cmtm5*$^{fl/fl}$**Cnp*$^{Cre/WT}$ mice (also termed *Cmtm5* cKO). In experiments assessing *Cmtm5* cKO mice, *Cmtm5*$^{fl/fl}$ mice served as controls.

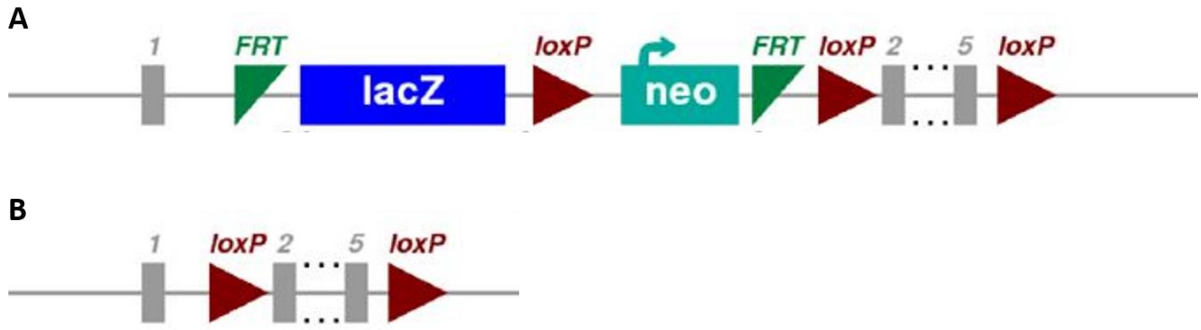

Figure 4: The *Cmtm5* gene construct. (A) Exons 2-5 of *Cmtm5* are flanked by loxP sites, additionally the construct contains a LacZ/neo cassette flanked by FRT recombination sites. **(B)** Breeding with mice expressing the flippase

recombinase leads to deletion of the LacZ/neo cassette. Mice with the floxed *Cmtm5* allele were crossbred with mice expressing the Cre-recombinase under the *Cnp* promotor ($Cnp^{Cre/WT}$) to delete *Cmtm5* in myelinating glia cells.

To analyze CMTM5 function independent of *Cnp* heterozygosity we also created a constitutive *Cmtm5* knock-out mouse. Mice with a body wide deletion of *Cmtm5* emerged via sporadic germline recombination in $Cmtm5^{fl/fl}$*$Cnp^{Cre/Wt}$. Mice heterozygous for the *Cmtm5* gene ($Cmtm5^{Wt/-}$) were bred without *Cnp-Cre* and the homozygous offspring was used as experimental ($Cmtm5^{-/-}$, knock-out) and control ($Cmtm5^{Wt/Wt}$, wildtype) groups.

Further, we cross-bred $Cmtm5^{Wt/-}$mice with $Cmtm5^{Wt/-}$ harboring the Wallerian degeneration slow mutation heterozygously (Wld^{s}, Coleman et al., 1998; Mack et al., 2001). To evaluate the influence of Wld^{s} on axon degeneration caused by *Cmtm5* deletion we analyzed $Cmtm5^{Wt/Wt}$, $Cmtm5^{Wt/Wt}$*Wld^{s} (control groups) and $Cmtm5^{-/-}$, $Cmtm5^{-/-}$*Wld^{s} (knock-out groups). Littermate mice were used as experimental controls as far as possible.

3.2.1.2 Generation of inducible *Cmtm5* knock-out mice

For deletion of *Cmtm5* in adult animals, $Cmtm5^{fl/fl}$ were bred with mice expressing tamoxifen inducible *Cre* under the *Plp* Promoter ($Plp^{CreERT2}$, Leone et al., 2003) resulting in $Cmtm5^{fl/fl*}$ $Plp^{CreERT2}$ mice (also termed *Cmtm5* IKO) and respective controls without *Cre.* For recombination, male mice of both experimental groups were injected Tamoxifen intraperitoneally at 8 weeks of age for 10 days with a 2-day break after the first five injection days (1 mg tamoxifen dissolved in 100 µl corn oil per mouse and day).

3.2.1.3 Generation of conditional *Cmtm5*/*Cmtm6* double knock-out mice

Mice lacking *Cmtm6* in Schwann cells were created before (Eichel et al., 2020) using Dhh^{Cre} (Jaegle et al., 2003). To create mice lacking both *Cmtm5* and *Cmtm6* in Schwann cells, $Cmtm5^{fl/fl}$ and $Cmtm6^{fl/fl}$*Dhh^{Cre} mice were cross-bred until reaching *Cmtm5* and *Cmtm6* flox homozygosity. Finally, $Cmtm5^{fl/fl}$*$Cmtm6^{fl/fl}$ mice were bred with $Cmtm5^{fl/fl}$*$Cmtm6^{fl/fl}$*Dhh^{Cre} mice resulting in mice lacking *Cmtm5* and *Cmtm6* in Schwann cells and respective controls without Dhh^{Cre}.

3.2.1.4 Genotyping PCR

For genotyping, ear punches of 16-21 days old mice were obtained. Biopsies were digested in 300µl 5M NaOH at 95°C for 75-90 minutes. Afterwards, samples were cooled down and 30µl Tris/HCl pH 8.0

were added. Biopsies were stored at 4°C until further use. Polymerase chain reaction (PCR) was performed to amplify genotype specific DNA fragments from genomic DNA (Saiki et al., 1988). Respective primers (see list in materials section) were provided by the service facility of the MPI-EM. Sample mixes were created as described in the materials section. 20µl of the respective primer mix was added to 1 µl DNA and PCRs were run in a T3 Thermocycler (Biometra GmbH, Göttingen, Germany). Agarose gels (2% [w/v] agarose in TBE buffer) were used to separate the DNA samples. 5µl Gel Red Nucleic acid Stain (BioTrend, Cologne, Germany) was added to each PCR Samples. The whole sample volume (approximately 26µl) was loaded per well along with a pre stained 100bp or 1000bp marker (GeneRuler, Thermo Fischer Scientific). Separation was carried out in gel chambers filled with TBE at 120V for 60-90 minutes. Images of the samples were obtained with an Intas UV system (Intas Science Imaging, Göttingen, Germany).

3.2.2 Purification of myelin and axogliasome-enriched fractions (AEF)

3.2.2.1 Myelin Purification

Myelin enriched fractions were prepared from mice brains of the respective age as described earlier (e.g.,Erwig et al., 2019). In brief, one hemisphere was homogenized in 5 ml 0.32 M sucrose using an T10 ULTRA-TURRAX® homogenizer (IKA, Staufen, Germany) and 200 µl brain lysate was directly snap-frozen on dry ice and stored at -80°C until further use. The remaining sample was then carefully layered over 0.85 M sucrose and centrifuged at 75000 *g* and 4°C with an XL-70 ultracentrifuge with Optima™ TLX rotor (Beckman Coulter, Krefeld, Germany) for 30 minutes. Myelin was collected from the interphase with a Pasteur pipette and transferred to a new ultracentrifuge tube. Myelin membranes were further distorted using osmotic shocks as follows: centrifuge Tubes were filled with $_{dd}H_2O$ and kept on ice for 10 minutes followed by a centrifugation step at 12000 *g* for 15 minutes at 4°C. The pellet was resuspended in 0.32 M sucrose containing protease inhibitor and layered over 0.85 M sucrose in a fresh ultracentrifuge tube. The samples were again centrifuged for 30 minutes at 75000 *g* and 4°C using slowest acceleration and deceleration possible. The interphase was again collected in a fresh ultracentrifuge tube using a pasteur pipette. The tube was filled up with $_{dd}H_2O$ and centrifuged at 12000 *g* for 10 minutes. Finally, the water was discarded and the remaining myelin pellet was resuspended in 200-300 µl 1x TBS containing protease inhibitor. Samples were snap-frozen on dry ice and kept at -80°C until further use.

3.2.2.2 AEF purification

Axogliasome-enriched fractions were isolated as described in (Eichel et al., 2020). The protocol was adapted for the use of mouse brains instead of mouse sciatic nerves. For each biological replicate two mouse brains from P75 old *Cmtm5*$^{-/-}$ mice and respective wildtype controls were pooled. Brains were collected in centrifuge tubes containing 1.25 M sucrose with protease inhibitor tablets (Roche Diagnostics, GmbH, Mannheim, Germany) and homogenized using an T10 ULTRA-TURRAX® homogenizer (IKA, Staufen, Germany). The nerve lysate was carefully overlaid with 1 M sucrose followed by 0.29 M sucrose. Centrifugation was carried out with an XL-70 ultracentrifuge with Optima™ TLX rotor (Beckman Coulter, Krefeld, Germany) at 100.000 *g* for 16 h at 4°C with slowest possible acceleration and deceleration. The axogliasome-enriched fraction at the 1/1.25 M interphase was collected with a Pasteur pipette and transferred into a new centrifugation tube. The AEF was processed with two consecutive washing and osmotic shocks steps: centrifuge Tubes were filled with $_{dd}H_2O$ and kept on ice for 10 minutes followed by a centrifugation step at 12000 *g* for 15 minutes at 4°C. Finally, the supernatants were carefully discarded and the AEF-pellet was taken up in 50-100 µl 1x TBS containing protease inhibitor. Samples were snap-frozen on dry ice and stored at -80°C until further use.

3.2.3 Label-free quantification of proteins in myelin and AEF samples

Proteome experiments were carried out by Dörte Hesse and and quality control and data analysis were carried out by Dr. Olaf Jahn (Proteomics Group, MPI-EM, Göttingen). Myelin samples for proteome analysis were prepared by Ramona Jung (Neurogenetics group, MPI-EM, Göttingen). The whole procedure for proteome experiments was described in (Buscham et al., 2021) as follows: The In-solution digestion of myelin proteins according to an automated filter-aided sample preparation (FASP) protocol (Patzig et al., 2016) and LC-MS-analysis by different MS^E-type data-independent acquisition (DIA) mass spectrometry approaches was performed as recently established for PNS (Siems et al., 2020) and CNS (Jahn et al., 2020) myelin. Briefly, protein fractions corresponding to 10 µg myelin protein were dissolved in lysis buffer (1% ASB-14, 7 M urea, 2 M thiourea, 10 mM DTT, 0.1 M Tris pH 8.5) and processed according to a CHAPS-based FASP protocol in centrifugal filter units (30 kDa MWCO, Merck Millipore). After removal of the detergents, protein alkylation with iodoacetamide, and buffer exchange to digestion buffer (50 mM ammonium bicarbonate (ABC), 10 % acetonitrile), proteins were digested overnight at 37°C with 400 ng trypsin. Tryptic peptides were recovered by centrifugation and extracted with 40 µl of 50 mM ABC and 40 µl of 1% trifluoroacetic acid (TFA), respectively. Combined flow-throughs were directly subjected to LC-MS-analysis. For quantification according to the TOP3 approach (Silva et al., 2006), aliquots were spiked with 10 fmol/µl of Hi3 EColi standard (Waters

Corporation), containing a set of quantified synthetic peptides derived from E. coli. Chaperone protein ClpB.

Nanoscale reversed-phase UPLC separation of tryptic peptides was performed with a nanoAcquity UPLC system equipped with a Symmetry C18 5 µm, 180 µm × 20 mm trap column and a HSS T3 C18 1.8 µm, 75 µm × 250 mm analytical column (Waters Corporation) maintained at 45°C. Peptides were separated over 120 min at a flow rate of 300 nl/min with a gradient comprising two linear steps of 3-35% mobile phase B (acetonitrile containing 0.1% formic acid) in 105 min and 35-60% mobile phase B in 15 min, respectively. Mass spectrometric analysis on a quadrupole time-of-flight mass spectrometer with ion mobility option (Synapt G2-S, Waters Corporation) was performed in the dynamic range-enhanced (DRE)-UDMS^{E} mode as established previously for proteome analysis of purified myelin (Jahn et al., 2020; Siems et al., 2020). Continuum LC-MS data were processed using Waters ProteinLynx Global Server (PLGS) and searched against a custom database compiled by adding the sequence information for E. coli. Chaperone protein ClpB and porcine trypsin to the UniProtKB/Swiss-Prot mouse proteome (release 2017-07, 16909 entries) and by appending the reversed sequence of each entry to enable the determination of false discovery rate (FDR). Precursor and fragment ion mass tolerances were automatically determined by PLGS and were typically below 5 ppm for precursor ions and below 10 ppm (root mean square) for fragment ions. Carbamidomethylation of cysteine was specified as fixed and oxidation of methionine as variable modification. One missed trypsin cleavage was allowed. Minimal ion matching requirements were two fragments per peptide, five fragments per protein, and one peptide per protein. The FDR for protein identification was set to 1% threshold.

For post-identification analysis including TOP3 quantification of proteins, ISOQuant (Distler et al., 2014; Kuharev et al., 2015) software freely available at www.isoquant.net) was used as described previously (Jahn et al., 2020; Siems et al., 2020). Only proteins represented by at least two peptides (minimum length six amino acids, score ≥ 5.5, identified in at least two runs) were quantified as parts per million (ppm), i.e. the relative amount [w/w] of each protein in respect to the sum over all detected proteins. FDR for both peptides and proteins was set to 1% threshold and at least one unique peptide was required. Proteome profiling comparing myelin from *Cmtm5* cKO and CTRL mice was performed with three biological replicates and duplicate digestion, resulting in a total of 6 LC-MS runs per condition. For data visualization and further analysis Microsoft Excel 2016 and GraphPad Prism 8 was used

3.2.4 SDS PAGE and Immunoblotting

3.2.4.1 Sample preparation

The protein concentration of all samples (lysate, myelin, AEF) was measured using the BioRad DC protein assay kit (Lowry assay, Lowry et al., 1951). In brief, a calibration line was prepared using the respective sample buffer for each fraction (Lysate= 0.32 M sucrose, Myelin, AEF= 1x TBS) containing 0.5 µg/µl to 2.5µg/µl BSA. 25µl of reagent A were pipetted into a 96 well plate followed by 5 µl of either the protein standard or the samples. Then, 200 µl of reagent B were added into each well and the plate was incubated for 10 minutes at room temperature. Samples and protein standards were measured in duplicates or triplicates. Finally, the optical density was measured at 650 nm with a microplate reader using the Gen5 software (BioTek Instruments, Bad Friedrichshall, Germany).

For immunoblotting, samples were diluted in 1x SDS sample buffer and 5% Dithiotheitol (DTT) was added as reducing agent. Samples were kept at -20°C until further use.

3.2.4.2 SDS PAGE

Protein separation was performed by SDS-Page using selfcast Acylamid gels (8-12% depending on protein of interest) and the Mini-PROTEAN Handcast system (BioRad, Munich, Germany). Before loading, samples were heated at 40°C for 10 minutes. Depending on the protein of interest between 1-15 µg sample were loaded per pocket. 5 µl pre-stained protein ladder (PageRuler™, Thermo Fischer Scientific) served as control for band sizes and was loaded in a free pocket next to the samples. Seperation was carried out with the BioRad Protein Electrophoresis device with a constant current of 200V for 45-60 minutes. Gels were then carefully removed and incubated in transfer buffer for rougly 10 minutes until immunoblotting.

3.2.4.3 Immunoblotting

Immunoblotting was performed using the Novex® Semi-Dry Blotter (Invitrogen, Karlsruhe, Germany), a BioRad power supply and PVDF membranes (GE Healthcare, Buckinghamshire, UK). Before blotting, PVDF membranes were activated with pure ethanol for 1 min followed by 2 washing steps with $_{dd}H_2O$ for 30 seconds and were kept afterwards in transfer buffer until blotting. Pre cooled transfer buffer was used to soak eight Whatman™ papers (GE Healthcare Life Sciences, Buckinghamshire, UK) per membrane. The “sandwich” was assembled on the anode of the blotter as follows: 4 Whatman™ paper, PVDF membrane, Acrylamide Gel, 4 Whatman™ paper. Air bubbles between the sheaths were carefully removed with a plastic roller. Proteins were transferred at 20V for 45-60 minutes (depending

on protein size). Following blotting, the membranes were incubated in 5% [w/v] non-fat dry milk diluted in 1x TBST for 45-60 minutes at room temperature. Respective primary antibodies were diluted in 5 ml blocking buffer and membranes were incubated overnight at 4°C in 50 ml Falcon Tubes (Cornig, Reynosa, Mexico) with rotation. Blots were then washed three times with 1x TBST for 10 minutes. Followed by incubation in secondary HRP antibody diluted in blocking buffer at room temperature for 1-2 hours. The membranes were again washed three times for ten minutes with 1x TBST.

For detection membranes were incubated with enhanced chemiluminescent detection (ECL) solution according to the manufacturers instructions. Depending on signal intensity normal (Western Lightning® Plus-ECL) or stronger ECL (SuperSignal™ West Femto Maximum sensitive Substrate, Thermo Fischer Scientific, St. Leon-Rot, Germany) was used. Membranes were incubated with appropriate standard proteins to ensure equal loading.

3.2.5 Immunohistochemistry

3.2.5.1 Perfusion

Before perfusion, mice were injected intraperitoneally with 0.2 ml Avertin per 10 g bodyweight. After three to five minutes, reflexes were checked to ensure a deep anesthesia. The abdomen and the diaphragm were opened using scissors and a butterfly cannula (27G, Venofix) was injected into the left ventricle. A small incision was made into the right atrium to ensure blood and fixative efflux. The body was first flushed for 2-3 minutes using prewarmed (37°C) HBSS (Invitrogen, Karlsruhe, Germany) followed by 10 minutes of 4% [w/v] PFA. Following perfusion, tissues were dissected and post-fixed overnight in 4% [w/v] PFA. Samples were either directly processed or stored in 4% [w/v] PFA at 4°C.

3.2.5.2 Preparation of Paraffin and Cryosections

For neuropathological staining's and quantification of oligodendrocyte cell number, paraffin embedded sections were used which were processed as follows: Following fixation, brains were cut into 2 coronal slices at the approximal height of the hypothalamus. Brain tissue was then placed into small plastic wire cases and embedded in paraffin (Paraplast, Leica, Wetzlar, Germany) using an automated system (HMP 110, MICROM) with the following protocol:

Time (hours)	Solution
1	50% [v/v] Ethanol
2	70% [v/v] Ethanol
2	70% [v/v] Ethanol
1	96% [v/v] Ethanol
1	96% [v/v] Ethanol
1	100% [v/v] Ethanol
1	100% [v/v] Ethanol
1	Isopropanol
2	Xylol
2	Xylol
2	Paraffin
2	Paraffin

Following the automated embedding, brain sections were placed with the sectioned side down into metal forms which were filled with paraffin. The paraffin was left to harden and sectioned with a Microtome (HM 400, MICROM) into 5 µm sections. Brain slices were collected on microscope slides and kept overnight at 37°C. Brain slices were then stored at room temperature until further use.

Preparation of cryosections was performed as described in (Buscham et al., 2021): Cryosection were obtained from perfused or immersion fixed optic nerves and spinal cords. Nerves were kept in a sucrose buffer (10% [w/v], 20% [w/v], 30% [w/v] in 0.1 M phosphate buffer) over night at 4°C for each concentration. The nerves were then embedded in small plastic chambers using Tissue-Tek® O.C.T.™ Compound (Sakura, Staufen, Germany). Nerves were stored at -20°C until further use. 10 µm thick cross-sections were prepared using a cryostat (Reichert Jung® Cryocut 18000, Wetzlar, Germany) and transferred to Superfrost® Plus microscope slides (Thermo Fischer Scientific, St. Leon-Rot, Germany). Slides were dried for 30 minutes at room temperature and stored at -20°C until further use.

3.2.5.3 Neuropathological stainings and analysis

Slides were incubated at 60°C for ten minutes and afterwards deparaffinized in the following order: Xylol, Xylol, Isopropanol/Xylol (1:1) for 10 minutes each. Followed by a decreasing ethanol line: 100% Ethanol, 90% Ethanol, 70% Ethanol, 50% Ethanol and H_2O for five minutes each. Slides were then incubated in citrate buffer for 5 minutes, during that time 300 ml citrate buffer was heated until the buffer was cooking. Slices were transferred in the preheated buffer and heated in the microwave for 10 minutes. Afterwards the slides were left to cool at room temperature. Slides were then transferred

into Tris-Buffer containing 2% skim milk powder. For the next incubation steps, small capillary chambers were created on top of the slides using the Shandon cover plate system (Thermo Fisher Scientific). Fitting was controlled by filling the chambers with Tris-Buffer containing 2% skim milk powder. Afterwards, 100 µl 3% H_2O_2 were added for 5 minutes to inactivate the endogenous peroxidases which could lead to unspecific signals when using a horse-radish-peroxidase (HRP) coupled secondary antibody. To reduce non-specific binding of the antibody, the tissue was blocked for 10 minutes with 100 µl goat serum diluted 1:5 in PBS/BSA. Afterwards the slides were incubated with the first respective antibody over night at 4°C. The slides were rinsed with 2% skim milk in Tris-Buffer and 100µl of the biotinylated secondary antibody were added followed by 100 µl of the HRP-streptavidin complex. The microglial activation factor-3 (MAC3) and the microglia marker IBA1 were detected using the Vector Elite ABC kit (Vector Labs, Lörrach, Germany). Amyloid β precursor protein (APP) and the glial fibrillary acidic protein (GFAP) were labeled with the $LSAB_2$ kit, following the instructions by the manufacturer (DAKO, Hamburg, Germany). MAC3 and IBA1 were incubated for 30 minutes and GFAP and APP for 10 minutes. The slides were washed with 2% skim milk in Tris-Buffer once and the cover plates were removed. The bound antibodies were visualized using 100 µl of the DAB-Kit (Zytomed Systems GmbH, Berlin, Germany). Cell Nuclei were stained by incubating the slides in hematoxylin for 30 seconds. The slides were than rinsed in $_{dd}H_2O$ followed by a short incubation in HCL-alcohol, rinsed again and finally incubated in Scott´s solution for 5 minutes. Then the slides were washed in $_{dd}H_2O$ and incubated in an increasing ethanol line as follows: 50% Ethanol, 70% Ethanol, 90% Ethanol and 100% Ethanol for five minutes each. Following the ethanol line, slices were incubated for 10 minutes in Isopropanol/Xylol (1:1) once and twice in Xylol. Finally, the slides were mounted using Eukitt.

For analysis the hippocampal fimbria was imaged using a bright-field light microscope at 40x magnification (Zeiss AxioImager Z1, coupled to Zeiss AxioCam, MRc Camera, controlled and stitched by Zeiss Zen 1.0 software). APP positive spheroids were counted by hand and normalized to the quantified area. GFAP/MAC3/IBA1 relative immunopositive area was determined using a semi-automatically ImageJ plugin (de Monasterio-Schrader et al., 2013; Lüders et al., 2017; Patzig et al., 2016).

3.2.5.4 Quantification of oligodendrocyte cell number

To quantify oligodendrocyte cell number, coronal paraffin embedded brain sections were used following the above-described protocol up until the antigen retrieval step using Citrate buffer. Following the Citrate-Buffer cooking step, samples were blocked for 1 hour at room temperature with PBS containing BSA and horse serum. Incubation with CAII primary antibody was carried out over 48h at 4°C (1:300 in PBS containing 1% Horse serum). Afterwards, slides were washed three times for 10

minutes with PBS and incubated with DAPI (Thermo Fischer Scientific) and anti-rabbit Alexa555 (Dianova, 1:1000 in PBS containing 1% HS) for 1 hour at room temperature. Slides were washed three times again using PBS for 10 minutes and finally mounted using AquaPolymount. The hippocampal fimbria was imaged with an Axio Observer Z2 (Zeiss) at 40x magnification. Images were stitched using the Zeiss Zen 1.0 Software. All cell positive for both DAPI and CAII were identified as oligodendrocytes. All positive cells were counted and numbers were normalized to an area of 1 mm^2.

3.2.5.5 Preparation of cryosections and confocal imaging

Preparation of cryosections for imaging was performed as described in (Buscham et al., 2021): Cryosection were obtained from spinal cords immersion fixed with 4% PFA overnight. Nerves were then transferred to a sucrose buffer (10% [w/v], 20% [w/v], 30% [w/v] in 0.1 M phosphate buffer) over night at 4°C for each concentration. The nerves were then embedded in small plastic chambers using Tissue-Tek® O.C.T.™ Compound (Sakura, Staufen, Germany). Nerves were stored at -20°C until further use. 10 µm thick cross-sections were prepared using a cryostat (Reichert Jung® Cryocut 18000, Wetzlar, Germany) and transferred to Superfrost® Plus microscope slides (Thermo Fischer Scientific, St. Leon-Rot, Germany). Slides were dried for 30 minutes at room temperature and stored at -20°C until further use.

Sections were stained with the following protocol using 200 µl volumes per slide: 3 minutes Methanol, 30 minutes permeabilization using PBS with 0.4% [v/v] Triton-X100 (Sigma Aldrich, St. Louis, USA) followed by blocking using DAKO blocking buffer (DAKO, Hamburg, Germany) for 60 minutes. (Covance) and CMTM5 (custom made by Pineda, Berlin, Germany Table 2) antibodies were diluted in antibody diluent (DAKO, Hamburg, Germany) and incubated for 48 hours at 4°C in a dark, humid chamber. Sections were then washed three times with PBS for 10 minutes and incubated with secondary antibodies (α-rabbit STAR-RED, α-mouse STAR-ORANGE, abberior, Göttingen, Germany, Table 2) diluted 1:200 in antibody diluent for 60 minutes. Sections were washed 3 times with PBS for 10 minutes and mounted using AquaPolymount (Polysciences, Warrington, USA). Images were obtained on a Confocal and STED FACILITY line microscope (Abberior Instruments, Germany) and acquired as xy-plane with a pixel size of 30nm. The fluorophores were excited with appropriate excitation lasers at 640nm (abberior STAR RED) and 561nm (abberior STAR ORANGE).

Imaging was performed by Martin Meschkat (Abberior Instruments GmbH, Göttingen). For image acquisition the microscope software “Lightbox” as provided by Abberior Instruments was used.

3.2.5.6 Quantification of RGC number

Protocol for the preparation of retinae and quantification of RGC number was described in (Buscham et al., 2021): To assess retinal ganglion cell numbers (RGC), eyes of 1 year old *Cmtm5*$^{-/-}$ mice and respective controls were dissected and fixed for one hour with 4% PFA/Phosphate Buffer (PB). Eyes were then rinsed in PB and retinae were dissected as follows. The eye was cut open along the ciliary body and cornea and lens were removed. The retinal pigment epithelium (RPG) was carefully removed. Four cuts on opposing sites were made to flatten the retina. The retina was transferred into a 24 well plate with 1 retina per well containing PBS. Retinae were washed with PBS/2% Triton X-100 (500µl/well) at room temperature and gentle agitation for 10 minutes. To permeate nuclear membranes the wash solution was replaced by fresh PBS/2% Triton X-100 and retinae were frozen at -80°C for 10 minutes. Retinae were washed twice with PBS/0.5% Triton X-100 for 5 minutes at room temperature. To reduce unspecific AB binding retinae were incubated with blocking buffer (PBS/ 5%BSA/ 5% Donkey Serum/ 2% Triton X-100) for 1 hour at room temperature with gently agitation. To label RGCs, retinae were incubated with guinea pig anti-RBPMS (Sigma-Aldrich; 1:200 in blocking buffer, 350µl per well) for 2 hours at room temperature. Retinae were then washed thrice with PBS/0.5% Triton X-100 for 10 minutes at RT. RGCs were labelled using donkey anti-guinea pig Alexa 555 (1:1000 in blocking buffer) and incubated over night at 4°C. Retinae were then washed thrice for 30 minutes with PBS and transferred to a Superfrost® Plus microscope slides with a fine brush. Retinae were mounted using AquaPolymount with the RGC layer facing up. Slides were kept at 4°C and dark until imaging. Images were taken using the Axio Observer Z2 (Zeiss) and a 40x magnification and stitched using Zeiss Zen2011. For assessment of RGC number the average of 3 different areas (area= mm^2 per rectangle) were analyzed for each inner/middle/outer part of the retina. In total, retinae of three different animals were analyzed per genotype.

3.2.6 Electron microscopy

Samples for transmission electron microscopy (TEM) and focused ion-beam scanning electron microscopy (FIB-SEM) were prepared for sectioning by Torben Ruhwedel and Anna Steyer (Electron Microscopy facility, MPI-EM, Göttingen) and sectioning of FIB-SEM samples was carried out by Torben Ruhwedel and Anna Steyer.

3.2.6.1 TEM

Animals of the respective age and genotype were sacrificed by cervical dislocation. Tissue was dissected and fixed in Karlsson-Schultz fixative solution at 4°C overnight and kept in 1% PFA for longer

storage. For transmission electron microscopy, fixed nerves were embedded in EPON using an automated system (EMPT, Leica; Wetzlar, Germany). Before, tissue was placed in small plastic baskets containing 0.1 M phosphate buffer.

The following protocol was used for sample preparation:

Solution	**Incubation time**	**Temperatur**
Phosphate buffer	3x 10 min	4 °C
2% [w/v] OsO_4	4h	4 °C
H_2O	3x 10 min	4 °C
30% [v/v] Ethanol	20 min	4 °C
50% [v/v] Ethanol	20 min	4 °C
70% [v/v] Ethanol	20 min	4 °C
90% [v/v] Ethanol	20 min	4 °C
100% [v/v] Ethanol	4x 10min	4 °C
Propylenoxid	3x 10 min	RT
Propylenoxid/Epon 2:1	2h	RT
Propylenoxid/Epon 1:1	2h	RT
Propylenoxid/Epon 1:2	4h	RT
Epon	4h	RT

Tissue was then carefully placed in silicon molds filled with Epon and labelled using small paper labels. Epon embedded samples were kept at 60°C over-night to allow the Epon to polymerize.

TEM sections were prepared as described in (Buscham et al., 2021): Ultrathin (50nm) sections were prepared using a PTPC Powertome Ultramicrotome (RMC, Tuscon Arizona, USA) and a diamond knife (Diatome AG, Biel, Switzerland). Sections were cut and collected on formwar coated cooper grids (AGAR scientific, Essex, UK). To enhance contrast, ultrathin sections were stained with UranyLess (Electron Microscopy Science, Hatfield, Panama) for 20 minutes and washed 6 times with $_{dd}H_20$. For analysis 16-20 non-overlapping random images were taken per animal (exact number of mice in the figure legends) using the Zeiss EM900 at 7000x (one image = 220µm^2). All image analysis was performed using Fiji (Version 2.0.0-rc-68/1.52i; Schindelin et al., 2012))

To assess relative number of pathological axons and pathological myelin units, all axons on 16-20 non-overlapping random images were analyzed per mouse. For the diameter analysis all normal appearing and properly cross-sectioned myelinated axons were evaluated on 16-20 non-overlapping random images. Data is presented as mean axonal diameter per animal. g-ratios were calculated as ratio between axonal diameter and the outer (abaxonal) diameter of the corresponding myelin sheath. In

total 200 axons were randomly selected for g-ratio analysis from 16-20 EM images per mouse using the Fiji Grid tool (Circular grids, 3 μm^2 per point, random offset).

3.2.6.2 Preparation and quantification of semithin sections

For the analysis of axon number in optic nerves (ON) and the axonal diameters in sciatic and phrenic nerves, semithin (500 nm) sections were prepared using a PTPC Powertome Ultramicrotome (RMC, Tuscon Arizona, USA) and a diamond knife (Diatome Ultra 45°). Sections were collected on microscope slides and dried. Afterwards, sections were stained with methylene blue/azur II (1:1) for one minute followed by a washing step with H_2O. After drying, sections were embedded using Eukitt. Images were acquired at x100 using a bright-field light microscope (Zeiss AxioImager Z1; coupled to Zeiss Axio Cam MRc camera; controlled and stitched by Zeiss Zen 1.0 software).

Optic nerves were analyzed as follows: Using Fiji, ON images were separated into 55 μm^2 rectangles. From all rectangles filled with ON tissue 5 were chosen at random and all axons were counted. Axon number is shown as mean of 5 rectangles per mouse.

Axonal diameters in the PNS were analyzed using a semi-automated approach with “analyze particle” function of FIJI. The Particle analyzer was set to an appropriate size and circularity and all profiles were inspected carefully. Inaccurate ROIs were deleted and drawn by hand. Tilted and not properly sectioned axons were not included in the analysis of axonal diameters. Mean axonal diameters were calculated using GraphPad Prism 8, shifts in axonal diameters (according to Kolmogorov-Smirnoff test) were calculated using an R script described in (Eichel et al., 2020). Analysis of *Cmtm5/6* dKO were carried out by Hanna Pies and Maria Eichel.

3.2.6.3 FIB-SEM

FIB-SEM sectioning and imaging was performed by Dr. Anna Steyer (EMBL Imaging Center, Heidelberg). Samples were prepared according to (Buscham et al., 2021; Steyer et al., 2020). In short, the dissected samples were immersed in primary fixative and processed with a modified OTO-protocol (Deerinck et al., 2010), as described previously (Weil et al., 2018). Samples were post-fixed for 3 h with 2% OsO_4 and 1.5% $K_3Fe(CN)_6$ at 4 °C followed by a contrasting step with 1% thiocarbohydrazide 1 h at room temperature and 1.5 h incubation with 2% OsO_4. *E*n bloc staining was done with 2% uranyl acetate overnight at 4 °C. The next day the nerve samples were dehydrated through a series of ascending concentrations of acetone for 15 min each (30%, 50%, 75%, 90%, 3× 100%) and incubated with increasing concentrations of resin (2:1, 1:1, 1:2) for 2 h each and left in 90% Durcupan over night

without component D. The next day the samples were incubated with 100% Durcupan (all components) for 4.5 h and polymerized for 48 h at 60 °C.

The polymerized samples were trimmed using a 90° trimming knife (Diatome) and positioned on a SEM-stub using silver conductive resin (EPO-TEK 129-4). The surface was sputtered coated (Leica, ACE 600) with a layer of 10 nm platinum and placed inside the FIB-SEM (Crossbeam 540, Zeiss). After exposing a cross-section through the region of interest with 15 nA ion current and polishing with 7 nA, a 400 nm deposition of platinum was done using 3 nA. The final dataset was acquired at 1.5 kV (1000 pA) 5 nm × 5 nm × 25 nm voxel size with a milling current of 1.5 nA. Fiji (Schindelin et al., 2012) was used for all following image processing steps: The images were aligned using the SIFT algorithm, cropped and inverted. They were smoothed using a Gaussian blur (sigma 1) and a local contrast enhancement was applied (CLAHE: blocksize 127, histogram bins 256, maximum slope 1.25). The dataset was binned by 2 in x and y. Analysis of pathological myelin and axonal profiles was carried out using Fiji. All profiles in the volume belonging to one of the categories (Myelin outfoldings, Inner-tongue inclusions, Axoplasmic inclusions, Myelin whorls) were counted and values were normalized to a volume of 10000µm^3. Example 3D models were reconstructed using IMOD (v 4.9.12, University of Colorado).

3.2.7 Cell culture and exosome purification

3.2.7.1 Oligodendrocyte cell culture

Oligodendrocyte cell culture and exosome analysis was performed by Dr. Christina Müller (University of Mainz) and described in detail before (Frühbeis et al., 2020). Primary oligodendrocytes were kept in culture for six days. Culture supernatants were collected over a period of 48 h under serum-free conditions.

3.2.7.2 Exosome purification and EV analysis

Briefly, culture supernatant was cleared from dead cells and debris by successive centrifugation for 10 min at 300 x *g* and 30 min at 10,000 x *g* and 4°C in a fixed angle rotor (220.78, Hermle). sEVs remaining in the supernatant were pelleted by ultracentrifugation in polyallomer tubes (Beckman Coulter) for 2 h at 100,000 x *g* and 4°C (SW40 rotor, 27.000 rpm, RCF (max) 130.000, k-factor 301.4, Beckman Coulter). 10K and 100K pellets were resuspended in SDS-PAGE sample buffer for Western blot analysis. Cells were scraped in 10 mM Tris pH 7.4, 150 mM NaCl, 1 mM EDTA, 1 % Triton X-100 and protease inhibitor cocktail (Roche complete) on ice. Nuclei were pelleted by centrifugation for 5 min at 2000 x

g. Cell lysates and sEV/exosome samples were subjected to 12 % SDS-PAGE and Western blotting (Biorad). Proteins were blotted onto a PVDF membrane, which was subsequently blocked with 4 % milk powder and 0.1 % Tween in PBS. Membranes were sequentially incubated with primary and HRP-coupled secondary antibodies and proteins were detected using chemiluminescence reagents (Luminata Crescendo, Millipore) and X-ray films. Films were scanned and analysed using ImageJ software (National Institutes of Health).

3.2.8 MRI and MRS

Magnetic resonance imaging (MRI) and magnetic resonance spectroscopy were performed as described in (Buscham et al., 2021): Experiments were carried out at the Functional imaging facility (DPZ, Göttingen, Germany) by Kerstin Fuhrmann, Sina Bode and Kristin Kötz. Data analysis was performed by Tor Rasmus Memhave, Rakshit Dardawal and Prof. Dr. Susann Boretius. Magnetic resonance imaging (MRI) and spectroscopy (MRS) were acquired on a 9.4T Bruker BioSpec MR system with a 30 cm horizontal bore and B-GA12 gradient system operating on Bruker ParaVision 6.0.1 (Hardware and software from Bruker BioSpin MRI GmbH, Ettlingen, Germany). A four-channel (2×2) receive-only mouse head coil was used, in combination with a 112/84 resonator, to acquire MRI and MRS (both components from Bruker).

The MRI protocol included magnetization transfer (MT)-weighted images and diffusion-weighted images. For MT, a 3D fast low angle shot (FLASH) sequence was used to acquire three datasets: MT-weighted, proton density-weighted, and T1-weighted (repetition time [15.1, 15.1, 18] ms, echo time 3.4 ms, flip angles [5˚, 5˚, 25˚], two averages, voxel size 100 µm × 100 µm × 100 µm, acquisition time 18.4 min). These datasets were used to estimate MT saturation (MTsat) according to the method described by (Helms et al., 2008). Diffusion-weighted images (DWI) were acquired using a spin-echo echo-planar imaging sequence (repetition time 2000 ms, echo time 21.5 ms, two repetitions, voxel size 100 µm × 100 µm × 500 µm, gradient duration and separation 2.5 ms and 12.5 ms, b values 0, 1000 and 2000, gradient directions 30 for each b value, acquisition time 17.2 min). These DWI scans were preprocessed through denoising (Fadnavis et al., 2020) and averaged across repetitions. A diffusion tensor model (Basser et al., 1994) was fitted to the preprocessed DWI data, and fractional anisotropy (FA), axial diffusivity (AD), radial diffusivity (RD), and mean diffusivity (MD) maps were derived from (Garyfallidis et al., 2014).

Magnetic resonance spectroscopy was acquired from cortex and corpus callosum using a stimulated echo acquisition mode (STEAM) sequence. The parameters of the STEAM sequence were as follows: repetition time of 6000 ms, echo time of 10 ms, spectral width of 5000 Hz, 2048 data points, 128

averages, and a total acquisition time of 12:48 min. The dimensions of the cortical and corpus callosum voxels were 3.9×0.7×3.2 mm^3 and 3.9×0.7×1.7 mm^3, respectively. All spectra were acquired with CHESS water suppression and outer volume suppression. The spectra were analyzed and quantified using LCModel (Provencher, 1993) in the chemical shift range from 0.2 to 4.2 ppm. Statistics were performed in *Excel* using a 2-tailed, unpaired t-test assuming equal variance.

3.2.9 Measuring RNA abundances using qRT-PCR

Quantitative realtime PCR was carried out by Ursula Kutzke (MPI-EM, Göttingen, Germany).

3.2.9.1 Sample Preparation and mRNA extraction

For analysis of *Mct1* and *Cmtm5* mRNA abundances corpus callosa of 6-month-old *Cmtm5*$^{-/-}$ and respective wildtype controls were dissected and kept at -80°C until further processing. RNA isolation was carried out using the "Rneasy Mini Prep" kit from Qiagen. Tissue was homogenized in Trizol (Life Technologies™, Thermo Fischer Scientific, St Leon-Rot, Germany) followed by RNA extraction using chloroform. Quality and concentration of the RNA were checked with the Agilent RNA 6000 Nano Kit, the Agilent 2100 Bioanalyzer (Agilent Technologies, Santa Clara, California, United States) and the Nano Drop 2000 spectrophotometer (Thermo Fischer Scientific, St. Leon-Rot, Germany). RNA concentration of all samples was adjusted to 100 ng/µl.

Complementary single stranded DNA (cDNA) was synthesized from isolated RNA using the SuperScript III reverse transcriptase (Invitrogen, Karlsruhe, Germany) with the following protocol:

cDNA synthesis
8 µl RNA (800 ng in total) 2 µl dT mic Primer (0.6 pmol/µl) 2 µl N9 (120 pmol/µl) The mix was incubated for 10 minutes at 70°C and 1 minute on ice to denature RNA and primers
The following mix was then added to the reaction: 4 µl 5x firstt strand buffer 1 µl dNTP (10 mM) 2 µl DDT (100 mM) 1 µl SuperScript III reverse transcriptase (200 U/µl) Mix was incubated as follows: 25°C 10 minutes 50°C 45 minutes 55°C 45 minutes

Finally the cDNA of all sapmes was diluted to a concentration of 47.62 ng/µl with $_{dd}H_2O$ and stored at -20°C until further use.

3.2.9.2 qRT-PCR

Pipetting for qRT-PCR was performed using the epMotion 5075 pipetting robot (Eppendorf, Hamburg, Germany). Further the Power SYBR Green PCR Master Mix (Promega, Fitchburg, Wisconsin, United States) and the Light Cycler 480II (Roche Dianostics GmbH, Mannheim, Germany) were used for qRT-PCR. Primer sequences for the genes of interest are were listed before. For each biological replicate 4 technical replicates were used.

Protocol for qRT-PCR
Primer mix:
2 µl cDNA 82ng/µl)
5 µl SYBR Green PCR Master Mix
0.1 µl forward primer
0.1 µl reverse primer
2.8 µl $_{dd}H_2O$
PCR Program
15 min 95°C
50 cycles:
15 seconds 95°C
1 minute 60°C
Melting: 95°C 10 seconds
1 minute 65°C

Analysis was performed with Microsoft Excel and GraphPad Prism. Genes of interest were normalized to the mean of the housekeeping genes *Rps13* and *Rplp0* which did not differ between the genotypes.

3.2.10 Behavior

3.2.10.1 Electroretinography (ERG) and visually evoked potentials (VEP)

Visually evoked potentials (VEP) experiments were carried out by Stefan Tohm and Dr. Nicola Strenzke (Institute for Auditory Neuroscience, University medicine of Göttingen, Germany) and data analysis was carried out by Dr. Nicola Strenzke. The protocol for the experimental procedure and analysis is derived from (Buscham et al., 2021):

ERGs were recorded as described (Dieck et al., 2012) and VEP were recorded essentially as described (Ridder and Nusinowitz, 2006). Briefly, mice were dark adapted overnight and anesthetized with

Ketamin (125µg/g), Xylazin (2,5µg/g) and Buprenorphin i.p. (0,1 mg/kg). Eyes were kept moist using contact lens solution containing hyaluronic acid for ERG recordings and with Methocel (DuPont Pharma, Mississauga, Canada) for VEP recordings. For ERG recordings, a silver ball electrode placed in the outer angle of the left eye served as active electrode. Signals were averaged 10 times. For VEP recordings, the scalp was resected and a small hole was drilled on the right side 1 mm lateral and 1mm rostral of lambda and a thin needle electrode was inserted superficially. Signals were averaged at least 50 times. The reference electrode was placed on the nose of the mouse and the common ground near the hind legs. Signals were amplified 1000 times (NeuroAmp) and sampled without analog filtering. 0.1 ms light flashes were generated using BioSig Software and TDT system III hardware (Tucker Davis Technologies, Davis, USA) and presented via a custom-designed Ganzfeld apparatus at a stimulus rate of 0.5 Hz. Illumination was calibrated using a luxmeter (Mavolux 5032c, Nürnberg, Germany) and an Integrated Photodiode Amplifier 10530 (Integrated Photomatrix Limited, Dorchester, UK). Analysis was performed using custom written Matlab scripts (version 2019b). For analysis of ERG and VEP thresholds, Student´s t-test was applied. Data from ERG and VEP analysis is represented in line graphs showing mean values of mice per genotype ±SEM. To determine the genotype-dependent effect on ERG and VEP amplitude and latencies across various light intensities, 2-way-ANOVA was applied.

3.2.10.2 Gait analysis using the CatWalk^{TM} assay

The CatWalk^{TM} assay (Noldus, Wageningen, Netherlands) was used to analyze the gait and motor capabilities of *Cmtm5* cKO mice and respective controls with an age of 6 month. In brief, the mouse walks over an illuminated glass plate. Paw contact leads to glass illumination that is captured by a camera below the glass plate. The camera is able to capture positioning of toes and paws, gait, as well as walking speed and paw pressure on the glass (derived from light intensity). Animals are trained 5 days on the device one time per day, followed by an experimentation day with three measurements. Measurements during training and experiment take 10 minutes each and all crossing over the glass plate are recorded once the animal enters a predefined field of view. Between each measurement, animals are brought back to their cage for at least 10 minutes. Between runs the device is cleaned with 70% [v/v] Ethanol and water. For analysis all runs are validated by hand using the CatWalk XT 10.6 (Noldus; Wageningen, Netherlands) software. Runs were animals stop (eg explore/clean themselves) while passing the field of view were not included in the analysis. For statistical assessment, the mean values for all parameters from at least 6 runs were used per animal.

3.2.10.3 Open Field

We analyzed motoric capabilities and explorative behavior using an open field assay (Dere et al., 2014). Two hours before the start of the experiment, mice were brought to the experiment room to habituate. For the experiment, mice were placed in an empty, grey plastic box (120cm in diameter, 25 cm high) with an open lid. Light intensity in the center was 140 lux. *Cmtm5* cKO mice and respective controls with an age of 6 month were analyzed. Animals were placed alone into the box and were able to freely explore it for 10 minutes. Using a camera and an automated tracking software (Viewer2, Biobserve, Bonn, Germany) the following parameters were tracked: latency to move from the center of the box to the periphery, time spent in the different predefined zones (centre, mid-area, periphery), as well as overall distance covered and speed. Afterwards mice were placed into a new cage and the box was cleaned using 70% [v/v] Ethanol and water. The next mouse was placed into the cage after 5 minutes. All mice were analyzed on the same day.

3.2.10.4 Rotarod

The Rotarod system 3375.5 (TSE systems) was used to further assess motor capabilities of *Cmtm5* cKO mice and respective controls with an age of 6 month. Mice, were placed on a rotating rod in a small chamber, secluded from other experimental mice. Rotation was accelerated from 5-20 rpm in 180 seconds. Training consisted of 2 consecutive days with 3 runs per mouse repeated three times (9 runs per training day per mouse). Followed by the experiment day with three consecutive runs and three trials in total per animal. Mice had a ten minutes break between each trial. The latency to fall per trial was calculated using Microsoft Excel 2016.

3.2.11 Statistics

All experiments were analyzed blinded for genotypes. Statistical assessment was performed using GraphPad Prism 8 (GraphPad, Software Inc., San Diego, United States), Matlab (v 2019b), Microsoft Excel 2016 or R. Two-sided Student´s t-test was applied to compare two groups. Welch´s correction was performed in case of unequal distribution. Axonal diameter shifts were analyzed using an R script which was described earlier (Eichel et al., 2020) for these measures, significances according to Kolmogorov-Smirnoff were applied. Levels of significance were set at $p<0.05$ (*), $p<0.01$ (**) and $p< 0.001$ (***). For all graphs exact p-values are given in the figure legends. The Bioconductor R packages ‘limma’ and ‘q-value’ were used to detect significant changes in protein abundance by moderated t-statistics as described (Ambrozkiewicz et al., 2018; Siems et al., 2020). Data from ERG and VEP analysis (Figure 13) is represented in line graphs showing mean values of mice per genotype ±SEM. To

determine the genotype-dependent effect on ERG and VEP amplitude and latencies across light intensities, 2-way-ANOVA was applied. For all experiments, statistical testing and correction is reported in the figure legends. Exact sample size and number of animals is shown in the figures or indicated in the figure legends.

4 Results

4.1 Identification of CMTM5 as a CNS myelin protein

Following recent findings in the PNS where Schwann-cell expressed CMTM6 restricts axonal diameters (Eichel et al., 2020), we were curios whether we can find a functional homolog in the CNS. From all the members of the CMTM protein family only CMTM5 is expressed in myelinating oligodendrocytes to a considerable amount (Figure 3A, B). Further, the expression of CMTM5 is mostly specific for cells of the oligodendrocyte lineage in humans and mice (Figure 3C-F) and was identified in datasets analyzing myelin (Gargareta et al., 2022; Jahn et al., 2020) of both species. To date, CMTM5 has never been described as a CNS myelin protein and its function in oligodendrocytes has not been investigated until now.

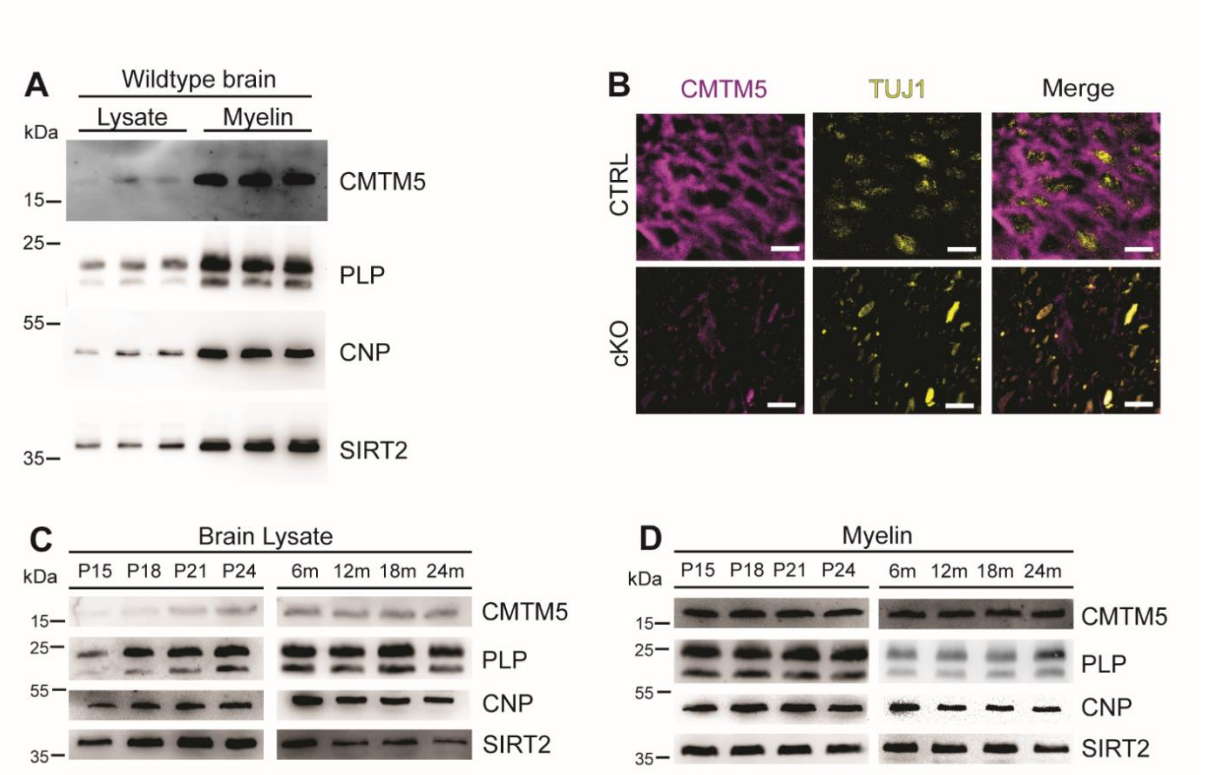

Figure 5: Identification of CMTM5 as a CNS myelin protein. (A) Immunoblot analysis of CMTM5 in myelin biochemically purified from brains of C57/Bl6 mice at the age of 75 days (P75) compared to brain lysate. CMTM5 is enriched in myelin fractions. Known myelin proteins PLP, CNP and SIRT2 are detected as myelin markers. Shown are three biological replicates. **(B)** Immunohistochemistry and confocal microscopy of spinal cord sections of mice at P75. Note that CMTM5 (magenta) labelling was consistent with localization in myelin surrounding beta-III tubulin (TUJ1)-immunopositive axons (yellow) in CTRL (*Cmtm5*$^{fl/fl}$) mice. CMTM5 labelling was not detected in myelin of mice lacking *Cmtm5* expression in mature oligodendrocytes (*Cmtm5*$^{fl/fl}$**Cnp*$^{Cre/Wt}$, cKO). Scale bar, 2 µm. **(C, D)** Immunoblot analysis of CMTM5 in brain lysate **(C)** and biochemically purified myelin **(D)** of young and aged mice (P15 up to 2 years). Note that the increase of CMTM5 abundance in brain lysate coincides with developmental myelination **(D)**. Shown is one biological replicate per age. PLP, CNP, SIRT2 were detected

as markers. P= postnatal day, m=months. Imaging of IHC sections in **(B)** was performed by Martin Meschkat (Abberior Instruments Gmbh, Göttingen).

To validate CMTM5 as a new myelin protein we compared its abundance in lysate and myelin fractions from brains of wildtype C57/Bl6 mice (Figure 5A). Indeed, CMTM5 is highly enriched in purified myelin fractions alongside with known myelin proteins like PLP, CNP and SIRT2. Furthermore, its localization in immunofluorescent stainings is consistent with myelin surrounding axons stained with the neurofilament marker TUJ1 in the CNS (Figure 5B).

Given the specific expression of CMTM5 in oligodendrocytes and myelin we were further interested how its abundance changes during early myelination and how stable its abundance remains in older age. Thus, we analyzed lysate and myelin fractions from different stages during development (P15-P24) and adulthood (6-24 months) (Figure 5C, D). As expected, the abundance of CMTM5 as well as the myelin proteins PLP, CNP and SIRT2 increased in brain lysate during early development, coinciding with CNS myelination (Figure 5C). Interestingly, CMTM5 abundance remains largely constant in brain lysate and myelin even up to an old age of 24 months.

The enrichment of CMTM5 in purified myelin fractions, its localization to myelin sheaths and its increased expression during CNS myelination alongside other known myelin makers allow for the assumption that CMTM5 can indeed be considered as a novel CNS myelin protein.

4.2 Analysis of mice conditionally lacking CMTM5

To investigate the function of oligodendrocyte expressed CMTM5 for the CNS, we created a mouse line conditionally lacking CMTM5 in myelinating glial cells (*Cmtm5*$^{fl/fl}$**Cnp*$^{Cre/Wt}$ mice, also termed *Cmtm5* cKO; *Cmtm5*$^{fl/fl}$, controls) taking advantage of *Cre* mediated recombination under control of the *Cnp*-promoter (Lappe-Siefke et al., 2003). The main body of research for this project was performed with *Cmtm5* cKO mice and respective controls and the resulting data is presented in the following chapter.

4.2.1 CMTM5 is not essential for myelin biogenesis, structure or composition

We classified CMTM5 as a novel myelin protein and were thus interested how deletion of CMTM5 in oligodendrocytes would affect myelin composition, biogenesis and structure. The successful deletion of CMTM5 was confirmed using immunoblot experiments with myelin samples biochemically purified from brains of control and *Cmtm5* cKO mice at age P75 as well as immunohistological stainings of spinal

cord sections derived from *Cmtm5* cKO mice and respective controls (Figure 5B; Fig 6A). While CMTM5 was readily detectable in brain myelin derived from CTRL mice it was absent in myelin from *Cmtm5* cKO mice. The known myelin proteins PLP and SIRT2 were unaffected by *Cmtm5* deletion and served as loading controls while CNP was reduced by approximately 50%. Note that this reduction is expected as *Cnp* served as the Cre driver, essentially leaving only one functional *Cnp* allele.

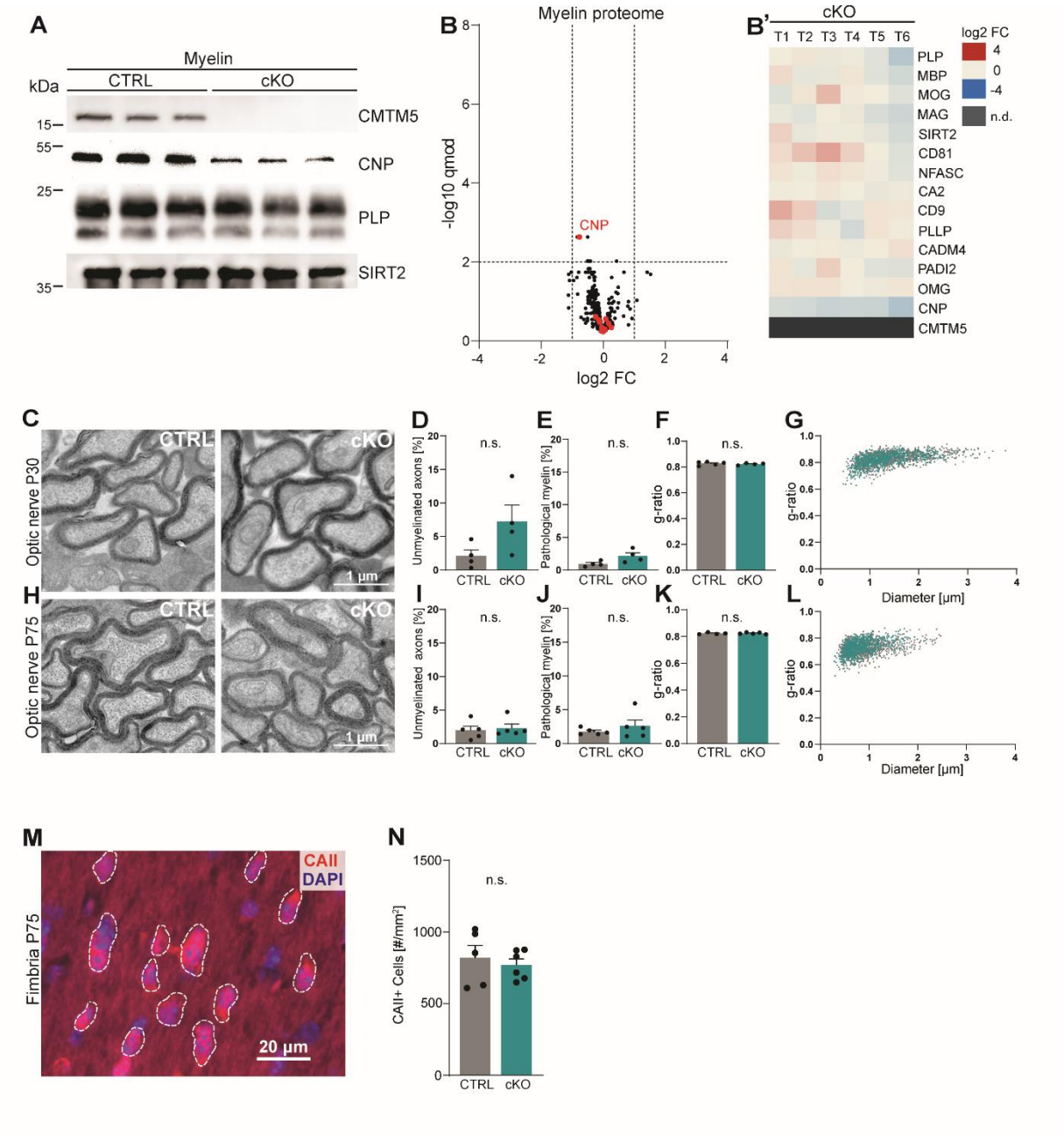

Figure 6: CMTM5 is not essential for myelin biogenesis and composition. (A) Immunoblot analysis shows that CMTM5 is undetectable in myelin purified from the brains of *Cmtm5*$^{fl/fl}$**Cnp*$^{Cre/Wt}$ (cKO) mice. PLP, CNP, SIRT2 were detected as markers. Shown are three biological replicates per genotype. **(B, B')** Quantitative proteome analysis of brain myelin reveals largely similar myelin composition in *Cmtm5* cKO and CTRL mice. Analyzed were n=3 mice per genotype and 2 technical replicates per mouse. **(B)** Volcano plot with data points representing the

log2-fold change and -log10-transformed q-values of 428 identified proteins in cKO compared to CTRL myelin. Red dots highlight known myelin proteins. CMTM5 is not displayed because it was not identified in *Cmtm5* cKO myelin. **(B')** Heatmap showing the relative abundance of selected known myelin proteins in *Cmtm5* cKO compared to control myelin. The Foldchange (FC) is displayed as log2 with red representing enrichment and blue representing diminishment of of proteins in *Cmtm5* cKO myelin. Data represents n=3 mice per genotype analyzed as 2 technical replicates per mouse (T1-T6). Note that the relative abundance of most myelin proteins was largely similar in cKO and CTRL myelin. In agreement with the immunoblot analysis in **(A)** the abundance of CNP was about halved in *Cmtm5* cKO myelin reflecting that the Cre driver line ($Cnp^{Cre/Wt}$) possesses only one native *Cnp* allele. CMTM5 was not detected (n.d.) in cKO myelin. **(C-L)** Electron micrographs and quantitative assessment of myelin in CTRL and cKO optic nerves at postnatal day (P) 30 **(C-G)** and P75 **(H-L)**. Percentage of unmyelinated axons **(D, I)** and pathological myelin profiles is similar between both groups **(E, J)**. Data corresponds to all axons from 18-20 non-overlapping random EM images from 4-5 animals per group. Two-tailed Student´s t-test, **D**: p= 0.1003; **E**: p= 0.0596; **I**: p= 0.3937; **J**: p= 0.7269. Mean g-ratio **(F, K)** is similar between the experimental groups at P30 and P75. Data corresponds to 200 axons randomly selected from 18-20 EM images for each animal. n= 4-5 mice per group. Two-tailed Student´s t-test **F**: p= 0.5894; **K**: p= 0.8821. **(G, L)** Scatter plot showing g-ratios in relation to respective axonal diameters. No apparent shift between the experimental groups is detectable. **(M, N)** Immunohistochemistry and genotype-dependent quantification of CAII immune-positive oligodendrocytes in a representative white matter tract (hippocampal fimbria) at P75. **(M)** Representative fluorescence micrograph, stippled lines encircle CAII positive cells. Scale bar, 20 µm. **(N)** Number of CAII immuno-positive cells is similar in the fimbria of CTRL and *Cmtm5* cKO mice. n= 5-6 mice per group, unpaired Student´s t-test p= 0.5971. Bar graphs give mean ± SEM; Data points in bar graphs represent induvial mice. Experimental procedure for Proteome analysis in **(B)** was performed by Dörte Hesse and data processing was performed by Olaf Jahn (Proteomics group, MPI-EM, Göttingen).

Further, we analyzed the proteome composition of myelin samples from *Cmtm5* cKO and respective controls by using quantitative mass spectrometry (Figure 6B, B´). As expected, we were able to replicate the results from the immunoblot experiments. CMTM5 was not detected in samples derived from *Cmtm5* cKO mice and CNP abundance was approximately halved. Noteworthy, the overall proteome profile appeared mostly similar between the two groups (Figure 6B) and the abundance of known myelin proteins was unaltered (Figure 6B´).

To inspect potential alterations in myelin biogenesis and structure when CMTM5 is lacking in oligodendrocytes we analyzed the optic nerve of *Cmtm5* cKO mice and respective controls at P30 and P75 using transmission electron microscopy (TEM) (Figure 6C-L). The number of unmyelinated fibers as well as profiles with abnormal appearing myelin (including myelin outfoldings) was not significantly altered between the two groups at P30 (Figure 6D, E) and P75 (Figure 6I, J) and g-ratios, as an indicator of myelin sheath thickness, were unchanged at P30 (Figure 6F, G) and P75 (Figure 6K, L).

To ensure that deletion of CMTM5 does not impact oligodendrocyte number we analyzed the amount of CAII positive cells in the Fimbria at P75 (Figure 6M, N). The number of mature CAII positive oligodendrocytes was unaltered between *Cmtm5* cKO and control mice suggesting a stable population of mature oligodendrocytes even after *Cmtm5* deletion.

We further analyzed the brains of 8 months old control and *Cmtm5* cKO mice using magnetic resonance imaging (MRI) to assess changes in morphometry and diffusivity in different white and grey matter

areas (Figure 7). We found no evident changes in brain morphometry between the two groups (Figure 7A) and diffusivity measures (Figure 7B-E) as well as the magnetization transfer ratio (MTsaT) (Figure 7F) were unaltered in *Cmtm5* cKO mice compared to respective control mice. Indicating, normal myelination and myelin integrity in the brain of *Cmtm5* cKO mice.

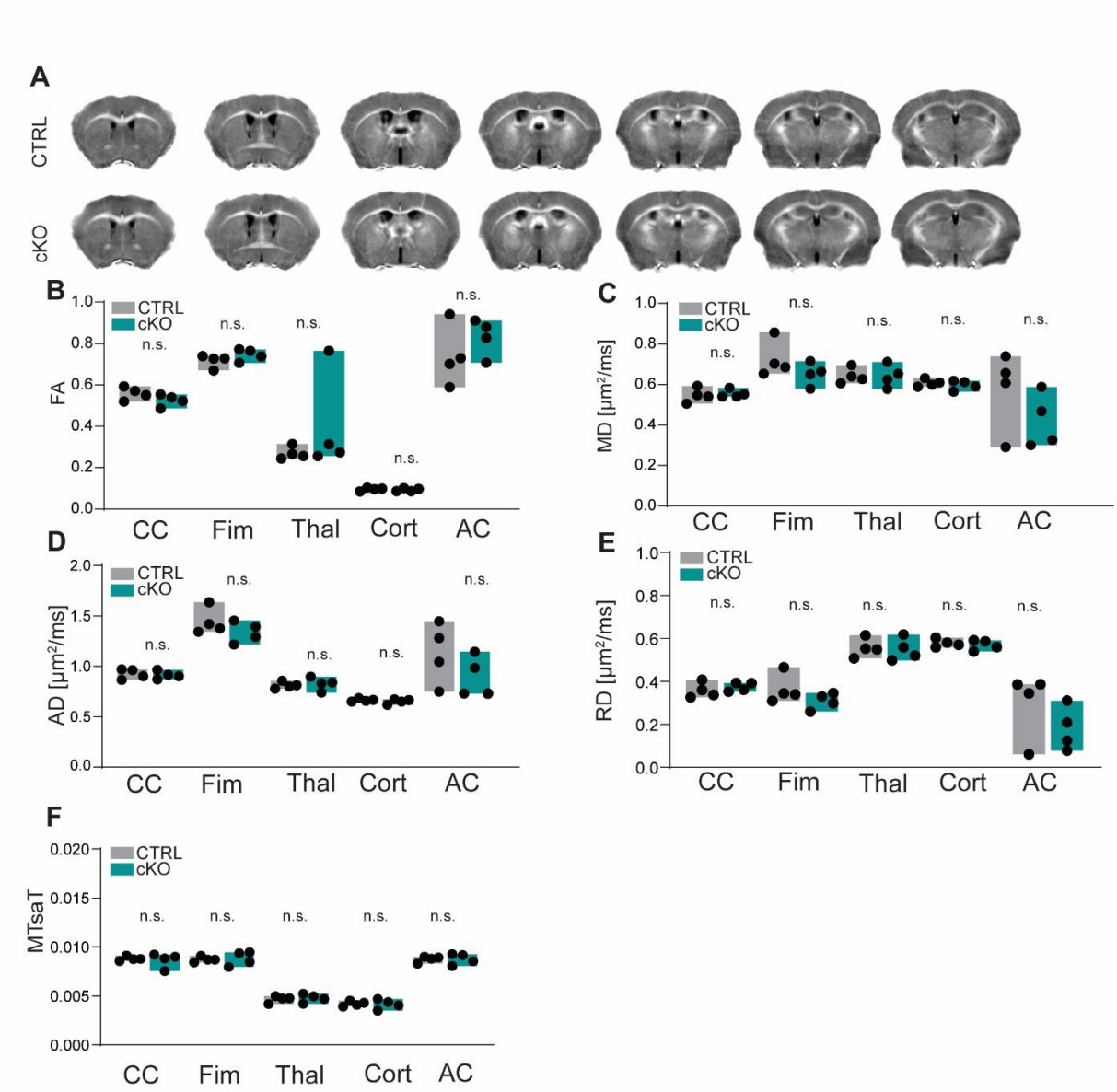

Figure 7: Unaltered white matter volume, integrity and diffusivity in brains of *Cmtm5* cKO mice. (A) Magnetic resonance imaging (MRI)-based morphometry of brains from CTRL and *Cmtm5* cKO mice at 8 months of age. Shown are representative genotype averaged (4 mice per genotype) effective transverse relaxation rate (R_2^*) MRI images. **(B-E)** Diffusion tensor imaging (DTI) indicates unchanged fractional anisotropy (FA), mean diffusivity (MD), axial diffusivity (AD) and radial diffusivity (RD) in white and grey matter in brains of *Cmtm5* cKO and CTRL mice. CC, Corpus callosum; Fim, Fimbria; Thal, Thalamus; Cort, Cortex; AC, Anterior commissure. n=4 per genotype. **(F)** Magnetization transfer saturation index (MTsaT) is unaltered in *Cmtm5* cKO compared to CTRL mice. All graphs give mean ± SEM; all data points represent individual mice. Two-sided Student´s t-test was applied. **(B)** CC: p= 0.1739; Fim: p= 0.2244; Thal: p= 0.3229; Cort: p= 0.6159; AC: p= 0.3290. **(C)** CC: p= 0.7263; Fim: p= 0.2223; Thal: p= 0.9943; Cort: p= 0.5009; AC: p= 0.2425. **(D)** CC: p= 0.7103; Fim: p= 0.2608; Thal: p= 0.6903; Cort: p= 0.3576; AC: p= 0.2531. **(E)** CC: p= 0.4374; Fim: p= 0.2038; Thal: p= 0.8343; Cort: p= 0.5728; AC:

p= 0.2678. **(F)** CC: p= 0.7065; Fim: p= 0.8432; Thal: p= 0.7319; Cort: p= 0.8614; AC: p= 0.9983. Measurements were carried out by Sina Bode and Kristin Kötz, data analysis was performed by Rakshit Dardawal and Susann Boretius (Functional imaging facility, DPZ, Göttingen).

Together, the data presented in Figure 6 and 7 imply that deletion of CMTM5 does not alter myelin composition, biogenesis and structure. Meaning that CMTM5 is not essential for oligodendrocyte function with respect to myelination.

4.2.2 CMTM5 does not regulate axonal diameters in the CNS

Following the previously published findings that Schwann-cell expressed CMTM6 restricts axonal diameters in the PNS (Eichel et al., 2020) we were curious whether CMTM5 is involved in a similar mechanism in the CNS. To analyze shifts in axonal diameters in the CNS, myelinated axons of the optic nerve of *Cmtm5* cKO mice and respective control mice from different timepoints were analyzed on electron micrographs (Figure 8A-B´).

Mean axonal diameters were not significantly changed at ages P75 and P365 between the two groups (Figure 8A´, B´). A slight shift towards larger axonal diameters could be detected at P75 when analyzing the frequency distribution of axonal diameters (Figure 8A), which was not reflected in the mean axonal diameters at P75 (Figure 8A´) and not detectable at one year of age (Figure 8B, B´). Although statistically significant, we decided to regard a shift of 5.9 nm on average towards larger axon diameters of not higher functional importance, especially as this shift is not reflected in the analyses of mean axonal diameters (Figure 8A´).

It is known that changes in axonal diameter can be caused by alteration in neurofilament phosphorylation (de Waegh et al., 1992; Yin et al., 1998). By immunoblotting we did not see a change in abundance of non-phosphorylated neurofilament (SMI32) and phosphorylated neurofilament (SMI31) in brain lysate derived from *Cmtm5* cKO mice and respective controls (Figure 8C). Indicating an unchanged neurofilament phosphorylation state when CMTM5 is deleted in oligodendrocytes, underlining the finding that axonal diameters are unchanged in the CNS of *Cmtm5* cKO mice. Taken together, this data emphasizes that CMTM5 does not alter axonal diameters in the optic nerve.

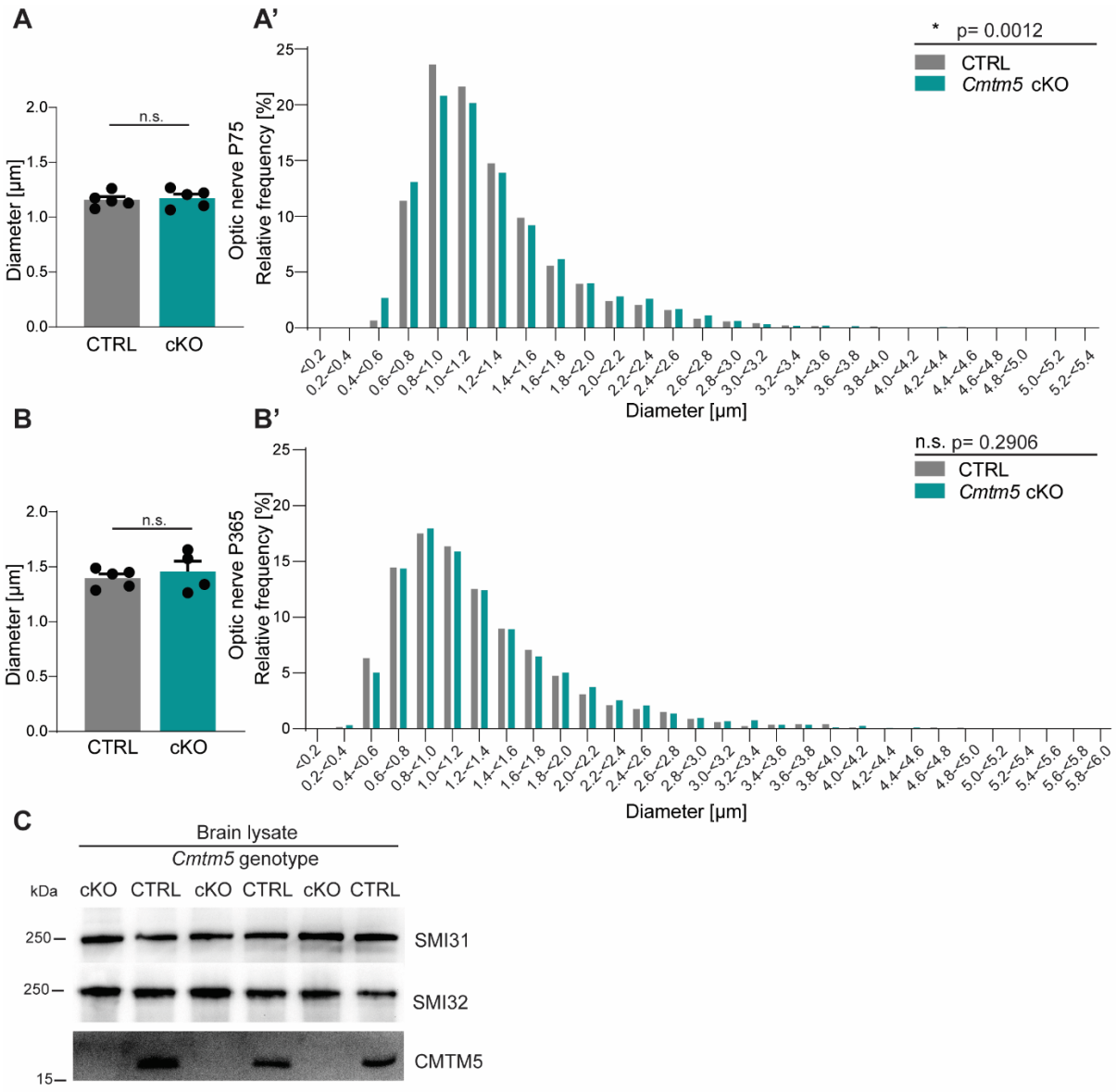

Figure 8: CMTM5 does not regulate axonal diameters in the CNS. (A & B) Analysis of axonal diameters from electron micrographs of optic nerves from *Cmtm5* cKO and control mice at P75 **(A, A´)** and P365 **(B, B´)**. Frequency distribution of axonal diameters shows a slight shift towards larger axons (on average +5.9nm) at P75 **(A´)** which is not reflected in the analysis mean axonal diameters **(A)**. At P365 no significant change in axonal diameters could be detected between the two groups **(B, B´)**. Data corresponds to 800-900 axonal profiles per mouse from 4-5 mice per genotype and timepoint. K/S-test P75: p= 0.0012; P365= 0.2906. Two-sided student´s t-test P75: p= 0.7514; P365= 0.5315. Data is presented as mean ±SEM. **(C)** Immunoblot showing brain lysate of *Cmtm5* cKO and control mice with an age of one year. Abundance of phosphorylated neurofilament (SMI31) and non-phosphorylated neurofilament (SMI32) appears unaltered between the two groups.

4.2.3 CMTM5 deletion in oligodendrocytes causes axonal loss

CMTM5 does not seem to be involved in axon diameter regulations in the CNS and further is not essential for myelin biogenesis, composition or structure. Interestingly, while analyzing optic nerve sections from *Cmtm5* cKO and respective controls using TEM it became evident, that deletion of *Cmtm5* is accompanied by an increased number of pathological axonal profiles (Figure 9A, B). Further analysis revealed that the axonal pathology emerges early at P30 and is progressive until one year of age, which is the oldest timepoint of analysis (Figure 9B). Additionally, the axonal pathology coincides with a trend towards reduced myelinated axonal profiles in the optic nerve at age P30 and P75, which reaches significance at P365 (Figure 9C). Additionally, an increased number of pathological appearing axonal profiles was also observed in the dorsal white matter of the spinal cord in *Cmtm5* cKO mice when compared to respective controls (Figure 9D, E).

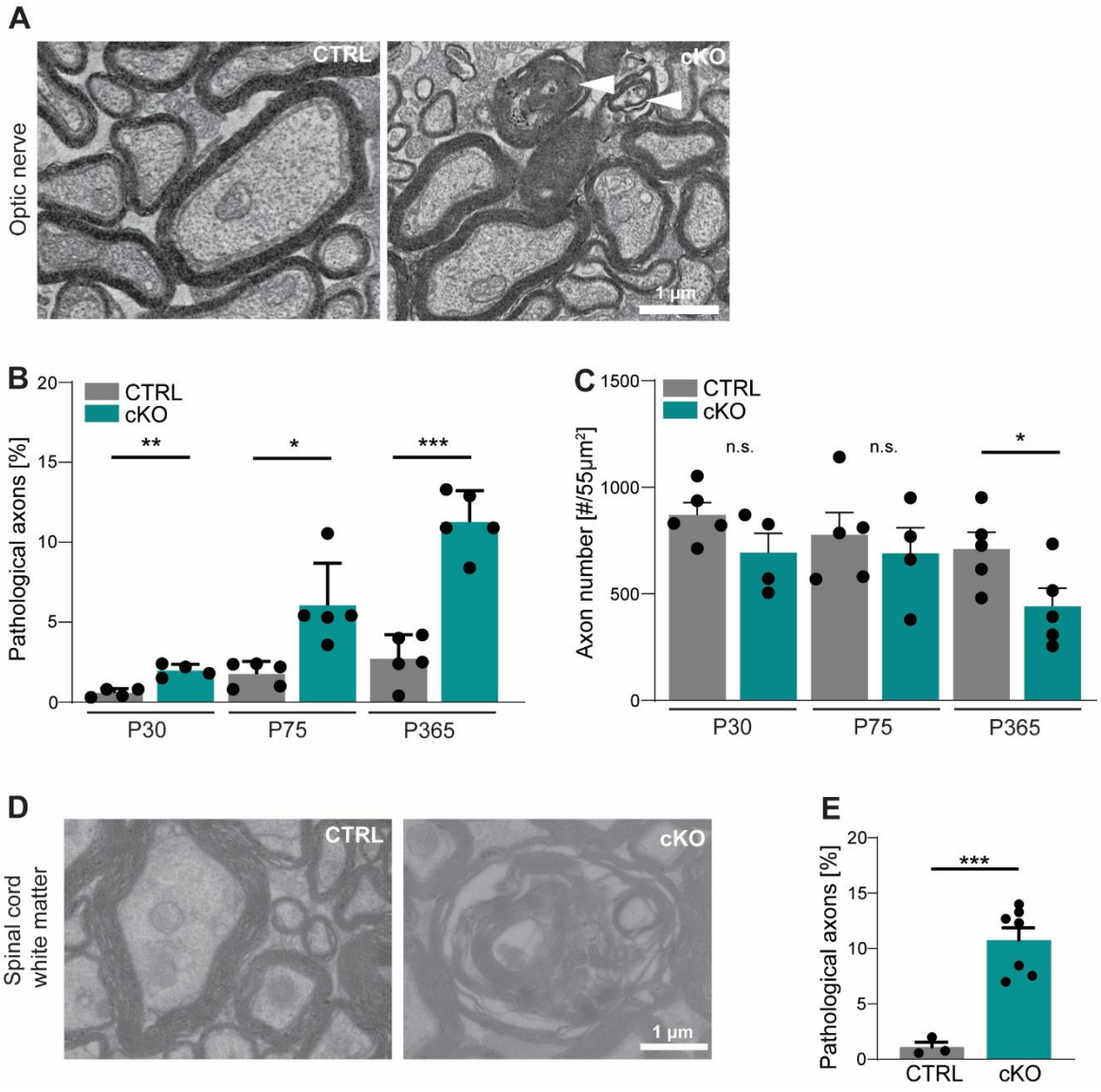

Figure 9: *Cmtm5* deletion in oligodendrocytes causes axonal loss. (A-B) Electron micrographs and genotype-dependent quantitative assessment of CTRL and *Cmtm5* cKO optic nerves at P75. **(A)** Arrowheads indicate

pathological axons. **(B)** Quantification of pathological axons reveals progressive axonopathy in optic nerves of *Cmtm5* cKO mice. n=4-5 mice per group, 18-20 random non-overlapping EM images analyzed, Two-tailed Student´s t-test P30 p= 0.0011; P75 p= 0.0191 (With Welch´s correction); P365 p<0.0001.
(C) Quantitative assessment of axonal numbers on semithin optic nerve sections. n=4-5 mice per group, data represents mean axon number in five 55 μm^2 images per mouse randomly distributed over the entire optic nerve. Axon numbers are significantly reduced at one year of age according to Two-tailed Student´s t-test P30 p= 0.1288; P75 p= 0.5993; P365 p=0.0499. **(D-E)** Electron micrographs and genotype-dependent quantitative assessment of spinal cord white matter in 1 year old CTRL and *Cmtm5* cKO mice. **(F)** Number of pathological profiles is increased in spinal cord white matter of *Cmtm5* cKO mice. n=3-7 mice per group, 20 non-overlapping random EM images per mouse, Two-tailed Student´s t-test p=0.0007. All bars show mean ± SEM; all data points represent individual mice.

Following these results, we further classified the axonal pathology caused by *Cmtm5* deletion in oligodendrocytes using Focused ion beam-scanning electron microscopy (FIB-SEM). Compared to conventional TEM, which only allows for an analysis of two-dimensional (2D) sections, the FIB-SEM technique can be used for a more elaborate analysis as it allows sequential cross-sections to be reconstructed in 3D. We analyzed optic nerves of one year old *Cmtm5* cKO mice and respective controls (Figure 10), focusing on myelin outfoldings, inner-tongue inclusions, axoplasmic inclusions and myelin whorls. The latter can be best described as myelin profiles reminiscent of an axon, probably best interpreted as remnants of axonal degeneration. The number of myelin outfoldings, inner-tongue inclusions and axoplasmic inclusions was not increased in optic nerves from *Cmtm5* cKO mice (Figure 10A´´-C´´). However, the number of myelin whorls were significantly increased in *Cmtm5* cKO mice compared to respective controls indicating axonal pathology following *Cmtm5* deletion in oligodendrocytes (Figure 10D´´).

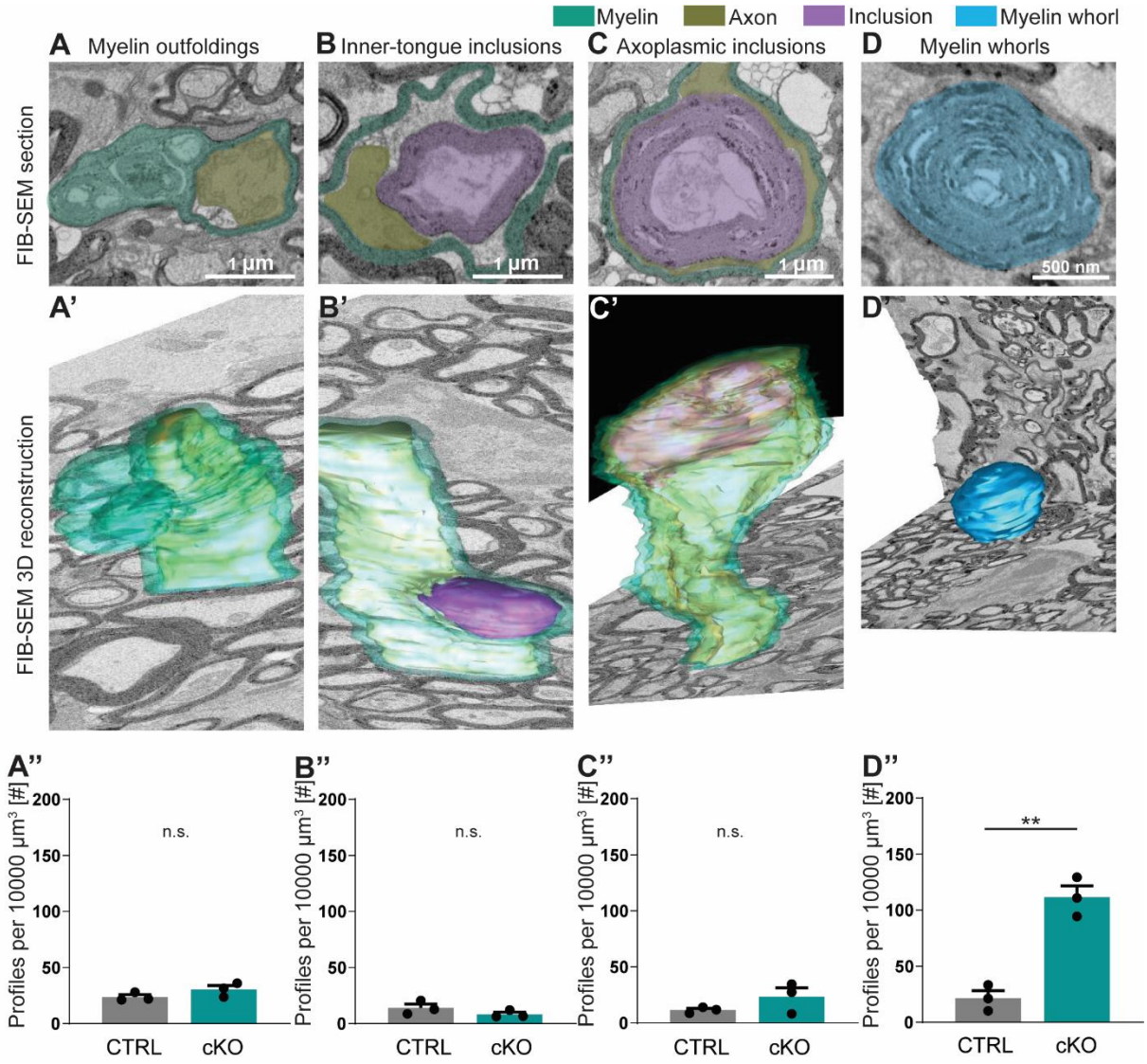

Figure 10: FIB-SEM 3D analysis specifies pathological profiles following *Cmtm5* deletion. Focused ion beam-scanning electron microscopy (FIB-SEM) micrographs **(A)** and 3D reconstruction **(A')** of pathological profiles in *Cmtm5* cKO optic nerve at 1 year. Myelin (cyan), axons (gold), inclusion (purple) and myelin whorls (blue) are highlighted. Pathological profiles include myelin outfoldings, inclusions in the inner tongue, inclusions completely engulfed by axoplasma and myelin whorls. Analysis of the entire 3D volumes reveals that the number of myelin whorls is significantly increased in cKO mice. FIB-SEM stacks of optic nerves of three mice per genotype were analyzed. Normalized volume = 10000µm^3. Two-tailed Student´s t-test **A´´**: p= 0.2062; **B´´**: p= 0.2168; **C´´**: p= 0.2172; **D´´**: p=0.0018. Scale bars **A-C** 1µm, **D** 500nm. All data presented as mean ± SEM. FIB-SEM operation was carried out by Anna Steyer and Torben Ruhwedel (Electron microscopy facility, MPI-EM, Göttingen).

Taken together, this data emphasizes that CMTM5 is involved in supporting axonal integrity and its deletion causes axonal pathology but does not lead to structural changes of the myelin sheaths itself. Further, it is attractive to hypothesize that this process is a general feature of oligodendrocyte-axon signaling in different white matter regions of the CNS.

4.2.4 Late onset neuroinflammation in mice lacking CMTM5 in oligodendrocytes

We were curious whether the axonal degeneration following *Cmtm5* deletion in oligodendrocytes is accompanied by a general neuropathology. We used magnetic resonance spectroscopy (MRS) to analyze the brains of *Cmtm5* cKO mice and respective controls at 8 months of age (Figure 11). Myo-Inositol serving as a marker for astrocytes and microglia was significantly upregulated in the corpus callosum of *Cmtm5* cKO mice, indicating gliosis (Figure 11A). N-acetyl-aspartate (NAA) was used as a marker for axons and neurons. NAA levels were slightly but not significantly reduced in *Cmtm5* cKO mice, possibly indicating lower axon density (Figure 11B).

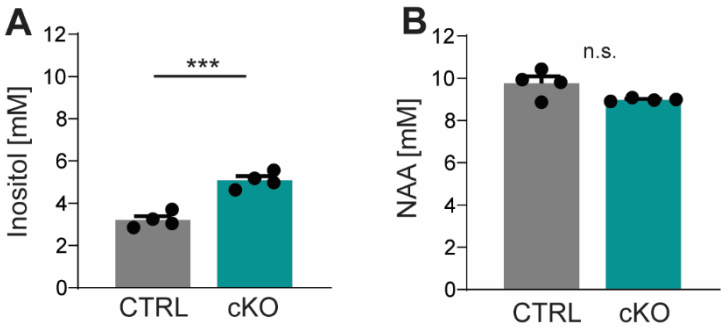

Figure 11: MRS of the corpus callosum of *Cmtm5* cKO mice implies gliosis and a trend towards reduced axon density. (A, B) Spectroscopy of key metabolic markers myo-inositol (for microglia and astrocytes, in **A**) and N-acetyl-aspartate (NAA, for axon/neurons, in **B**). **(A)** The concentration of inositol is significantly increased in the corpus callosum of *Cmtm5* cKO mice compared to controls. Two-tailed Student´s t-test of the mean p= 0.0004. **(B)** NAA levels are unchanged in the corpus callosum of *Cmtm5* cKO mice compared to controls. Two-tailed Student´s t-test of the mean p= 0.057. All bar graphs give mean ± SEM; all data points represent individual mice. MRS was carried out by Sina Bode and Kristin Kötz, data analysis was performed by Tor Rasmus Memhave and Susann Boretius (Functional imaging facility, DPZ, Göttingen).

The MRS results imply the emergence of general neuropathology when *Cmtm5* is missing in oligodendrocytes. To better understand whether the neuropathology emerges as a consequence of axon degeneration or might be causative for it, we decided to analyze the occurrence of common neuropathological markers temporarily. For this approach we used coronal brain sections of *Cmtm5* cKO mice and respective controls at P30, P75 and one year of age. Sections were immunolabeled with markers for axonal swellings (APP), microglia (IBA1/AIF1 and MAC3/LAMP2) as well as astrocytes (GFAP) and the hippocampal fimbria was analyzed (Figure 12). Interestingly, no genotype-dependent differences between *Cmtm5* cKO and control mice could be detected at P30 and P75 with regard to APP-positive swellings or MAC3, IBA1 and GFAP immuno-positive area. However, at one year of age all markers were significantly increased in *Cmtm5* cKO compared to control mice (Figure 12I-L).

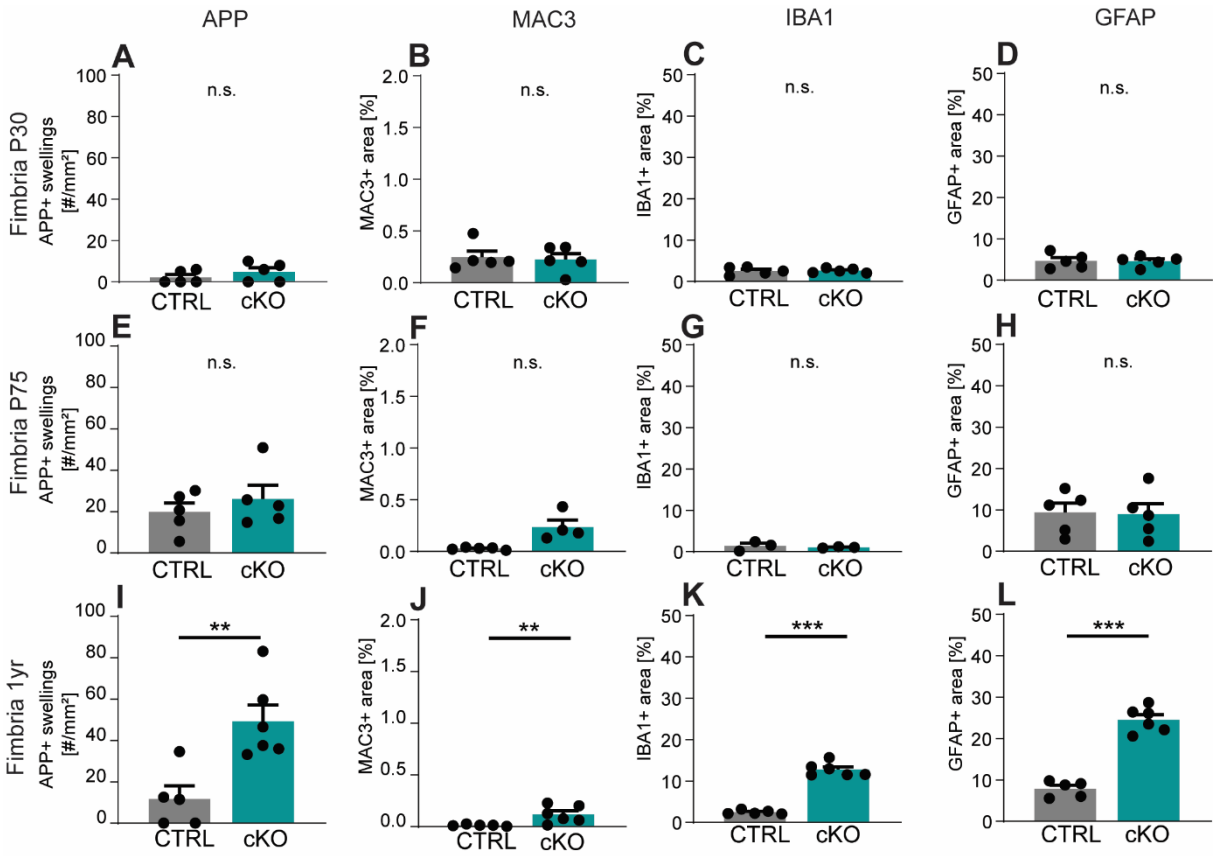

Figure 12: Secondary neuropathology following *Cmtm5* deletion. Immunohistochemical analysis of the hippocampal fimbria using markers for APP positive swellings (APP), microglia (MAC3, IBA1) and astroglia at P30 **(A-D)**, P75 **(E-H)** and 1 year **(I-L)**. **(A, E, I)** Shown is the number of APP-immuno-positive axonal swellings. **(B-D, F-M, J-L)** Shown is the relative area of immunopositivity. At 1 year all markers are significantly increased in *Cmtm5* cKO fimbriae. Paraffin-embedded brain sections, n=3-6 mice per group, data presented as mean ± SEM. Two-tailed Student´s t-test **A**: p= 0.3225; **B**: p= 0.7901; **C**: p= 0.9480; **D**; p=0.9152; **E**: p=0.4413; **F**: p= 0.0525; **G**: p= 0.9049; **H**: p=0.6270; **I**: p= 0.0055; **J**: p=0.0251; **K**: p<0.0001; **L**: p<0.0001.

The results of MRS and immunohistochemistry results indicate that the neuropathology in *Cmtm5* cKO mice emerges at a later timepoint of 8-12 month. It is possible that it reaches significance in a time window between 10 weeks and 8 months already. However, the respective markers are not elevated at P30 and P75 according to immunohistochemistry, a time in which axonal pathology already set in. This implies that the emergence of neuropathology follows axonal degeneration and should rather be interpreted as a consequence of it.

4.2.5 Behavioral analysis of mice conditionally lacking Cmtm5

4.2.5.1 Analysis of ERGs and VEP

Cmtm5 deletion in oligodendrocytes causes axonal degeneration and late onset neuropathology. We were interested how these pathological hallmarks manifest on a functional level. To tackle this, we

chose to analyze the optic tract by measuring visually evoked potentials (VEP) to assess the impairment caused by *Cmtm5* deletion. To ensure retinal functionality, we first analyzed the retinae of *Cmtm5* cKO mice and respective controls using electroretinography (ERG) recordings at 34 weeks of age. ERG waveforms (Figure 13A), ERG thresholds (Figure 13B) as well as amplitudes of a- and b- waves (Figure 13C-D) were unchanged between the two groups, indicating normal function of the retina. However, when analyzing VEPs *Cmtm5* cKO showed altered VEP waveforms (Figure 13E) but normal thresholds (Figure 13F) compared to control mice. VEP latency (Figure 13G) was unaltered between the two genotypes, showing normal speed of action potential propagation, indicating normal myelination of the optic nerve in both experimental groups. A reduction of VEP amplitudes could be observed in *Cmtm5* cKO mice (Figure 13H), probably caused by axonopathy in the optic nerve.

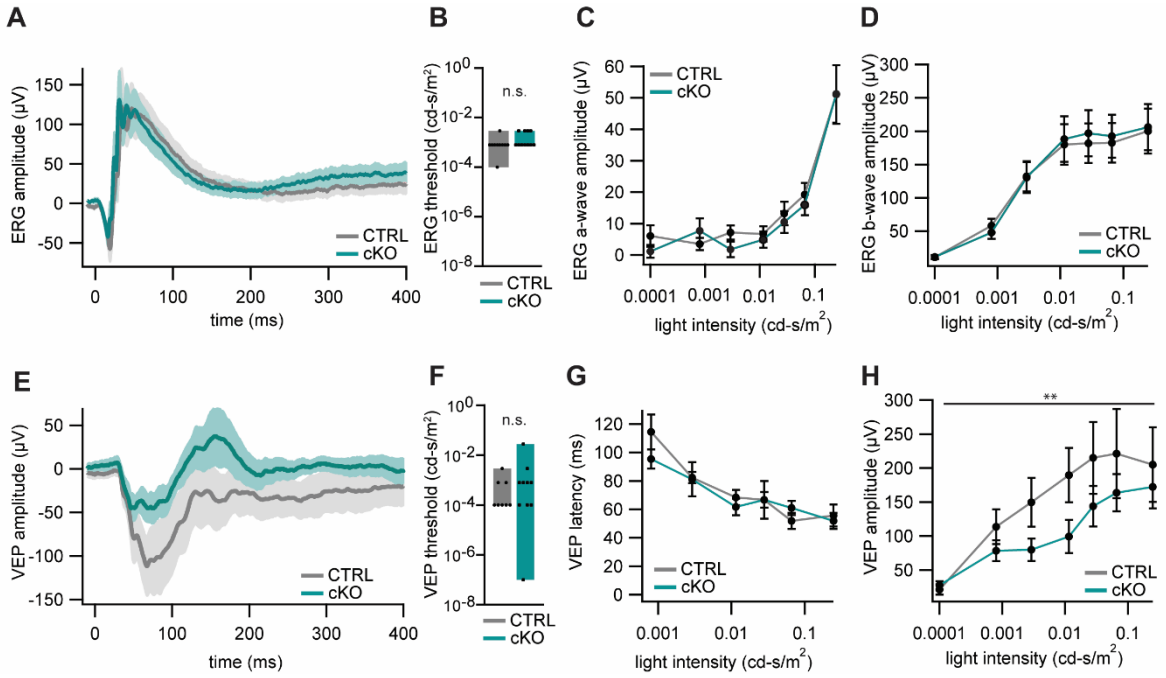

Figure 13: *Cmtm5* cKO mice have normal ERGs but reduced VEP amplitudes. (A-D) Electroretinograms (ERG). **(A)** ERG waveforms in response to light flashes at 0.25 cd-s/m^2 from 11 *Cmtm5* cKO (grand average turquoise, SEM shaded) and 10 CTRL mice (grand average grey, SEM shaded). **(B)** ERG thresholds are similar between CTRL and *Cmtm5* cKO. Unpaired Student´s t-test of the mean ±SEM p= 0.13 **(C,D)** Amplitudes of the ERG A and B waves in response to light flashes of varying intensities in *Cmtm5* cKO (n=11, turquoise) and CTRL mice (n=11, grey; mean ± SEM) are similar between genotypes. 2-way ANOVA **(C)** p= 0.42, **(D)** p= 0.79. **(E-H)** Visual evoked potentials (VEP). **(E)** VEP in response to light flashes at 0.01 cd-s/m^2 from 10 *Cmtm5* cKO (grand average turquoise, SEM shaded) and 9 CTRL mice (grand average grey, SEM shaded) display comparable waveforms dominated by a broad negative wave in both genotypes. **(F)** VEP thresholds are not significantly different between CTRL and *Cmtm5* cKO. Unpaired Student´s t-test of the mean ±SEM with Welch´s correction p= 0.33 **(G-H)** VEP latencies and amplitudes in response to light flashes of varying intensities in *Cmtm5* cKO (n=10, turquoise) and CTRL mice (n=8, grey; means ± SEM). Note that *Cmtm5* cKO and CTRL mice show similar VEP latencies but *Cmtm5* cKO mice display reduced VEP amplitudes compared to CTRL mice. 2-way ANOVA **(G)** p= 0.61 **(H)** p=

0.005. Experiments were performed by Stefan Thom and Nicola Strenzke (Institute for Auditory Neuroscience/InnerEarLab, University Medicine Göttingen).

Taken together, these results show that the axonal pathology following *Cmtm5* deletion in oligodendrocytes causes a functional impairment in the visual system. Given that the axonal degeneration and neuropathology was also observed in other CNS areas it is plausible to hypothesize that other functions are also impaired in mice lacking *Cmtm5*.

4.2.5.1 Analysis of motor capabilities

When looking at the normal cage behavior of *Cmtm5* cKO mice, no apparent impairments, abnormalities or burdens were observed (observations by animal caretakers and myself). Animals behaved and moved normal even with older age and were indistinguishable from their conspecifics belonging to the control group. However, we decided to analyze the motor capabilities of *Cmtm5* cKO mice and respective controls in more detail.

To further characterize the consequences of *Cmtm5* deletion for the animals we used the RotaRod assay, the Open field assay and the CatWalk^{TM} assay to assess their motor capabilities at 6 months of age (Figure 14). The RotaRod assay was used as a basic test for motor capabilities. Counterintuitively, we observed that *Cmtm5* cKO mice perform better in this test and were able to stay longer on the rotating rod compared to mice from the control group (Figure 14A). We further tested these mice in the Open Field assay to assess their movement in an open environment as well as their explorative behavior of an unknown space. In this test, mice usually try to stay close to the box walls and avoid its center. The overall speed and distance covered did not significantly differ between the two groups (Figure 14B, C) and distance covered in the center as well as center visits were largely similar between *Cmtm5* cKO and control mice (Figure 14F, G). However, we found that *Cmtm5* cKO mice moved slower through the center of the box and spent more time in it (Figure 14D, E). It is not clear how these results should be interpreted. One possible explanation could be that an impaired vision leads to a false perception of the environment in *Cmtm5* cKO mice thus deeming the center less dangerous than their control conspecifics do. However, one needs to keep in mind that mice probably rely on somatosensation using their whiskers when exploring an unknown environment. We also used the CatWalk^{TM} assay that allows for an in-depth analysis of different motor capabilities. The run duration and average speed was not significantly altered between the two groups (Figure 14H, I) and all mice displayed a regular walking pattern (Figure 14J). We further analyzed the front and hindlimb stand duration, the contact time of the paws and the base of support (BOS, how far apart the paws are on the ground). These measures can be used as readouts for spinal cord impairments (Timotius et al.,

2021). For example, impairments in the lower spinal cord can lead to an increased stand duration of the hind paws and an increased spacing (Base of support) between the hind paws. We did not observe any significant differences between the two groups at 6 months of age for all these measures (Figure 14K-M).

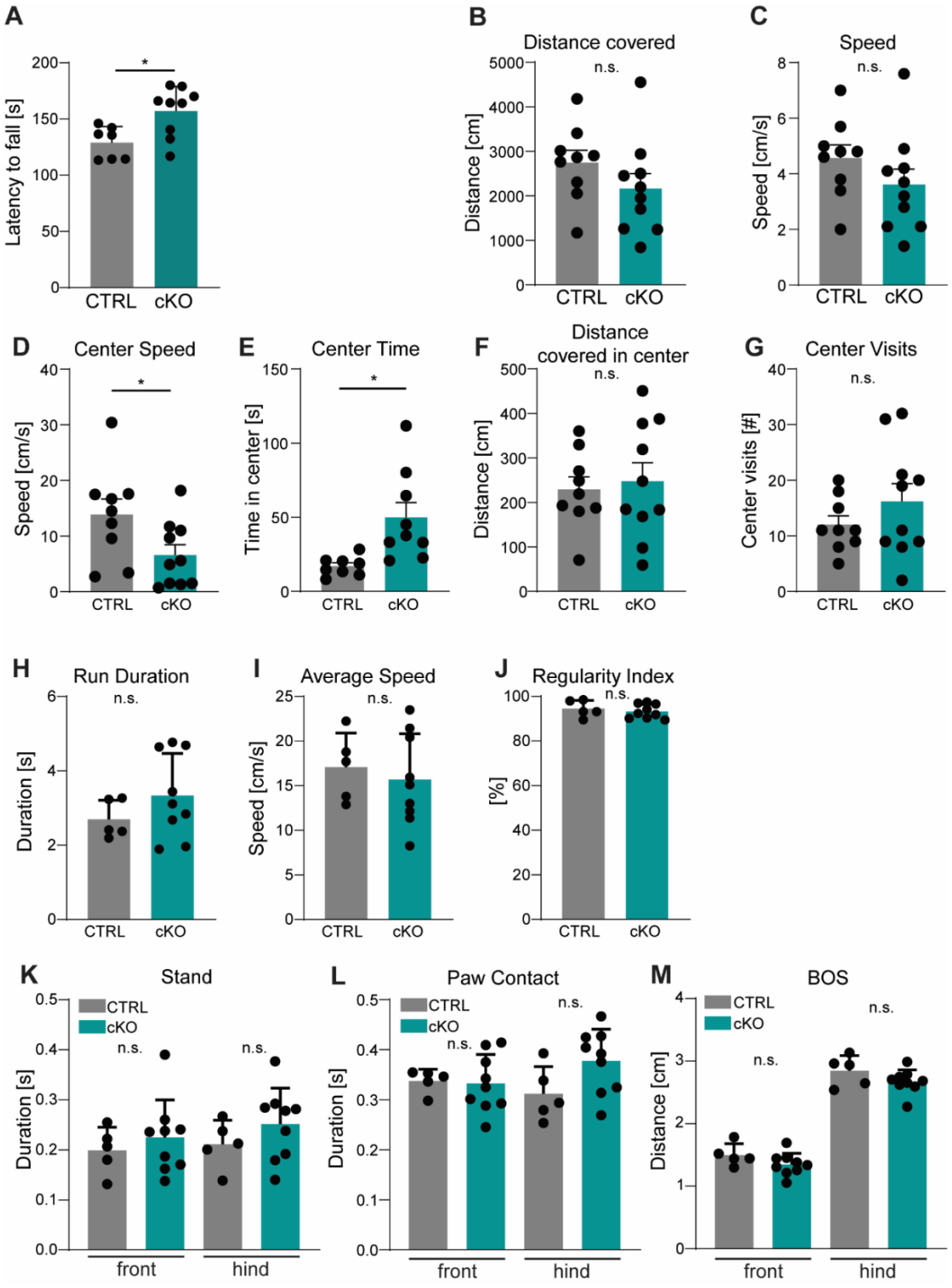

Figure 14: Motor capabilities in *Cmtm5* cKO mice are largely unaltered. Motor function of 6-month-old *Cmtm5* cKO mice and respective controls was assessed using the rotarod assay **(A)**, the open field assay **(B-G)** and the

CatWalk™ assay **(H-M)**. **(A)** *Cmtm5* cKO mice perform better in the RotaRod assay and are able to stay longer on the rotating rod compared to control mice. *Cmtm5* cKO and control mice perform mainly similar in the Open Field test **(B-G)** however, show reduced center speed and spent more time in the center of the box **(D, E)**. *Cmtm5* cKO mice and respective controls perform largely equal in the CatWalk™ **(H-M)**. Run duration **(H)** and average speed **(I)** is not altered and individuals of both groups show regular walking patterns **(J)**. Further, no genotype-dependent difference could be observed when comparing stand duration **(K)**, the time of paw contact **(L)** or the spacing between front limbs and hindlimbs **(M)**. All data points represent individual mice. Bar graphs give mean mean ± SEM. Unpaired Two-tailed Student´s t-test of the mean: **(A)** p= 0.0111, **(B)** p= 0.2120, **(C)** p= 0.2153, **(D)** p= 0.0114 with Welch´s correction, **(E)** p= 0.0418, **(F)** p= 0.7211, **(G)** p= 0.2600 with Welch´s correction, **(H)** p= 0.6073, **(I)** p=0.2607, **(J)** p= 0.5307, **(K)** front: p= 0.5040; hind: p=0.2882, **(L)** front: p= 0.8600; hind: p= 0.0748, **(M)** front: p= 0.1619; hind: p= 0.1697.

In summary, we observed that motor capabilities of *Cmtm5* cKO and control mice are largely similar. At 6 months of age *Cmtm5* cKO mice surprisingly perform better at the RotaRod however other methods showed no difference in motor capabilities between the two groups. These results indicate that the axonal pathology caused by *Cmtm5* deletion in oligodendrocytes is not severe enough to impair motor function in *Cmtm5* cKO mice at an age of 6 months.

4.3 Analysis of constitutive *Cmtm5* mutants

Data presented in the previous chapters came from analysis of mice conditionally lacking *Cmtm5* in oligodendrocytes. We used $Cnp^{Cre/Wt}$ (Lappe-Siefke et al., 2003) for recombination leaving only one functional *Cnp* allele. It was previously reported that *Cnp* heterozygosity causes axonal degeneration and neuropathology at an older age in mice (Hagemeyer et al., 2012). To exclude that the axonal pathology following *Cmtm5* deletion is caused by *Cnp* heterozygosity we also analyzed mice independent of $Cnp^{Cre/Wt}$. Taking advantage of germline recombination we created a mouse line with a body-wide *Cmtm5* deletion ($Cmtm5^{-/-}$) and respective wildtype controls ($Cmtm5^{wt/wt}$).

4.3.1 Body-wide *Cmtm5* mutants show axonal pathology in the CNS

To validate the knock-out of CMTM5 we analyzed myelin derived from $Cmtm5^{-/-}$ and respective controls using immunoblots. CMTM5 is readily detected in wildtype myelin but absent in that derived from brains of $Cmtm5^{-/-}$ (Figure 15A). Note that the abundance of CNP is unaltered between the two genotypes different than in *Cmtm5* cKO. Mice with a body-wide deletion of *Cmtm5* were born at the expected rate, did not display an obvious cage phenotype and reached the same age as wildtype littermate controls.

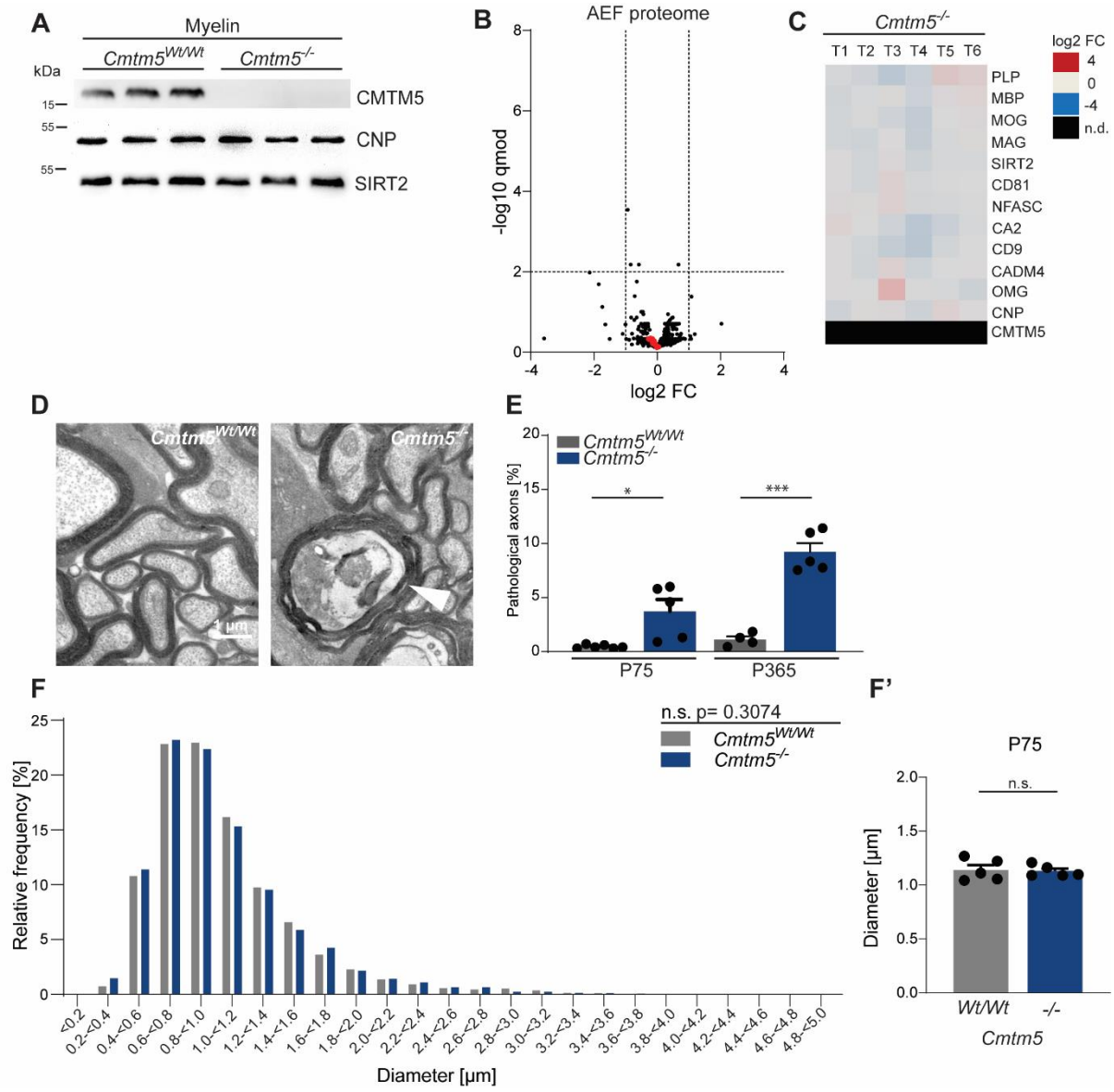

Figure 15: Constitutive *Cmtm5* KO mice show an axonopathy phenotype similar to *Cmtm5* cKO mice. (A-F´) Analysis of mice with a body wide deletion of *Cmtm5* (*Cmtm5*$^{-/-}$) and respective wildtype controls (*Cmtm5*$^{wt/wt}$). **(A)** Immunoblot confirms the absence of CMTM5 in myelin purified from the brain of *Cmtm5*$^{-/-}$ mice. Abundance of SIRT2 and CNP are unaltered between the two genotypes. **(B, C)** Quantitative proteome analysis of the axogliasome enriched fraction (AEF) is largely similar between *Cmtm5*$^{-/-}$ and wildtype controls. **(B)** Volcano plot with data points representing log2-fold change and -log10-transformed q-values of proteins in *Cmtm5*$^{-/-}$ compared to *Cmtm5*$^{W/Wt}$ AEF. Red dots highlight known myelin proteins. Stippled lines indicate thresholds. CMTM5 was not detected in the AEF of *Cmtm5*$^{-/-}$ mice. **(C)** Heatmap showing the relative abundance of selected known myelin proteins in *Cmtm5*$^{-/-}$ compared to the abundance in the AEF derived from controls. Data represents n=3 mice per genotype analyzed as 2 technical replicates per mouse (T1-T6). Note that the relative abundance of most myelin proteins was essentially similar in the AEF of *Cmtm5*$^{-/-}$ and wildtypes. **(D)** Representative electron micrographs of *Cmtm5*$^{-/-}$ and respective control optic nerves. Arrowhead points at pathological profile. Scale bar, 1µm. **(E)** Quantitative assessment of 18-20 random non-overlapping EM micrographs from 4-6 mice per group. Note the progressive increase in pathological appearing axons in optic nerves of *Cmtm5*$^{-/-}$ mice. Two-sided Student´s t-test with Welch´s Correction; P75: p= 0.0406; P365: p< 0.0001 two-sided Student´s t-test. **(F, F´)** Diameter analysis of 700-800 optic nerve axons per mouse. **(F)** Frequency distribution of axonal diameters in the optic nerve is unaltered between the two genotypes. K/S-test p= 0.3074. **(F´)** and mean axonal diameters are unchanged. Two-sided Student´s t-test p= 0.8496. Bar graphs give mean ± SEM; data points represent individual mice. Experimental procedure for Proteome analysis in **(B-C)** was performed by Dörte Hesse and data analysis was performed by Olaf Jahn (Proteomics group, MPI-EM, Göttingen).

Direct oligodendrocyte-axon interactions can be mediated via proteins/components situated at the innermost myelin sheath, the contact area of myelin and the axon. We were interested if *Cmtm5* deletion alters the composition of this fraction. When modifying the protocol for myelin purification it is possible to enrich this compartment, the so called axogliasome enriched fraction (AEF). We subjected the AEF of *Cmtm5*$^{-/-}$ and wildtype controls to quantitative proteome analysis (Figure 15B, C). Surprisingly, the protein abundance was largely similar between the two genotypes (Figure 15B) and the abundance of selected myelin proteins was unchanged (Figure 15C), consistent with the analysis of myelin fractions from *Cmtm5* cKO and respective controls (Figure 6A-B´). Only CMTM5 was not detectable in *Cmtm5*$^{-/-}$ confirming the immunoblot findings.

When analyzing the optic nerves of *Cmtm5*$^{-/-}$ and wildtype controls using TEM we found a significant increase of pathological appearing axons in *Cmtm5*$^{-/-}$ mice at P75 (Figure 15D, E). Optic nerves of 1 year old *Cmtm5*$^{-/-}$ mice showed an even higher number of pathological axons, indicating a progressive advancement of the axonopathy. We further assessed optic nerve diameters in *Cmtm5*$^{-/-}$and wildtype animals at P75 (Figure 15F, F´) but did not find a difference in the frequency distribution of axonal diameters or mean axonal diameters.

Consistent with findings in *Cmtm5* cKO presented in (Figure 6), we find that constitutive *Cmtm5*$^{-/-}$ mice display a progressive axonopathy while myelination of axons appears unaffected. This implies that the axon pathology in *Cmtm5* mutants arises independent of *Cnp* heterozygosity and can thus be attributed to loss of CMTM5 function.

4.3.2 CMTM5 abundance is unaltered in CNS myelin from *Plp* or *Cnp* mutants

PLP and CNP are the most and third-most abundant protein in myelin respectively and mice lacking these proteins show a variety of pathologies including axonal degeneration (Edgar et al., 2009, 2004; Griffiths I et al., 1998). We were interested whether absence of these major myelin constituents influences the abundance of CMTM5. Therefore, we analyzed CNS myelin samples derived from 10-week-old *Cnp* or *Plp* knock-out mice and respective controls (Figure 16). Absence of CNP or PLP did not influence the abundance of CMTM5 in myelin and *vice versa* absence of CMTM5 did not influence the abundance of PLP or CNP in myelin (Figure 6A, Figure 15A).

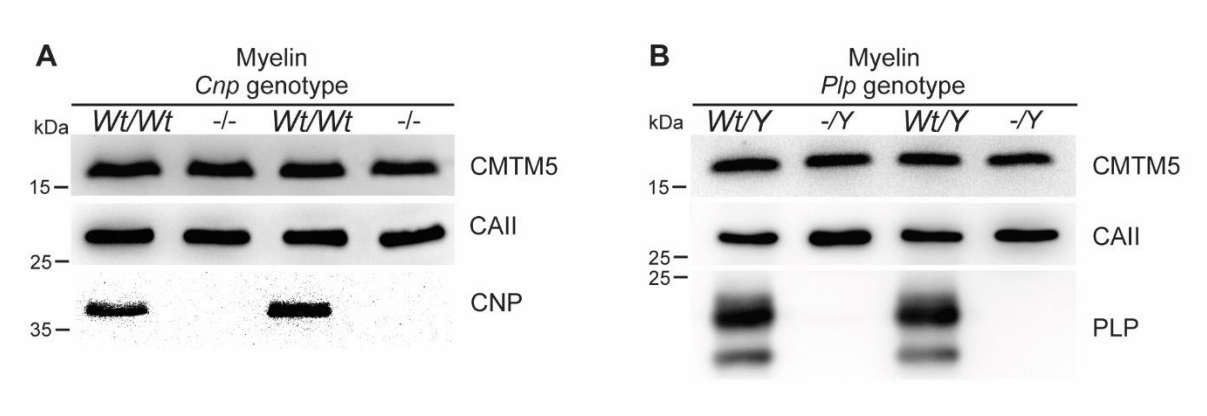

Figure 16: CMTM5 abundance is unaltered in CNS myelin from *Plp* or *Cnp* mutants. (A, B) Immunoblot analysis of myelin purified from the brain of *Cnp* KO **(A)** and *Plp* KO **(B)** mice and respective controls at age P75. CMTM5 abundance in myelin is not altered when CNP or PLP are lacking. Blots show n=2 mice per genotype. CA2 was detected as control.

4.3.3 MCT1 abundance is unchanged in brains of *Cmtm5* knock-out mice

Oligodendrocytes support axons with metabolites and deletion of key proteins in this process can lead to axonal pathology. One important protein in this pathway is the monocarboxylate transporter 1 (*Mct1/Slc16a1*) (Lee et al., 2012; Philips et al., 2021). We were curious if MCT1 protein or mRNA abundance are altered in the absence of CMTM5 contributing to the axonal pathology. Immunoblot analyzes of myelin derived from brains of *Cmtm5*$^{-/-}$ and wildtype mice showed no difference in MCT1 abundance between the experimental groups (Figure 17A).

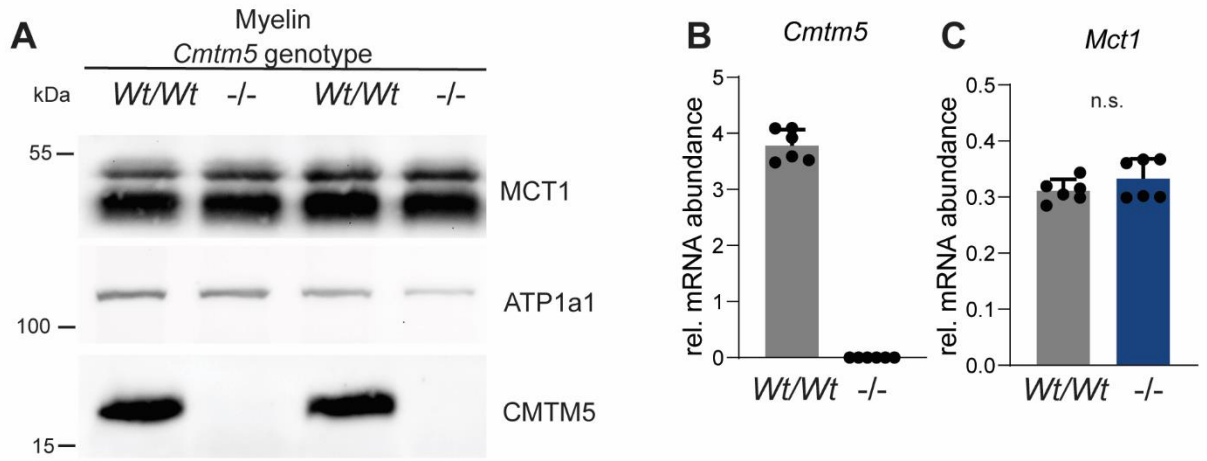

Figure 17: MCT1 protein and mRNA abundance is unaltered in brains of *Cmtm5* KO mice. (A) Immunoblot analysis shows similar MCT1 protein abundance in the myelin purified of *Cmtm5*$^{-/-}$ and control mice. ATP1a1 is shown as control. **(B, C)** qRT-PCR analysis of mRNA isolated from corpus callosum of *Cmtm5*$^{-/-}$ mice and respective controls (n=6 per genotype, 6 months old). **(B)** *Cmtm5* mRNA was not detected in KO tissue. **(C)** *Mct1* mRNA abundance is unchanged between the two groups. Unpaired Two-sided Student´s t-test p= 0.2261. Data presented as mean ± SEM.

We further analyzed *Cmtm5* and *Mct1* mRNA abundance in the corpus callosa of *Cmtm5* KO and wildtype mice. While *Cmtm5* mRNA was readily detected in wildtypes, it was not detectable in *Cmtm5* KO confirming the successful knock-out of *Cmtm5* (Figure 17B). *Mct1* mRNA abundance was unaltered between the two groups (Figure 17C). This data implies that axonal pathology following *Cmtm5* deletion is not influenced by changes in MCT1 abundance in myelin.

4.4 *Cmtm5* deletion in adult animals causes axonal degeneration

So far, data was presented from experiments in which *Cmtm5* was deleted before or during development of the central nervous system. To further examine if the axonal pathology also emerges when *Cmtm5* is recombined in oligodendrocytes post development, we used the $Plp^{CreERT2}$ driver line (Leone et al., 2003) and induced *Cmtm5* recombination via tamoxifen injection at 8 weeks of age ($Cmtm5^{fl/fl}$*$Plp^{CreERT2}$ mice, also termed *Cmtm5* iKO; $Cmtm5^{fl/fl}$, controls). Immunoblot analysis of myelin fractions purified from brains of CTRL and *Cmtm5* iKO mice 4 months post tamoxifen injection (PTI) shows a strong reduction of CMTM5, confirming the successful recombination and deletion of *Cmtm5* (Figure 18A). PLP and SIRT2 were detected as controls and their abundance was not influenced by the reduction of CMTM5. Interestingly, a significant increase of pathological appearing axons was detected in the optic nerves of *Cmtm5* iKO mice when compared with optic nerves from respective controls using TEM (Figure 18B, C).

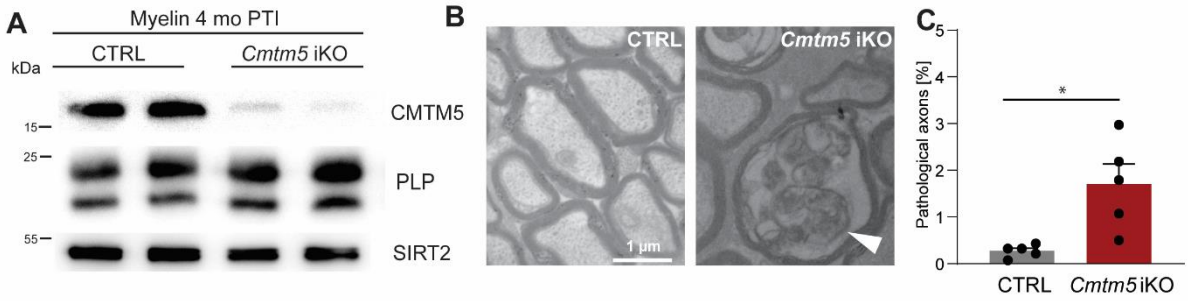

Figure 18: Deletion of *Cmtm5* in adult mice causes axonal degeneration. (A-C) Analysis of mice lacking *Cmtm5* expression in mature oligodendrocytes upon induction by tamoxifen ($Cmtm5^{fl/fl}$*$Plp^{CreERT2}$, iKO) and respective tamoxifen-injected Cre^{ERT2}-negative controls ($Cmtm5^{fl/fl}$, CTRL). **(A)** Immunoblot of myelin purified from the brains of mice 4 months post Tamoxifen injection (PTI). Note that the abundance of CMTM5 is strongly reduced in *Cmtm5* iKO myelin. PLP and SIRT2 were detected as controls. **(B)** Representative electron micrographs of *Cmtm5* iKO and CTRL optic nerves. Arrowhead points at pathological profile. **(C)** Quantification of pathological profiles (20 non-overlapping random images per animal, n=5 mice per genotype). Number of pathological profiles is significantly increased 4 months PTI (p=0.0282 by Two-sided Student´s t-test with Welch´s correction). Bar graphs give mean ± SEM; data points represent individual mice.

In conclusion, this data emphasizes that the function of CMTM5 in preserving axonal integrity is independent of CNS development and probably remains important throughout life.

4.5 CMTM5 is not present in extracellular vesicles from primary oligodendrocytes

Oligodendrocytes support axons via the secretion of vesicles allocating antioxidative proteins and other enzymes (Chamberlain et al., 2021; Frühbeis et al., 2020; Mukherjee et al., 2020). We were interested whether CMTM5 is secreted in EVs targeted at axons. Therefore, we subjected EVs collected from primary oligodendrocytes to immunoblot analysis (Figure 19). While CMTM5 was detected in oligodendrocyte cell lysate it was not present in the exosomal fraction (100K pellet). Successful isolation of EVs was confirmed by the presence of exosomal markers like Alix, CD9 and Flotillin. CMTM5 is not present in oligodendrocyte derived exosomes, however these experiments do not allow the exclusion of CMTM5 being involved at a different step of this support mechanism. It would be necessary to further analyze whether released EVs differ in number between *Cmtm5*$^{-/-}$ mice and respective controls or if presence or absence of CMTM5 alters the cargo that is delivered via EVs to axons.

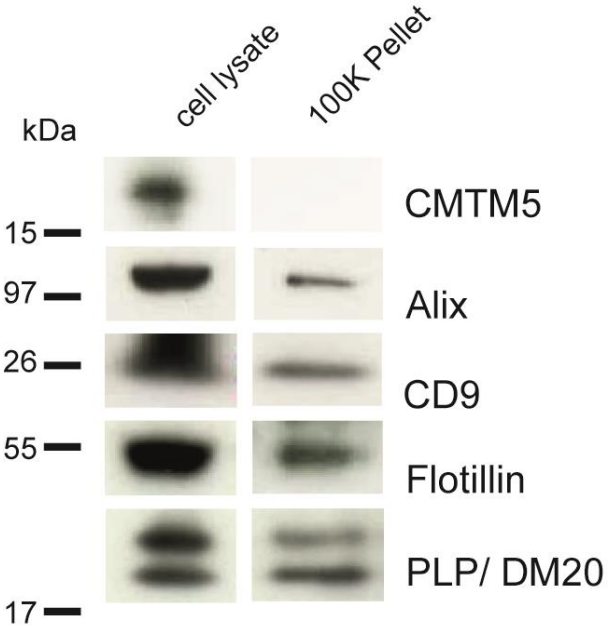

Figure 19: CMTM5 is not present in extracellular vesicles from primary oligodendrocytes. CMTM5 is readily detected in cell lysate from primary oligodendrocytes at DIV6 but not in the exosomal fraction (100K pellet).

Exosomal markers (Alix, CD9, Flotillin) are detected as controls. Analysis was performed by Christina Müller (University of Mainz).

4.6 Axonopathy upon CMTM5 deletion is counteracted by the *Wld^S* mutation

So far it is not clear whether deletion of *Cmtm5* affects neuronal cell bodies or causes mainly the axon to degenerate in a Wallerian-type mechanism. To tackle this question, we first analyzed the number of retinal ganglion cells (RGC) of 1 year old *Cmtm5* cKO mice and respective controls (Figure 20A-C). We found that RGC numbers were largely similar between the two genotypes (Figure 20C), indicating that retinal ganglion cell bodies are preserved. Further, we tested if loss of CMTM5 causes a Wallerian-type axon degeneration (Coleman and Höke, 2020). Using TEM, we analyzed whether presence of the *Wld^S* mutation (Coleman et al., 1998; Lunn et al., 1989) affects the number of pathological axonal profiles following *Cmtm5* deletion (Figure 20D, E). Product of the *Wld^S* mutation is a fusion protein that was shown to protect axons from a variety of different insults, delaying and even preventing axonal degeneration (Coleman et al., 1998; Coleman and Höke, 2020; Lunn et al., 1989). Interestingly, we found that the number of pathological axons was indeed reduced in the presence of *Wld^S* in the optic nerves of 6 months old mice deficient for *Cmtm5* compared with animals without the *Wld^S* mutation (Figure 20E). Taken together, all of these results imply a Wallerian-type pathomechanism in mice lacking *Cmtm5* in oligodendrocytes.

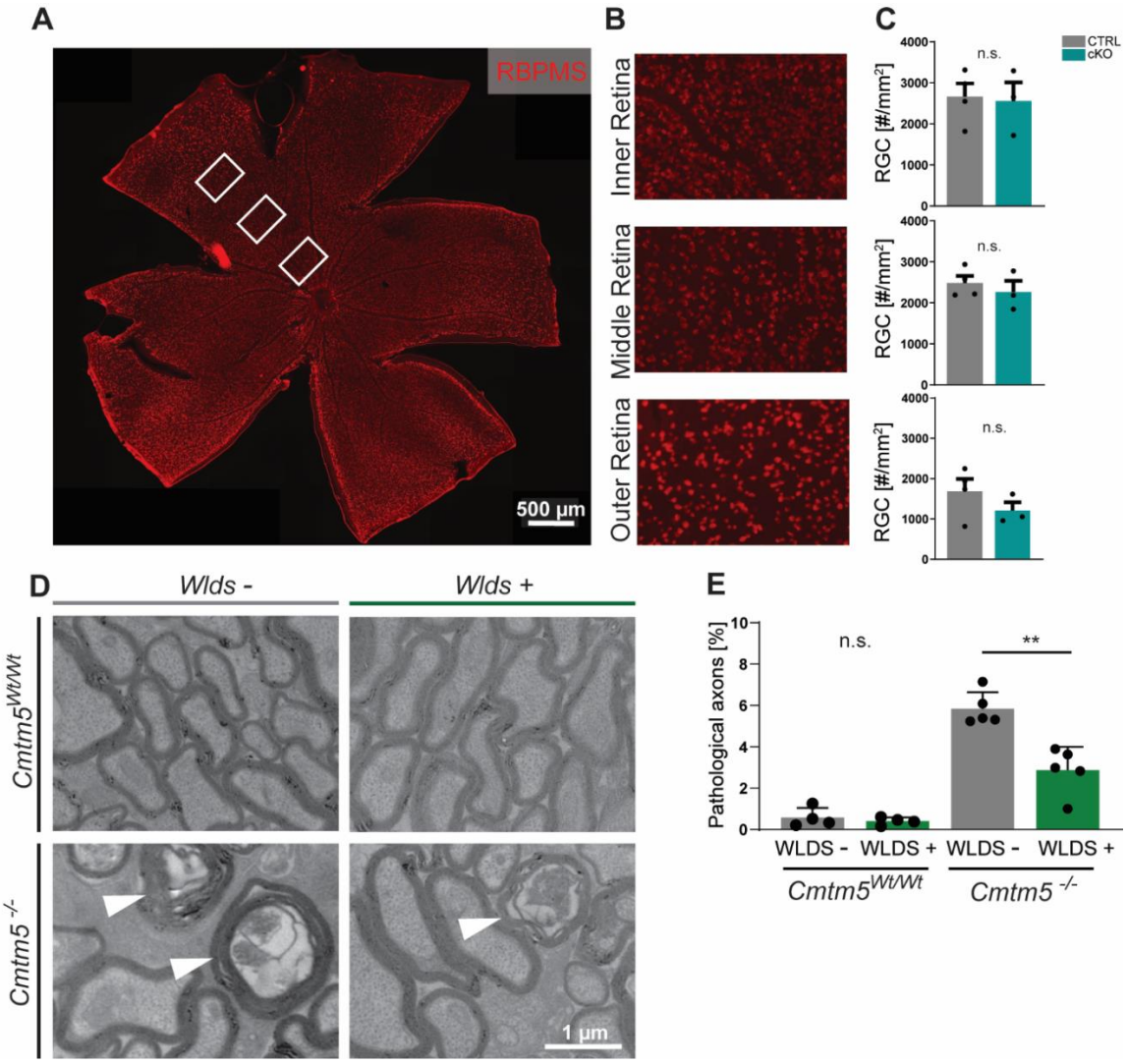

Figure 20: Axonopathy upon *Cmtm5* deletion counteracted by the *Wlds* mutation. (A) Retinae dissected from *Cmtm5* cKO and control mice were immunologically labelled with antibodies against RBPMS detecting Retinal ganglion cells (RGC)**.** Representative image. Scale bar= 500µm. **(B)** Magnification of the inner, middle and outer part of the retina. **(C)** Number of of RGCs is unchanged between CTRL and *Cmtm5* cKO mice. Retinae of 1 year old mice were analyzed. Data represent the mean of 3 non-overlapping areas assessed for each zone (inner, middle outer retina). Unpaired Two-sided Student´s t-test inner part: p= 0.8484; middle part: p= 0.5211; outer part: p= 0.2912). **(D)** Electron micrographs of optic nerves show pathological axons in *Cmtm5*$^{-/-}$ and *Cmtm5*$^{-/-}$ **Wlds+* at 6 months. Arrowheads point at pathological profiles. **(E)** Quantification of degenerated axonal profiles in optic nerves of 6 months old mice. *Cmtm5* deletion causes an increase in pathological profiles, which is significantly reduced in the presence of the *Wlds* mutation. Data correspond to optic nerves from 4-5 mice per group and 20 random non-overlapping EM images analyzed. Unpaired Two-sided Student´s t-test *Cmtm5*$^{wt/wt}$: p= 0.5107; *Cmtm5*$^{-/-}$: p= 0.0471. All data presented as mean ± SEM.

4.7 Function of CMTM5 in the PNS

Previous published findings reported Schwann-cell expressed CMTM6 to be involved in axonal diameter regulation by restricting axonal diameters (Eichel et al., 2020). Data presented in section 4.2.2

showed that CMTM5 is not involved in axonal diameter regulations at least in the CNS. However, we were curious if CMTM5 holds a function in diameter regulations in the PNS. Of note, *Cmtm5* mRNA was detected in the sciatic nerve before and presence of CMTM5 in PNS myelin was also shown (Eichel et al., 2020; Patzig et al., 2011). Conveniently, *Cnp*-Cre can also be used for recombination of *Cmtm5* in Schwann cells and thus allowed for analysis of the PNS of *Cmtm5* cKO mice and respective controls.

4.7.1 Analysis of *Cmtm5* deletion in the PNS

Conventional TEM was used to analyze axonal pathology and myelination status of sciatic nerve axons from *Cmtm5* cKO and respective controls at P75 (Figure 21A-D). In contrast to observations in optic nerve and spinal cord, axonal pathology was absent in the sciatic nerves of *Cmtm5* cKO mice and nearly all axon-Schwann cell units appeared normal (Figure 21B).

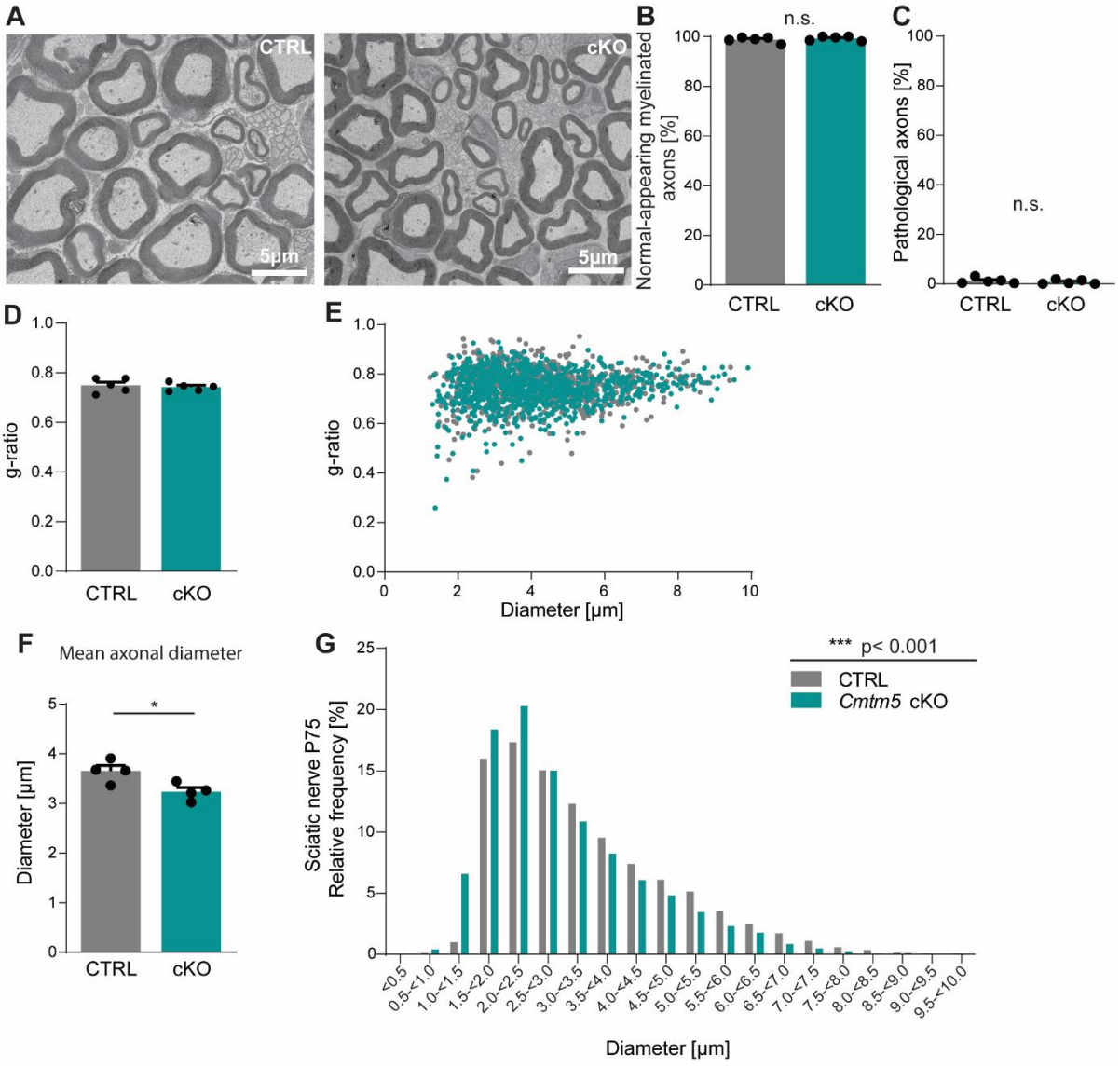

Figure 21: CMTM5 deletion in Schwann cells causes reduced axonal diameters in the sciatic nerve. (A-E) Electron microscope-based analysis of sciatic nerves from *Cmtm5* cKO mice and respective controls at P75. **(A)** Representative electron micrographs of sciatic nerve cross-sections from control and *Cmtm5* cKO mice. Scalebar 5µm. **(B, C)** Analysis of normal appearing myelinated axonal profiles **(B)** and pathological axons **(C)** in the sciatic nerve shows largely unaltered axonal integrity in *Cmtm5* cKO mice compared to control mice. 5 mice per genotype, Student´s t-test B: p=0.4580, C: p=0.4692. **(D&E)** g-ratio analysis of normal appearing myelinated axons in sciatic nerve cross-sections. Mean g-ratio is unaltered between the experimental groups. Student´s t-test p=0.6405 **(D)**. Scatterplot of g-ratios appear largely similar between the groups indicating normal myelination at respective axonal diameters **(E)**. Note the sharp cut-off at 1µm, the expected diameter threshold for PNS axons to be myelinated. **(F&G)** Analysis of axonal diameters based on quantifications on semithin sciatic nerve sections. A shift towards smaller diameter axons (on average -0.4 µm) can be observed in *Cmtm5* cKO sciatic nerves in comparison to control mice **(G)** which is also reflected in the mean axonal diameters per animal **(F)**. 2600-3000 axons analyzed per mouse with 4 mice per genotype. G: K/S Test $p=2.2^{-16}$. F: Student´s t-test p=0.0258. Bar graphs give mean ±SEM.

Further, g-ratios were unaltered between the two groups (Figure 21C, D). However, when analyzing all myelinated axonal profiles on semithin sciatic nerve sections, a shift towards smaller axonal diameters (on average -0.4 µm) could be observed (Figure 21D) which was also reflected in a reduction of mean axonal diameters in *Cmtm5* cKO mice (Figure 21E).

Taken together, the data implies that CMTM5 holds different functions in the CNS and PNS. Deletion of CMTM5 in oligodendrocytes causes axonal pathology in the CNS but axonal diameters are unaltered. When deleted in Schwann cells, sciatic nerve axons appear healthy however show a shift towards smaller diameters. Further, myelination appears to be unaffected in CNS nor PNS and g-ratios remain normal even with a shift towards smaller diameter axons in the PNS.

4.7.2 Analysis of mice lacking *Cmtm5* and *Cmtm6* in the PNS

Sciatic nerve axons in *Cmtm5* cKO mice show on average smaller diameters compared to those of respective controls. Given that axons grow bigger in absence of Schwann cell expressed CMTM6 (Eichel et al., 2020) we were curious how a double knock-out of CMTM5 and CMTM6 affects axonal diameters.

We used Dhh^{Cre} (Jaegle et al., 2003) to specifically knock out CMTM5 and CMTM6 in Schwann cells ($Cmtm5^{fl/fl}$*$Cmtm6^{fl/fl}$*Dhh^{Cre}, also referred to as *Cmtm5/6* dKO; $Cmtm5^{fl/fl}$*$Cmtm6^{fl/fl}$, controls).

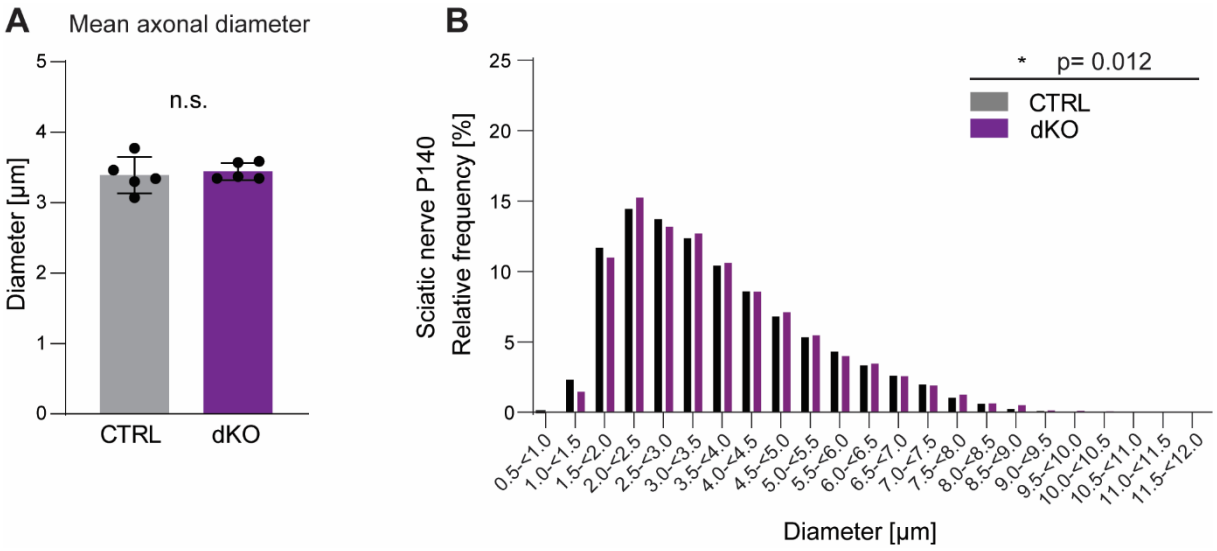

Figure 22: Double knock-out of *Cmtm5* and *Cmtm6* causes slightly increased axonal diameters in the PNS. (A&B) Analysis of axonal diameters in sciatic nerves from *Cmtm5/6* dKO mice and respective controls. **(B)** Frequency distribution of axonal diameters shows a shift towards slightly increased axonal diameters (on average +0.06 µm) in *Cmtm5/6* dKO. K/S-test p= 0.012. Which is not reflected in mean axonal diameters per animal **(A)**. Student´s t-test p= 0.4153. Bar graph gives mean ±SEM. 3500-4100 axons were analyzed per animal and 5 animals were analyzed per genotype. Diameter analysis was performed by Hanna Pies and Maria Eichel (Neurogenetics group, MPI-EM, Göttingen).

Analysis of semi-thin sciatic nerve sections from P140 day old *Cmtm5/6* dKO mice and respective controls showed a slight shift towards larger axon diameters (on average +0.06 µm) (Figure 21A) while the mean axonal diameter per animal is not significantly changed between the two experimental groups (Figure 22B). It is intriguing to hypothesis that 2 proteins of the same protein family expressed by Schwann cells could participate directly or indirectly in the regulation of axonal diameters with opposed effects, however more detailed experiments are necessary to assess the interplay of CMTM5 and CMTM6 in the PNS.

5 Discussion

In this study we established CMTM5 as a novel CNS myelin protein with a relevant role in oligodendrocyte-axon interaction. Our results imply that CMTM5 function is not crucial for myelin biogenesis, structure, or composition. Interestingly, however, ablation of CMTM5 from oligodendrocytes results in early-onset and progressive axonal pathology. Taken together, our findings suggest that CMTM5 holds a relevant function in the long-term support of axonal integrity.

5.1 The novel CNS myelin protein CMTM5 is not essential for myelin biogenesis, composition or structure

The close association of myelin with the myelinated axon allows for multiple cell-cell interactions that support and regulate neuronal activity and ultimately brain function (Nave and Werner, 2021). To identify novel proteins with a potential relevance in this interaction, quantitative mass-spectrometry allows an in-depth analysis of myelin composition (Jahn et al., 2020). While several highly abundant myelin proteins have been previously identified by other methods, less abundant proteins only emerged in recent years as a result of technical improvements.

For example, the three most abundant myelin proteins in the CNS, PLP, MBP and CNP, account for 37.9%, 29.6% and 5.1% of the total myelin proteome, respectively (Jahn et al., 2020), and their functions have been intensely investigated since their discovery (Edgar et al., 2009, 2004; Griffiths I et al., 1998; Lappe-Siefke et al., 2003; Lüders et al., 2017; Roach et al., 1985; Rosenbluth, 1980). However, advancements in recent years allowed the identification of hundreds of proteins in myelin, many of which have not yet been well investigated, at least not in the context of the CNS or their function in oligodendrocytes and myelin.

One of these novel candidates is CMTM5, a relatively low abundant protein representing about 0.027% of the total CNS myelin proteome (Jahn et al., 2020). Previous studies showed a specific expression of *Cmtm5* mRNA in cells of the oligodendrocyte lineage in mice and humans (Jäkel et al., 2019; Zhang et al., 2014; Zhou et al., 2020). Further, CMTM5 was detected in myelin derived from both mice and humans, and its abundance was approximately similar in the CNS myelin fractions of both species (Gargareta et al., 2022; Jahn et al., 2020). Of note, *Cmtm5* mRNA was previously detected in the PNS where it shows a high specificity to Schwann cells (Eichel et al., 2020; Gerber et al., 2021) and its localization to the myelin sheath in the PNS was shown as well using immunoelectron microscopy (Patzig et al., 2011).

In the present study CMTM5 was confirmed as a novel CNS myelin protein following our additional observations that:

1. Its abundance is highly enriched in purified CNS myelin fractions compared to brain lysate according to immunoblots.

2. It shows a specific localization to the myelin sheath by immunohistochemistry.

3. Its abundance increases during postnatal brain development similar to other known myelin proteins, coinciding with myelin formation.

CMTM5 is a member of the chemokine-like factor-like MARVEL-transmembrane domain containing (CMTM) protein family (Han et al., 2003) which has been mainly associated with roles in regulating cancer immunity (Burr et al., 2017; Mezzadra et al., 2017; Shao et al., 2007; Xiao et al., 2015; Yuan et al., 2020) and male fertility (Fujihara et al., 2018; Liu et al., 2019). While the relevance of CMTM proteins for tumor immunity has been studied intensely in the past years, not much is known about their functions in the nervous system.

Recently the protein CMTM6 was reported to play a role in the regulation of axonal diameters in the peripheral nervous system (Eichel et al., 2020). Deletion of CMTM6 from Schwann cells, the myelinating glial cells of the PNS, caused axons to grow in diameter indicating that CMTM6 restricts axonal diameters in the PNS, a so far unknown function of myelinating glial cells. This observation as well as the identification of CMTM5 as a potential functional paralog expressed in CNS myelin, motivated us to further investigate the function of CMTM5 in the nervous system.

Following our identification of CMTM5 as a novel CNS myelin protein, we were interested whether its deletion from oligodendrocytes could affect the generation and structure of myelin. We found that myelination appeared normal in *Cmtm5*-mutants and that the myelin protein composition was largely unaffected by absence of CMTM5. Given the comparatively low abundance of CMTM5 in CNS myelin, it is not unexpected that its deletion does not cause structural alterations of the myelin sheath as observed in mice lacking more abundant proteins like PLP or CNP (Edgar et al., 2009, 2004; Griffiths I et al., 1998; Lappe-Siefke et al., 2003).

Here we identified CMTM5 as a novel CNS myelin protein with a functional relevance for oligodendrocyte-axon interaction: CMTM5 does not seem to be involved in axonal diameter regulation in the CNS. However, its absence in oligodendrocytes leads to axonal pathology without affecting myelin composition, biogenesis or structure.

5.2 The *Cmtm5*-mutant, a novel model to investigate axonal pathology in the CNS

5.2.1 Early-onset, progressive axonopathy when oligodendrocytes lack CMTM5

We made the interesting observation that deletion of CMTM5 in oligodendrocytes caused an early onset, progressive axonal pathology implying that CMTM5 plays a role in the preservation of axonal integrity. Importantly, we also observed axonopathy in mice in which deletion of *Cmtm5* is independent of the presence of the $Cnp^{Cre/Wt}$ allele. Indeed, the observed axonopathy in $Cmtm5^{-/-}$ and $Cmtm5^{fl/fl}$*$Plp^{CreERT2}$ mice confirms that the emergence of pathology can be attributed to loss of CMTM5 function and is not caused by *Cnp* heterozygosity as observed before at higher age (Hagemeyer et al., 2012).

Loss of CMTM5 function caused an axonopathy in various white matter areas, allowing the assumption that CMTM5 holds a general function in maintaining axonal integrity. This is also underlined by the observation, that deletion of CMTM5 in adult animals causes axonal pathology after nervous system development is largely completed. Further, given that CMTM5 protein abundance as well as *Cmtm5* mRNA expression (Thakurela et al., 2016) remains stable in myelin also in older age, we hypothesize that the function of CMTM5 in maintaining axonal integrity in the CNS remains relevant throughout life.

Which fibers are affected by loss of CMTM5? Findings in mice lacking Myelin Associated Glycoprotein (MAG) suggested that larger axons are more susceptible to disturbance of the axon-myelin unit, at least following an injury in the PNS (Palandri et al., 2015). In contrast, a study analyzing spinal cords of Multiple Sclerosis (MS) patients suggested that especially smaller diameter axons can be affected by the disease (Lovas et al., 2000). Therefore, we aimed to assess if axons with larger or smaller diameters are more affected by loss of CMTM5 function. Yet, a pathological profile does not necessarily match the size of the previously healthy axon and it is thus difficult to assign the correct axonal diameter to a degenerated profile. This is particularly apparent when analyzing axonal swellings, which can increase axonal diameter dimensions manifold (Yong et al., 2020, 2019). We further investigated this hypothesis by using FIB-SEM analysis and 3D reconstruction of optic nerve axons, but found only very few profiles with axonal swellings. Further, pathological axonal profiles largely presented as myelin whorls without connection to something that could be considered as a healthy axon. However, we did not find changes in the frequency distribution of axonal diameters. Together, this implies that degeneration affects myelinated axons independent of their diameter.

We observed a reduction of VEP amplitudes in the optic tract probably best explained by the reduction of healthy axonal profiles following *Cmtm5* deletion in oligodendrocytes. In contrast, we did not observe striking functional impairments in our assays measuring motor functions. The electrophysiological VEP measurements might be able to pick up more subtle differences in axonal loss between CTRL and *Cmtm5* cKO mice. However, given the observation that axons also degenerate in the spinal cord, and the general progressive nature of the pathology, it is reasonable to hypothesize that *Cmtm5* deficient mice may show impaired cage behavior and poor performance in motor tests if assessed at older age, as previously reported for mice lacking PLP (Griffiths I et al., 1998).

5.2.2 Axonopathy following *Cmtm5* deletion is ameliorated by presence of the *Wld^s* mutation

Our observations that retinal ganglion cells are spared by *Cmtm5* deletion and presence of the *Wld^s* mutation ameliorates the axonopathy caused by loss of CMTM5 suggest a Wallerian-like mechanism of axon degeneration. Presence of the *Wld^s* mutation was shown to protect axons from different types of physical, toxic or genetic insults or at least delayed axonal degeneration (Coleman et al., 1998; Coleman and Höke, 2020; Lunn et al., 1989).

It is currently unknown whether *Wld^s* reduces axonal degeneration in *Cmtm5*-mutant mice or rather delays the degenerative process. It would thus be interesting to assess whether the dynamic of axonal pathology in the presence of *Wld^s* changes from early postnatal brain development throughout adulthood and up into higher age in future follow-up experiments.

The axon protective function of *Wld^s* is long known. More recently, the underlying pathways were updated by findings in mice and flies, analyzing the enzyme Sterile alpha and TIR motif containing 1 (SARM1) and its fly ortholog dSarm, respectively (Gerdts et al., 2013; Osterloh et al., 2012). Both the product of the *Wld^s* mutation, a Nicotinamide Nucleotide Adenylyltransferase 1 (NMNAT1) fusion protein, and SARM1 can play central roles mediating axonal degeneration (Coleman et al., 1998; Essuman et al., 2017; Mack et al., 2001). In this pathway axonal survival relies on stable supply of Nicotinamide Nucleotide Adenylyltransferase 2 (NMNAT2), or the *Wld^s* produced NMAT1 fusion protein, and stable NAD^+ levels along the axon (di Stefano et al., 2015; Gilley and Coleman, 2010; Wang et al., 2005). Targeting this pathway showed promising results in the amelioration of some disease models affecting axonal integrity (Coleman and Höke, 2020), while axonal degeneration was not ameliorated in others. For example, presence of *Wld^s* was shown to alleviate degeneration in models of glaucoma (Williams et al., 2017), but did not rescue the axonal pathology in mice lacking CNP or PLP (Edgar et al., 2009, 2004). Further, presence of *Wld^s* or loss of SARM1 did not prevent axonal pathology

in transgenic SOD1 mice serving as a model for amyotrophic lateral sclerosis (Fischer et al., 2005; Peters et al., 2018).

It is intriguing to analyze in which diseases or their respective animal models the Wallerian-degeneration pathway can be targeted to ameliorate the cause of axonal degeneration, especially with the emergence of small molecules targeting SARM1, activity which are developed toward application in clinical use (Bosanac et al., 2021; Hughes et al., 2021; Loring et al., 2020). It will be particularly interesting whether these SARM1 inhibitors could counteract axonal pathology caused by disturbance of the axon-myelin unit.

Notably, to the best of our knowledge, CMTM5-deficient mice present the first model in which presence of the *Wld*^{s} mutation counteracts the axonal pathology caused by deletion of a CNS myelin protein. This indicates that axonal degeneration in *Cmtm5*-mutants follows a Wallerian-like degeneration. Yet, it remains elusive how CMTM5 mediates its function and why axons degenerate when oligodendrocytes lack CMTM5.

5.2.3 Pathomechanism in *Cmtm5*-mutants differs from other myelin mutants

The deletion of myelin proteins was linked to the emergence of axonal pathology before, for example in mice lacking PLP or CNP (Edgar et al., 2009; Griffiths I et al., 1998). Interestingly, *Plp1* and *Cnp*-mutant mice indeed share some similarities in their pathological phenotype with that observed in *Cmtm5*-mutants. For example, mice lacking PLP (Edgar et al., 2004; Griffiths I et al., 1998), CNP (Edgar et al., 2009; Lappe-Siefke et al., 2003) or CMTM5 all show an early-onset, progressive axonopathy while presenting normal myelination (*Cmtm5* KO) or only moderate hypomyelination (*Plp1* and *Cnp* KO). However, the emergence of neuropathology including APP-positive axonal swellings, microgliosis and astrogliosis occurs at a much earlier age in *Plp*-mutants (de Monasterio-Schrader et al., 2013; Edgar et al., 2004; Griffiths I et al., 1998; Steyer et al., 2020) or *Cnp*-mutants (Edgar et al., 2009; Lappe-Siefke et al., 2003; Wieser et al., 2013) compared to *Cmtm5*-mutants where it emerges at a later timepoint following the onset of axonal pathology. Moreover, the presence of the *Wld*^{s} mutation ameliorates axonal pathology mediated by loss of CMTM5 function, but does not seem to affect the emergence of pathological axonal profiles in *Plp1* and *Cnp*-mutants (Edgar et al., 2009, 2004) notwithstanding the latter observed has not been quantified. Taken together, these findings suggest that the pathology in *Cmtm5*-mutants follows a different mechanism than in *Plp1* and *Cnp*-mutants.

Deletion of *Cnp* and *Plp1* lead to alterations in myelin structure and stability and cause hypomyelination but both mutants show considerable amounts of compacted myelin. In contrast, loss

of MBP leads to an inability of oligodendrocyte to form compacted myelin sheaths (Rosenbluth, 1980). Interestingly, complete deficiency of compact myelin as observed in *shiverer* mice lacking *Mbp* (Roach et al., 1985) does not seem to cause axonal degeneration (Griffiths I et al., 1998; Ou et al., 2009; Uschkureit et al., 2000). This indicates, that axonal integrity does depend more on the functionality of the myelin sheath by which it is enwrapped than on the presence of myelin *per se*. However, one needs to take into account that *shiverer* mice have a shortened life expectancy, dying with seizures at an age of 2-5 months (Popko et al., 1987). This emphasizes the importance of a functional myelination in the central nervous system.

5.3 Divergent role of CMTM5 in the regulation of axonal diameters in CNS and PNS

Myelination of axons allows for saltatory signal propagation enhancing the signaling speed several times (Tasaki, 1939). Notably, this is not the only mechanisms by which the transmission of electrical signals along axons can be modulated. The diameter of the transmitting fiber also plays an important role and can influence action potential transmission and thus ultimately finetune nervous system function (Hartline and Colman, 2007). Interestingly, next to the recently described CMTM6 we here find CMTM5 as another member of the CMTM protein family to be involved in the regulation of axonal diameters at least in the PNS.

Cmtm5 mRNA was detected in Schwann cells and presence of CMTM5 in PNS myelin was shown earlier (Eichel et al., 2020; Gerber et al., 2021; Patzig et al., 2011). Yet, the functional role of CMTM5 in the PNS was never investigated. Here we report that absence of CMTM5 in Schwann cells does not alter myelination of sciatic nerve axons, similarly to findings in mice deficient for CMTM6 in Schwann cells (Eichel et al., 2020). However, while deletion of CMTM6 in Schwann cells causes enlarged axon diameters we find that absence of CMTM5 coincides with moderately but significantly reduced axonal diameters. Further, deletion of both, CMTM5 and CMTM6, leads to almost wildtype axonal diameters, with a slight shift towards larger axon diameters (on average 60 nm).

Do CMTM5 and CMTM6 modulate axonal diameters with opposing effects? It is of note that these results come from different studies including different *Cre*-drivers for the recombination of the target gene in Schwann cells ($Cnp^{Cre/Wt}$ for *Cmtm5* cKO and *DhhCre* for *Cmtm5/6* dKO and *Cmtm6* cKO in Eichel et al., 2020) and different timepoints. A more detailed side-by-side analysis of *Cmtm5* next to *Cmtm6* cKO, the double knock-out and the respective controls using *DhhCre* would thus be necessary to validate this pilot observation at the required technical standard.

Albeit being the first known myelin protein involved in restricting axonal diameters in the PNS, CMTM6 was not the first reported myelin protein involved in regulation of axonal diameters by Schwann cells. The myelin protein MAG was shown to play an important role in axonal diameter growth by a mechanism involving increased neurofilament phosphorylation, thus increasing neurofilament spacing (Garcia et al., 2003; Yin et al., 1998). Of note, the neurofilament spacing was unchanged in peripheral axons of mice lacking CMTM6 in Schwann cells suggesting a different mode of diameter regulation (Eichel et al., 2020).

Further axon intrinsic mechanisms involved in the modulation of axonal diameters include α-Adducin and PTEN (Phosphatase and Tensin homolog) and deletion of either of them caused enlarged axon diameters at least in the CNS (Goebbels et al., 2017; Leite et al., 2016). To date, no myelin or oligodendrocyte proteins have been reported to directly affect axonal diameters in the CNS. Notably, axonal diameters were reported to be reduced in the CNS of *shiverer* mice (Kirkpatrick et al., 2001) but our own analysis showed unchanged axonal calibers in the optic nerve of *shiverer* mice at least at an age of 10 weeks (currently unpublished data). However, given the results from the PNS it is plausible that oligodendrocytes could also regulate axonal shape and diameter either by direct cell-cell interactions or via physical restriction and repulsion via their myelin sheath, potentially allowing the fine tuning of neuronal networks.

We were thus interested whether deletion of *Cmtm5* in oligodendrocytes coincides with changes in axonal diameters in the CNS. However axonal diameters were unaltered in the optic nerves of 10 week and one year old mice lacking CMTM5 in oligodendrocytes.

For now, the mechanism of diameter regulation by CMTM5 and CMTM6 remains elusive and it is not clear whether this effect would be directly mediated by CMTM5 or CMTM6 via an interaction with a target protein or if the deletion of CMTM5 or CMTM6 has an indirect effect on axon diameters. Nonetheless, it is interesting that 2 proteins of the same protein family seem to play a role in the modulation of axonal diameters in the PNS and that absence of either CMTM5 or CMTM6 causes axonal diameter to grow or shrink, without altering myelination status or integrity of the respective myelinated axon.

Taken together it appears that CMTM5 mediates different functions in the PNS and CNS. While we did not observe changes in myelin biogenesis or structure in either of the systems, CMTM5 deletion coincided with decreased axonal diameters yet unaltered axonal integrity in the PNS while ablation of CMTM5 in oligodendrocytes did not alter axonal diameters but was followed by a progressive axonopathy and late-stage neuropathology in the CNS.

5.4 How can CMTM5 affect axonal integrity?

Myelinated axons depend on support from oligodendrocytes and disturbance of this interaction is a hallmark that can be observed in different diseases affecting the nervous system (Franklin et al., 2012; Stadelmann et al., 2019; Wolf et al., 2021). This is further underlined by findings in animal models were the functionality of the axon-myelin unit is perturbed, leading to detrimental effects for axonal integrity and nervous system function (Edgar et al., 2009, 2004; Y. Lee et al., 2012; Mei et al., 2016; Philips et al., 2021).

Indeed, the concept of axonal support by oligodendrocytes is longer known and was intensely studied in recent years. These mechanisms are thought to include the supply of metabolites (pyruvate/lactate) via monocarboxylate transporters (Fünfschilling et al., 2012; Y. Lee et al., 2012; Philips et al., 2021; Trevisiol et al., 2020) , the allocation of antioxidative proteins and enzymes via extracellular vesicles (Chamberlain et al., 2021; Frühbeis et al., 2020; Mukherjee et al., 2020) as well as the modulation of axonal transport (Edgar et al., 2004; Frühbeis et al., 2020).

Our data indicate that CMTM5 is also involved in the support of long-term axonal integrity. However, it remains obscure why CNS axons degenerate after *Cmtm5* deletion or how CMTM5 mediates its supportive function. Our finding that *Wld*^{s} modulates axonal pathology in *Cmtm5*-mutants does not provide much mechanistic insight about CMTM5 *per se* but points to a Wallerian-like mechanism of axonal degeneration downstream of CMTM5 function.

We explored the hypothesis of axonal energy imbalances following the reported finding that lack of the mono-carboxylate transporter 1 (MCT1/*Slc16a1*) in oligodendrocytes can cause axonal pathology in the CNS (Lee et al., 2012; Philips et al., 2021). However, *Mct1* mRNA levels were unchanged in the brains of mice lacking CMTM5 and MCT1 protein levels were unaltered in purified myelin from *Cmtm5*-deficient mice. Further, the axonal pathology in mice lacking MCT1 arises at a much higher age compared to *Cmtm5*-mutants (Lee et al., 2012; Philips et al., 2021). Yet, we can´t exclude that CMTM5 is involved in maintaining axonal metabolic demand by means independent of MCT1. An attractive model to study potential alterations in axonal energy levels are axonal expressed ATP sensors which were successfully used in studies analyzing *Plp1*-mutants before (Imamura et al., 2009; Trevisiol et al., 2020, 2017). Further, given that axonal NAD^+ level play an important role for the initiation of Wallerian degeneration via NMNAT2 and SARM1 (Coleman and Höke, 2020; di Stefano et al., 2015; Essuman et al., 2017; Wang et al., 2005), it would be interesting to study potential alterations in NAD^+ dynamics in *Cmtm5*-mutants. This can be assessed by using the respective NAD sensors that recently emerged (Zou et al., 2020) in combination with induced stress for example by energy deprivation or high intensity stimulation in *Cmtm5*-mutants *ex vivo.*

Oligodendrocytes support axons by releasing extracellular vesicles (EV) modulating axonal transport and making them more resilient against oxidative stress and starvation *in vitro* (Chamberlain et al., 2021; Frühbeis et al., 2020, 2013; Krämer-Albers et al., 2007). We wanted to investigate whether CMTM5 could be involved in axonal support via EVs secreted by oligodendrocytes. Interestingly, CMTM5 was reported to be released via EVs in transfected cancer cell lines (Li et al., 2010). However, CMTM5 was not detected in EVs derived from cultivated primary oligodendrocytes. Oligodendrocytes derived from *Plp* and *Cnp* knock-out mice were reported to show impaired exosome release and secreted EVs were not as protective as exosomes from wildtype mice (Frühbeis et al., 2020). One could hypothesize that the loss of CMTM5 function might also directly or indirectly influence EV release or composition, making axons in *Cmtm5* KO mice more vulnerable towards different stressors.

Unfortunately, given the long duration of these follow-up experiments and the limited time for the study we were not able to perform these experiments as part of this thesis.

By structure prediction, CMTM5 does not expose a chemokine-like motif extracellularly. Alternatively, it seems plausible that CMTM5 could be involved in axonal maintenance by stabilizing protein localization in *cis* as it was reported for other CMTMs (Burr et al., 2017; Mezzadra et al., 2017; Mohapatra et al., 2021). Given that the periaxonal space is the closest contact zone and possibly a major transcellular interaction site between the axonal membrane and the adaxonal myelin, it appears interesting to further study the ultrastructural localization of CMTM5 in that area. We find CMTM5 abundant in the axogliasome-enriched fraction (AEF), suggesting its presence in this compartment.

Taken together, the mechanism by which CMTM5 exerts its axon-supportive function remains elusive at this time, and it will be a crucial next step to identify the relevant pathways that are affected by loss of CMTM5 function. We speculate that CMTM5 is involved in a “fail-safe” system that axons rely on to counter potential metabolic or oxidative stress also under normal physiological conditions. Hence, loss of CMTM5 function may make it more likely to shift the balance against axonal survival under stress, leading to increased vulnerability of CNS axons and ultimately axonal degeneration as observed in *Cmtm5*-deficient mice.

5.5 Outlook

We aim to identify novel proteins with a relevant function in oligodendrocyte-axon interaction. In this thesis, we identified CMTM5 as a low abundant CNS myelin protein with an interesting function in the nervous system, as its deletion from oligodendrocytes caused an early onset, progressive axonal

pathology without affecting myelin biogenesis and composition. We hypothesize that CMTM5 is involved in the maintenance and support of axonal integrity in the CNS.

Following our hypothesis, it would be attractive to analyze whether an increase of CMTM5 abundance in oligodendrocytes and myelin could counteract axonopathy in genetically or pharmacologically induced models of axonal loss *in vivo*.

As discussed in section 5.4, the underlying mechanism by which CMTM5 mediates its function remains obscure and it will be important to identify relevant interaction partners or pathways. We currently aim to achieve this by using BulkRNAseq analysis of isolated oligodendrocytes and neurons to identify altered pathways in mice lacking *Cmtm5*. Further, we approach this question using BlueNative gel experiments combined with mass spectrometric analysis of myelin derived from *Cmtm5*-deficient mice and respective wildtype controls to identify potential direct interaction partners. Following identification of relevant targets, it will be important to assess whether potential candidates could be efficiently targeted (pharmacologically) to improve axonal integrity in the CNS.

Given that axons show very limited regenerative capacity in the mammalian CNS, it is particularly important to stop them from entering a “fatal-state” in which axon degeneration becomes inevitable (Yong et al., 2020, 2019). Considering that SARM1 inhibitors (see section 5.4) could hold this potential (Bosanac et al., 2021; Hughes et al., 2021; Loring et al., 2020) it will be interesting to assess how these molecules maintain axonal integrity following an insult to oligodendrocytes or the axon-myelin unit. We here show that, in principle, it is possible to ameliorate axonal pathology caused by deletion of a CNS myelin protein using *Wld*^{S}. Targeting the Wallerian degeneration pathway appears as a promising route to improve axonal integrity in CNS and PNS diseases. However, the identification of relevant disease-modulating proteins and pathways in this context will remain a crucial endeavor, especially keeping in mind that regulation of the Wallerian degeneration pathway might not be beneficial for all diseases affecting axons in the CNS and PNS.

Intriguingly, findings in the past years, as well as ongoing technical advances in the field indicate that a promising compartment for candidate identification is the axon-myelin unit, by which oligodendrocytes and Schwann cells probably mediate most of the vital functions for axons they myelinate.

6 References

Ambrozkiewicz MC, Schwark M, Kishimoto-Suga M, Borisova E, Hori K, Salazar-Lázaro A, Rusanova A, Altas B, Piepkorn L, Bessa P, Schaub T, Zhang X, Rabe T, Ripamonti S, Rosário M, Akiyama H, Jahn O, Kobayashi T, Hoshino M, Tarabykin V, Kawabe H. 2018. Polarity Acquisition in Cortical Neurons Is Driven by Synergistic Action of Sox9-Regulated Wwp1 and Wwp2 E3 Ubiquitin Ligases and Intronic miR-140. *Neuron* **100**:1097-1115.e15. doi:10.1016/j.neuron.2018.10.008

Attwell D, Laughlin SB. 2001. An Energy Budget for Signaling in the Grey Matter of the Brain. *Journal of Cerebral Blood Flow and Metabolism* **10**:1133–1145. doi:10.1097/00004647-200110000-00001

Basser PJ, Mattiello J, Lebihan D. 1994. MR Diffusion Tensor Spectroscopy and Imaging. *Biophysical Journal* **66**:259–267. doi:10.1016/S0006-3495(94)80775-1

Bélanger M, Allaman I, Magistretti PJ. 2011. Brain energy metabolism: Focus on Astrocyte-neuron metabolic cooperation. *Cell Metabolism*. doi:10.1016/j.cmet.2011.08.016

Bosanac T, Hughes RO, Engber T, Devraj R, Brearley A, Danker K, Young K, Kopatz J, Hermann M, Berthemy A, Boyce S, Bentley J, Krauss R. 2021. Pharmacological SARM1 inhibition protects axon structure and function in paclitaxel-induced peripheral neuropathy. *Brain*. doi:10.1093/brain/awab184/6272578

Burr ML, Sparbier CE, Chan YC, Williamson JC, Woods K, Beavis PA, Lam EYN, Henderson MA, Bell CC, Stolzenburg S, Gilan O, Bloor S, Noori T, Morgens DW, Bassik MC, Neeson PJ, Behren A, Darcy PK, Dawson SJ, Voskoboinik I, Trapani JA, Cebon J, Lehner PJ, Dawson MA. 2017. CMTM6 maintains the expression of PD-L1 and regulates anti-Tumour immunity. *Nature* **549**:101–105. doi:10.1038/nature23643

Buscham TJ, Eichel-Vogel MA, Steyer AM, Jahn O, Strenzke N, Dardawal R, Memhave TR, Siems SB, Müller C, Meschkat M, Sun T, Ruhwedel T, Möbius W, Krämer-Albers E-M, Boretius S, Nave K-A, Werner HB. 2021. Progressive axonopathy when oligodendrocytes lack the myelin protein CMTM5. *Bioarchive*. doi:10.1101/2021.11.22.469514

Chamberlain KA, Huang N, Xie Y, LiCausi F, Li S, Li Y, Sheng Z-H. 2021. Oligodendrocytes enhance axonal energy metabolism by deacetylation of mitochondrial proteins through transcellular delivery of SIRT2. *Neuron* **109**:3456–3472. doi:10.1016/j.neuron.2021.08.011

Coleman MP, Conforti L, Anne Buckmaster E, Tarlton A, Ewing RM, Brown MC, Lyon MF, Perry VH. 1998. An 85-kb tandem triplication in the slow Wallerian degeneration (Wld s) mouse. *Proceedings of the National Academy of Sciences* **95**:9985–9990.

Coleman MP, Höke A. 2020. Programmed axon degeneration: from mouse to mechanism to medicine. *Nature Reviews Neuroscience* **21**:183–196. doi:10.1038/s41583-020-0269-3

de Monasterio-Schrader P, Patzig J, Möbius W, Barrette B, Wagner TL, Kusch K, Edgar JM, Brophy PJ, Werner HB. 2013. Uncoupling of neuroinflammation from axonal degeneration in mice lacking the myelin protein tetraspanin-2. *GLIA* **61**:1832–1847. doi:10.1002/glia.22561

de Waegh SM, M-Y Lee V, Brady ST. 1992. Local Modulation of Neurofilament Phosphorylation, Axonal Caliber, and Slow Axonal Transport by Myelinating Schwann Cells. *Cell* **68**:451–463. doi:10.1016/0092-8674(92)90183-d

Deerinck TJ, Bushong EA, Thor A, Ellisman MH. 2010. Ncmir methods for 3D EM: A New protocol for preparation of biological specimens for serial block face scanning electron microscopy. *Microscopy* 6–8.

Dere E, Dahm L, Lu D, Hammerschmidt K, Ju A, Tantra M, Kästner A, Chowdhury K, Ehrenreich H. 2014. Heterozygous Ambra1 deficiency in mice: A genetic trait with autism-like behavior restricted to the female gender. *Frontiers in Behavioral Neuroscience* **8**. doi:10.3389/fnbeh.2014.00181

di Stefano M, Nascimento-Ferreira I, Orsomando G, Mori V, Gilley J, Brown R, Janeckova L, Vargas ME, Worrell LA, Loreto A, Tickle J, Patrick J, Webster JRM, Marangoni M, Carpi FM, Pucciarelli S, Rossi F, Meng W, Sagasti A, Ribchester RR, Magni G, Coleman MP, Conforti L. 2015. A rise in NAD precursor nicotinamide mononucleotide (NMN) after injury promotes axon degeneration. *Cell Death and Differentiation* **22**:731–742. doi:10.1038/cdd.2014.164

Dieck ST, Specht D, Strenzke N, Hida Y, Krishnamoorthy V, Schmidt KF, Inoue E, Ishizaki H, Tanaka-Okamoto M, Miyoshi J, Hagiwara A, Brandstatter JH, Löwel S, Gollisch T, Ohtsuka T, Moser T. 2012. Deletion of the presynaptic scaffold cast reduces active zone size in rod photoreceptors and impairs visual processing. *Journal of Neuroscience* **32**:12192–12203. doi:10.1523/JNEUROSCI.0752-12.2012

Dimou L, Simons M. 2017. Diversity of oligodendrocytes and their progenitors. *Current Opinion in Neurobiology* **47**:73–79. doi:10.1016/j.conb.2017.09.015

Distler U, Kuharev J, Navarro P, Levin Y, Schild H, Tenzer S. 2014. Drift time-specific collision energies enable deep-coverage data-independent acquisition proteomics. *Nature Methods* **11**:167–170. doi:10.1038/nmeth.2767

Edgar JM, McLaughlin M, Werner HB, McCulloch MC, Barrie JA, Brown A, Faichney AB, Snaidero N, Nave KA, Griffiths IR. 2009. Early ultrastructural defects of axons and axon-glia junctions in mice lacking expression of Cnp1. *GLIA* **57**:1815–1824. doi:10.1002/glia.20893

Edgar JM, McLaughlin M, Yool D, Zhang SC, Fowler JH, Montague P, Barrie JA, McCulloch MC, Duncan ID, Garbern J, Nave KA, Griffiths IR. 2004. Oligodendroglial modulation of fast axonal transport in a mouse model of hereditary spastic paraplegia. *Journal of Cell Biology* **166**:121–131. doi:10.1083/jcb.200312012

Eichel MA, Gargareta VI, D'Este E, Fledrich R, Kungl T, Buscham TJ, Lüders KA, Miracle C, Jung RB, Distler U, Kusch K, Möbius W, Hülsmann S, Tenzer S, Nave KA, Werner HB. 2020. CMTM6 expressed on the adaxonal Schwann cell surface restricts axonal diameters in peripheral nerves. *Nature Communications* **11**:4514. doi:10.1038/s41467-020-18172-7

Erwig MS, Hesse D, Jung RB, Uecker M, Kusch K, Tenzer S, Jahn O, Werner HB. 2019. Myelin: Methods for purification and proteome analysis. *Methods in Molecular Biology* **1936**:37–63. doi:10.1007/978-1-4939-9072-6_3

Essuman K, Summers DW, Sasaki Y, Mao X, DiAntonio A, Milbrandt J. 2017. The SARM1 Toll/Interleukin-1 Receptor Domain Possesses Intrinsic NAD+ Cleavage Activity that Promotes Pathological Axonal Degeneration. *Neuron* **93**:1334-1343.e5. doi:10.1016/j.neuron.2017.02.022

Fadnavis S, Batson J, Garyfallidis E. 2020. Patch2Self: Denoising Diffusion MRI with Self-Supervised Learning.

Farley FW, Soriano P, Steffen LS, Dymecki SM. 2000. Widespread Recombinase Expression Using FLPeR (Flipper) Mice. *genesis* **28**:106–110.

Fischer LR, Culver DG, Davis AA, Tennant P, Wang M, Coleman M, Asress S, Adalbert R, Alexander GM, Glass JD. 2005. The WldS gene modestly prolongs survival in the SOD1 G93A fALS mouse. *Neurobiology of Disease* **19**:293–300. doi:10.1016/j.nbd.2005.01.008

Franklin RJM, Ffrench-Constant C, Edgar JM, Smith KJ. 2012. Neuroprotection and repair in multiple sclerosis. *Nature Reviews Neurology* **8**:624–634. doi:10.1038/nrneurol.2012.200

Frühbeis C, Fröhlich D, Kuo WP, Amphornrat J, Thilemann S, Saab AS, Kirchhoff F, Möbius W, Goebbels S, Nave KA, Schneider A, Simons M, Klugmann M, Trotter J, Krämer-Albers EM. 2013. Neurotransmitter-Triggered Transfer of Exosomes Mediates Oligodendrocyte-Neuron Communication. *PLoS Biology* **11**. doi:10.1371/journal.pbio.1001604

Frühbeis C, Kuo-Elsner WP, Müller C, Barth K, Peris L, Tenzer S, Möbius W, Werner HB, Nave KA, Fröhlich D, Krämer-Albers EM. 2020. Oligodendrocytes support axonal transport and maintenance via exosome secretion. *PLoS Biology* **18**:e3000621. doi:10.1371/journal.pbio.3000621

Fujihara Y, Oji A, Kojima-Kita K, Larasati T, Ikawa M. 2018. Co-expression of sperm membrane proteins CMTM2A and CMTM2B is essential for ADAM3 localization and male fertility in mice. *Journal of Cell Science* **19**:jcs221481. doi:10.1242/jcs.221481

Fünfschilling U, Supplie LM, Mahad D, Boretius S, Saab AS, Edgar J, Brinkmann BG, Kassmann CM, Tzvetanova ID, Möbius W, Diaz F, Meijer D, Suter U, Hamprecht B, Sereda MW, Moraes CT, Frahm J, Goebbels S, Nave KA. 2012. Glycolytic oligodendrocytes maintain myelin and long-term axonal integrity. *Nature* **485**:517–521. doi:10.1038/nature11007

Garcia ML, Lobsiger CS, Shah SB, Deerinck TJ, Crum J, Young D, Ward CM, Crawford TO, Gotow T, Uchiyama Y, Ellisman MH, Calcutt NA, Cleveland DW. 2003. NF-M is an essential target for the myelin-directed “outside-in” signaling cascade that mediates radial axonal growth. *Journal of Cell Biology* **163**:1011–1020. doi:10.1083/jcb.200308159

Gargareta V-I, Reuschenbach J, Siems SB, Sun T, Piepkorn L, Mangana C, Späte E, Goebbels S, Huitinga I, Möbius W, Nave K-A, Jahn O, Werner HB. 2022. Conservation and divergence of myelin proteome and oligodendrocyte transcriptome profiles between humans and mice. *Bioarchive*. doi:10.1101/2022.01.17.476643

Garyfallidis E, Brett M, Amirbekian B, Rokem A, van der Walt S, Descoteaux M, Nimmo-Smith I. 2014. Dipy, a library for the analysis of diffusion MRI data. *Frontiers in Neuroinformatics* **8**. doi:10.3389/fninf.2014.00008

Gerber D, Pereira JA, Gerber J, Tan G, Dimitrieva S, Yángüez E, Suter U. 2021. Transcriptional profiling of mouse peripheral nerves to the single-cell level to build a sciatic nerve atlas (Snat). *eLife* **10**:e58591. doi:10.7554/ELIFE.58591

Gerdts J, Summers DW, Sasaki Y, DiAntonio A, Milbrandt J. 2013. Sarm1-mediated axon degeneration requires both SAM and TIR interactions. *Journal of Neuroscience* **33**:13569–13580. doi:10.1523/JNEUROSCI.1197-13.2013

Gibson EM, Purger D, Mount CW, Goldstein AK, Lin GL, Wood LS, Inema I, Miller SE, Bieri G, Zuchero JB, Barres BA, Woo PJ, Vogel H, Monje M. 2014. Neuronal activity promotes oligodendrogenesis and adaptive myelination in the mammalian brain. *Science* **344**. doi:10.1126/science.1252304

Gilley J, Coleman MP. 2010. Endogenous Nmnat2 Is an Essential Survival Factor for Maintenance of Healthy Axons. *PLoS Biology* **8**:e1000300. doi:10.1371/journal.pbio.1000300

Goebbels S, Wieser GL, Pieper A, Spitzer S, Weege B, Yan K, Edgar JM, Yagensky O, Wichert SP, Agarwal A, Karram K, Renier N, Tessier-Lavigne M, Rossner MJ, Káradóttir RT, Nave KA. 2017. A neuronal PI(3,4,5)P 3 -dependent program of oligodendrocyte precursor recruitment and myelination. *Nature Neuroscience* **20**:10–15. doi:10.1038/nn.4425

Gong S, Doughty M, Harbaugh CR, Cummins A, Hatten ME, Heintz N, Gerfen CR. 2007. Targeting Cre recombinase to specific neuron populations with bacterial artificial chromosome constructs. *Journal of Neuroscience* **27**:9817–9823. doi:10.1523/JNEUROSCI.2707-07.2007

Griffiths I, Klugmann M, Anderson T, Thomson C, Vouyiouklis D, Nave KA. 1998. Axonal swellings and degeneration in mice lacking the major proteolipid of myelin. *Science* **280**:1610–1613. doi:10.1126/science.280.5369.1610

Hagemeyer N, Goebbels S, Papiol S, Kästner A, Hofer S, Begemann M, Gerwig UC, Boretius S, Wieser GL, Ronnenberg A, Gurvich A, Heckers SH, Frahm J, Nave KA, Ehrenreich H. 2012. A myelin gene causative of a catatonia-depression syndrome upon aging. *EMBO Molecular Medicine* **4**:528–539. doi:10.1002/emmm.201200230

Han W, Ding P, Xu M, Wang L, Rui M, Shi S, Liu Y, Zheng Y, Chen Y, Yang T, Ma D. 2003. Identification of eight genes encoding chemokine-like factor superfamily members 1-8 (CKLFSF1-8) by in silico cloning and experimental validation. *Genomics* **81**:609–617. doi:10.1016/S0888-7543(03)00095-8

Hartline DK, Colman DR. 2007. Rapid Conduction and the Evolution of Giant Axons and Myelinated Fibers. *Current Biology* **17**:29–35. doi:10.1016/j.cub.2006.11.042

Helms G, Dathe H, Kallenberg K, Dechent P. 2008. High-resolution maps of magnetization transfer with inherent correction for RF inhomogeneity and T1 relaxation obtained from 3D FLASH MRI. *Magnetic Resonance in Medicine* **60**:1396–1407. doi:10.1002/mrm.21732

Hughes RO, Bosanac T, Mao X, Engber TM, DiAntonio A, Milbrandt J, Devraj R, Krauss R. 2021. Small Molecule SARM1 Inhibitors Recapitulate the SARM1−/− Phenotype and Allow Recovery of a Metastable Pool of Axons Fated to Degenerate. *Cell Reports* **34**:108588. doi:10.1016/j.celrep.2020.108588

Imamura H, Huynh Nhat KP, Togawa H, Saito K, Iino R, Kato-Yamada Y, Nagai T, Noji H. 2009. Visualization of ATP levels inside single living cells with fluorescence resonance energy transfer-based genetically encoded indicators. *PNAS* **106**:15651–15656.

Jaegle M, Ghazvini M, Mandemakers W, Piirsoo M, Driegen S, Levavasseur F, Raghoenath S, Grosveld F, Meijer D. 2003. The POU proteins Brn-2 and Oct-6 share important functions in Schwann cell development. *Genes and Development* **17**:1380–1391. doi:10.1101/gad.258203

Jahn O, Siems SB, Kusch K, Hesse D, Jung RB, Liepold T, Uecker M, Sun T, Werner HB. 2020. The CNS Myelin Proteome: Deep Profile and Persistence After Post-mortem Delay. *Frontiers in Cellular Neuroscience* **14**:239. doi:10.3389/fncel.2020.00239

Jäkel S, Agirre E, Mendanha Falcão A, van Bruggen D, Lee KW, Knuesel I, Malhotra D, ffrench-Constant C, Williams A, Castelo-Branco G. 2019. Altered human oligodendrocyte heterogeneity in multiple sclerosis. *Nature* **566**:543–547. doi:10.1038/s41586-019-0903-2

Jumper J, Evans R, Pritzel A, Green T, Figurnov M, Ronneberger O, Tunyasuvunakool K, Bates R, Žídek A, Potapenko A, Bridgland A, Meyer C, Kohl SAA, Ballard AJ, Cowie A, Romera-Paredes B, Nikolov S, Jain R, Adler J, Back T, Petersen S, Reiman D, Clancy E, Zielinski M, Steinegger M, Pacholska M, Berghammer T, Bodenstein S, Silver D, Vinyals O, Senior AW, Kavukcuoglu K, Kohli P, Hassabis D. 2021. Highly accurate protein structure prediction with AlphaFold. *Nature* **596**:583–589. doi:10.1038/s41586-021-03819-2

Jung M, Sommer I, Schachner M, Nave K-A. 1996. Monoclonal Antibody O10 Defines a Conformationally Sensitive Cell-Surface Epitope of Proteolipid Protein (PLP): Evidence that PLP Misfolding Underlies Dysmyelination in Mutant Mice. *The Journal of Neuroscience* **16**:7920–7929. doi:10.1523/JNEUROSCI.16-24-07920.1996

Kirkpatrick LL, Witt AS, Ross Payne H, David Shine H, Brady ST. 2001. Changes in Microtubule Stability and Density in Myelin-Deficient Shiverer Mouse CNS Axons. *Journal of Neuroscience* **7**:2288–2297. doi:10.1523/JNEUROSCI.21-07-02288.2001

Krämer-Albers EM, Bretz N, Tenzer S, Winterstein C, Möbius W, Berger H, Nave KA, Schild H, Trotter J. 2007. Oligodendrocytes secrete exosomes containing major myelin and stress-protective proteins: Trophic support for axons? *Proteomics - Clinical Applications* **1**:1446–1461. doi:10.1002/prca.200700522

Kuharev J, Navarro P, Distler U, Jahn O, Tenzer S. 2015. In-depth evaluation of software tools for data-independent acquisition based label-free quantification. *Proteomics* **15**:3140–3151. doi:10.1002/pmic.201400396

Lappe-Siefke C, Goebbels S, Gravel M, Nicksch E, Lee J, Braun PE, Griffiths IR, Navel KA. 2003. Disruption of Cnp1 uncouples oligodendroglial functions in axonal support and myelination. *Nature Genetics* **33**:366–374. doi:10.1038/ng1095

Lee S, Leach MK, Redmond SA, Chong SYC, Mellon SH, Tuck SJ, Feng ZQ, Corey JM, Chan JR. 2012. A culture system to study oligodendrocyte myelination processes using engineered nanofibers. *Nature Methods* **9**:917–922. doi:10.1038/nmeth.2105

Lee Y, Morrison BM, Li Y, Lengacher S, Farah MH, Hoffman PN, Liu Y, Tsingalia A, Jin L, Zhang PW, Pellerin L, Magistretti PJ, Rothstein JD. 2012. Oligodendroglia metabolically support axons and contribute to neurodegeneration. *Nature* **487**:443–448. doi:10.1038/nature11314

Leite SC, Sampaio P, Sousa VF, Nogueira-Rodrigues J, Pinto-Costa R, Peters LL, Brites P, Sousa MM. 2016. The Actin-Binding Protein α-Adducin Is Required for Maintaining Axon Diameter. *Cell Reports* **15**:490–498. doi:10.1016/j.celrep.2016.03.047

Leone DP, Genoud S, Atanasoski S, Grausenburger R, Berger P, Metzger D, Macklin WB, Chambon P, Suter U. 2003. Tamoxifen-inducible glia-specific Cre mice for somatic mutagenesis in oligodendrocytes and Schwann cells. *Molecular and Cellular Neuroscience* **22**:430–440. doi:10.1016/S1044-7431(03)00029-0

Li H, Guo X, Shao L, Plate M, Mo X, Wang Y, Han W. 2010. CMTM5-v1, a four-transmembrane protein, presents a secreted form released via a vesicle-mediated secretory pathway. *Biochemistry and Molecular Biology Reports* **43**:182–187. doi:10.5483/bmbrep.2010.43.3.182

Liu FJ, Liu XX, Liu X, Li T, Zhu P, Liu ZY, Xue H, Wang WJ, Yang XL, Liu J, Han WL. 2019. Integrated analyses of phenotype and quantitative proteome of CMTM4 deficient mice reveal its association with Male fertility. *Molecular and Cellular Proteomics* **18**:1070–1084. doi:10.1074/mcp.RA119.001416

Loring HS, Parelkar SS, Mondal S, Thompson PR. 2020. Identification of the first noncompetitive SARM1 inhibitors. *Bioorganic and Medicinal Chemistry* **28**:115644. doi:10.1016/j.bmc.2020.115644

Lovas G, Szilágyi N, Majtényi K, Palkovits M, Komoly S. 2000. Axonal changes in chronic demyelinated cervical spinal cord plaques. *Brain* **123**:308–317. doi:10.1093/brain/123.2.308

Lowry OH, Rosebrough NJ, Farr AL, Randall RJ. 1951. Protein measurement with the Folin phenol reagent. *The Journal of biological chemistry* **193**:265–275. doi:10.1016/s0021-9258(19)52451-6

Lüders KA, Patzig J, Simons M, Nave KA, Werner HB. 2017. Genetic dissection of oligodendroglial and neuronal Plp1 function in a novel mouse model of spastic paraplegia type 2. *GLIA* **65**:1762–1776. doi:10.1002/glia.23193

Lunn ER, Perry VH, Brown MC, Gordon' S. 1989. Absence of Wallerian Degeneration does not Hinder Regeneration in Peripheral Nerve. *European Journal of Neuroscience* **I**:27–33. doi:10.1111/j.1460-9568.1989.tb00771.x

Mack TGA, Reiner M, Beirowski B, Mi W, Emanuelli M, Wagner D, Thomson D, Gillingwater T, Court F, Conforti L, Fernando FS, Tarlton A, Andressen C, Addicks K, Magni G, Ribchester RR, Perry VH, Coleman MP. 2001. Wallerian degeneration of injured axons and synapses is delayed by a Ube4b/Nmnat chimeric gene. *Nature Neuroscience* **4**:1199–1206. doi:10.1038/nn770

Maday S, Twelvetrees AE, Moughamian AJ, Holzbaur ELF. 2014. Axonal Transport: Cargo-Specific Mechanisms of Motility and Regulation. *Neuron*. doi:10.1016/j.neuron.2014.10.019

Mei F, Lehmann-Horn K, Shen Y-AA, Rankin KA, Stebbins KJ, Lorrain DS, Pekarek K, Sagan SA, Xiao L, Teuscher C, von Bü dingen H-C, rgen Wess J, Josh Lawrence J, Green AJ, Fancy SP, Zamvil SS, Chan JR. 2016. Accelerated remyelination during inflammatory demyelination prevents axonal loss and improves functional recovery. *eLife* **5**:e18246. doi:10.7554/eLife.18246.001

Mezzadra R, Sun C, Jae LT, Gomez-Eerland R, de Vries E, Wu W, Logtenberg MEW, Slagter M, Rozeman EA, Hofland I, Broeks A, Horlings HM, Wessels LFA, Blank CU, Xiao Y, Heck AJR, Borst J, Brummelkamp TR, Schumacher TNM. 2017. Identification of CMTM6 and CMTM4 as PD-L1 protein regulators. *Nature* **549**:106–110. doi:10.1038/nature23669

Mitew S, Gobius I, Fenlon LR, McDougall SJ, Hawkes D, Xing YL, Bujalka H, Gundlach AL, Richards LJ, Kilpatrick TJ, Merson TD, Emery B. 2018. Pharmacogenetic stimulation of neuronal activity increases myelination in an axon-specific manner. *Nature Communications* **9**. doi:10.1038/s41467-017-02719-2

Mohapatra P, Shriwas O, Mohanty S, Ghosh A, Smita S, Kaushik SR, Arya R, Rath R, das Majumdar SK, Muduly DK, Raghav SK, Nanda RK, Dash R. 2021. CMTM6 drives cisplatin resistance by regulating Wnt signaling through the ENO-1/AKT/GSK3β axis. *JCI Insight* **6**. doi:10.1172/jci.insight.143643

Mukherjee C, Kling T, Russo B, Miebach K, Kess E, Schifferer M, Pedro LD, Weikert U, Fard MK, Kannaiyan N, Rossner M, Aicher ML, Goebbels S, Nave KA, Krämer-Albers EM, Schneider A,

Simons M. 2020. Oligodendrocytes Provide Antioxidant Defense Function for Neurons by Secreting Ferritin Heavy Chain. *Cell Metabolism* **32**:259-272.e10. doi:10.1016/j.cmet.2020.05.019

Nave KA, Trapp BD. 2008. Axon-glial signaling and the glial support of axon function. *Annual Review of Neuroscience* **31**:535–561. doi:10.1146/annurev.neuro.30.051606.094309

Nave K-A, Werner HB. 2021. Ensheathment and Myelination of Axons: Evolution of Glial Functions. *Annual Review of Neuroscience* **44**:197–219. doi:10.1146/annurev-neuro-100120

Nave KA, Werner HB. 2014. Myelination of the nervous system: Mechanisms and functions. *Annual Review of Cell and Developmental Biology* **30**:503–533. doi:10.1146/annurev-cellbio-100913-013101

Osterloh JM, Yang J, Rooney TM, Fox AN, Adalbert R, Powell EH, Sheehan AE, Avery MA, Hackett R, Logan MA, MacDonald JM, Ziegenfuss JS, Milde S, Hou YJ, Nathan C, Ding A, Brown RH, Conforti L, Coleman M, Tessier-Lavigne M, Züchner S, Freeman MR. 2012. dSarm/Sarm1 is required for activation of an injury-induced axon death pathway. *Science* **337**:481–484. doi:10.1126/science.1223899

Ou X, Sun SW, Liang HF, Song SK, Gochberg DF. 2009. Quantitative magnetization transfer measured pool-size ratio reflects optic nerve myelin content in Ex vivo mice. *Magnetic Resonance in Medicine* **61**:364–371. doi:10.1002/mrm.21850

Palandri A, Salvador VR, Wojnacki J, Vivinetto AL, Schnaar RL, Lopez PHH. 2015. Myelin-associated glycoprotein modulates apoptosis of motoneurons during early postnatal development via NgR/p75 NTR receptor-mediated activation of RhoA signaling pathways. *Cell Death and Disease* **6**. doi:10.1038/cddis.2015.228

Patzig J, Erwig MS, Tenzer S, Kusch K, Dibaj P, Möbius W, Goebbels S, Schaeren-Wiemers N, Nave KA, Werner HB. 2016. Septin/anillin filaments scaffold central nervous system myelin to accelerate nerve conduction. *eLife* **5**:e17119. doi:10.7554/eLife.17119.001

Patzig J, Jahn O, Tenzer S, Wichert SP, de Monasterio-Schrader P, Rosfa S, Kuharev J, Yan K, Bormuth I, Bremer J, Aguzzi A, Orfaniotou F, Hesse D, Schwab MH, Möbius W, Nave KA, Werner HB. 2011. Quantitative and integrative proteome analysis of peripheral nerve myelin identifies novel myelin proteins and candidate neuropathy loci. *Journal of Neuroscience* **31**:16369–16386. doi:10.1523/JNEUROSCI.4016-11.2011

Peters OM, Lewis EA, Osterloh JM, Weiss A, Salameh JS, Metterville J, Brown RH, Freeman MR. 2018. Loss of Sarm1 does not suppress motor neuron degeneration in the SOD1G93A mouse model of amyotrophic lateral sclerosis. *Human Molecular Genetics* **27**:3761–3771. doi:10.1093/hmg/ddy260

Philips T, Mironova YA, Jouroukhin Y, Chew J, Vidensky S, Farah MH, Pletnikov M v., Bergles DE, Morrison BM, Rothstein JD. 2021. MCT1 Deletion in Oligodendrocyte Lineage Cells Causes Late-Onset Hypomyelination and Axonal Degeneration. *Cell Reports* **34**:108610. doi:10.1016/j.celrep.2020.108610

Poliak S, Peles E. 2003. The local differentiation of myelinated axons at nodes of ranvier. *Nature Reviews Neuroscience*. doi:10.1038/nrn1253

Popko B, Puckett C, Lai E, David Shine H, Readhead C, Takahashi N, Hunt SW, Sidman RL, Hood L. 1987. Myelin Deficient Mice: Expression of Myelin Basic Protein and Generation of Mice with Varying Levels of Myelin. *Cell* **48**:713–721. doi:10.1016/0092-8674(87)90249-2

Provencher SW. 1993. Estimation of Metabolite Concentrations from Localized in Vivo Proton NMR Spectra. *Magnetic Resonance in Medicine* **30**:672–679. doi:10.1002/mrm.1910300604

Redmond SA, Mei F, Eshed-Eisenbach Y, Osso LA, Leshkowitz D, Shen YAA, Kay JN, Aurrand-Lions M, Lyons DA, Peles E, Chan JR. 2016. Somatodendritic Expression of JAM2 Inhibits Oligodendrocyte Myelination. *Neuron* **91**:824–836. doi:10.1016/j.neuron.2016.07.021

Ridder WH, Nusinowitz S. 2006. The visual evoked potential in the mouse - Origins and response characteristics. *Vision Research* **46**:902–913. doi:10.1016/j.visres.2005.09.006

Roach A, Takahashi N, Pravtcheva D, Ruddle F, Hood L. 1985. Chromosomal Mapping of Mouse Myelin Basic Protein Gene and Structure and Transcription of the Partially Deleted Gene in Shiverer Mutant Mice. *Cell* **42**:149–155. doi:10.1016/s0092-8674(85)80110-0

Rosenbluth J. 1980. Central Myelin in the Mouse Mutant Shiverer. *The Journal of Comparative Neurology* **194**:639–648. doi:10.1002/cne.901940310

Saab AS, Tzvetavona ID, Trevisiol A, Baltan S, Dibaj P, Kusch K, Möbius W, Goetze B, Jahn HM, Huang W, Steffens H, Schomburg ED, Pérez-Samartín A, Pérez-Cerdá F, Bakhtiari D, Matute C, Löwel S, Griesinger C, Hirrlinger J, Kirchhoff F, Nave KA. 2016. Oligodendroglial NMDA Receptors Regulate Glucose Import and Axonal Energy Metabolism. *Neuron* **91**:119–132. doi:10.1016/j.neuron.2016.05.016

Saiki RK, Gelfand DH, Stoffel S, Scharf SJ, Higuchi R, Horn GT, Mullis KB, Ehrlich HA. 1988. Primer-Directed Enzymatic Amplification of DNA with a Termostable DNA Polymerase. *Science* **239**:487–491. doi:10.1126/science.2448875

Salzer JL. 2015. Schwann cell myelination. *Cold Spring Harbor Perspectives in Biology* **7**. doi:10.1101/cshperspect.a020529

Schindelin J, Arganda-Carreras I, Frise E, Kaynig V, Longair M, Pietzsch T, Preibisch S, Rueden C, Saalfeld S, Schmid B, Tinevez JY, White DJ, Hartenstein V, Eliceiri K, Tomancak P, Cardona A. 2012. Fiji: An open-source platform for biological-image analysis. *Nature Methods* **9**:676–682. doi:10.1038/nmeth.2019

Schmandke Antonio, Schmandke Andre, Schwab ME. 2014. Nogo-A: Multiple roles in CNS development, maintenance, and disease. *Neuroscientist*. doi:10.1177/1073858413516800

Shao L, Cui Y, Li H, Liu Y, Zhao H, Wang Y, Zhang Y, Ka MN, Han W, Ma D, Tao Q. 2007. CMTM5 exhibits tumor suppressor activities and is frequently silenced by methylation in carcinoma cell lines. *Clinical Cancer Research* **13**:5756–5762. doi:10.1158/1078-0432.CCR-06-3082

Siems SB, Jahn O, Eichel MA, Kannaiyan N, Wu LMN, Sherman DL, Kusch K, Hesse D, Jung RB, Fledrich R, Sereda MW, Rossner MJ, Brophy PJ, Werner HB. 2020. Proteome profile of peripheral myelin in healthy mice and in a neuropathy model. *eLife* **9**:e51406. doi:10.7554/eLife.51406

Silva JC, Gorenstein M v., Li GZ, Vissers JPC, Geromanos SJ. 2006. Absolute quantification of proteins by LCMSE: A virtue of parallel MS acquisition. *Molecular and Cellular Proteomics* **5**:144–156. doi:10.1074/mcp.M500230-MCP200

Simons M, Nave KA. 2016. Oligodendrocytes: Myelination and axonal support. *Cold Spring Harbor Perspectives in Biology* **8**. doi:10.1101/cshperspect.a020479

Stadelmann C, Timmler S, Barrantes-Freer A, Simons M. 2019. Myelin in the Central Nervous System: Structure, Function, and Pathology. *Physiol Rev* **99**:1381–1431. doi:10.1152/physrev.00031.2018.-Oligodendro

Steyer AM, Ruhwedel T, Nardis C, Werner HB, Nave KA, Möbius W. 2020. Pathology of myelinated axons in the PLP-deficient mouse model of spastic paraplegia type 2 revealed by volume imaging using focused ion beam-scanning electron microscopy. *Journal of Structural Biology* **210**:107492. doi:10.1016/j.jsb.2020.107492

Tasaki I. 1939. The electro-saltatory transmission of the nerve impulse and the effect of narcosis upon the nerve fiber. *The American Journal of Physiology* **127**:211–227. doi:10.1152/AJPLEGACY.1939.127.2.211

Thakurela S, Garding A, Jung RB, Müller C, Goebbels S, White R, Werner HB, Tiwari VK. 2016. The transcriptome of mouse central nervous system myelin. *Scientific Reports* **6**:1–12. doi:10.1038/srep25828

Timotius IK, Bieler L, Couillard-Despres S, Sandner B, Garcia-Ovejero D, Labombarda F, Estrada V, Müller HW, Winkler J, Klucken J, Eskofier B, Weidner N, Puttagunta R. 2021. Combination of defined catwalk gait parameters for predictive locomotion recovery in experimental spinal cord injury rat models. *eNeuro* **8**:1–14. doi:10.1523/ENEURO.0497-20.2021

Trevisiol A, Kusch K, Steyer AM, Gregor I, Nardis C, Winkler U, Köhler S, Restrepo A, Möbius W, Werner HB, Nave KA, Hirrlinger J. 2020. Structural myelin defects are associated with low axonal ATP levels but rapid recovery from energy deprivation in a mouse model of spastic paraplegia. *PLoS Biology* **18**:e3000943. doi:10.1371/journal.pbio.3000943

Trevisiol A, Saab AS, Winkler U, Marx G, Imamura H, Mö Bius W, Kusch K, Nave K-A, Hirrlinger J. 2017. Monitoring ATP dynamics in electrically active white matter tracts. *eLife* **6**:e24241. doi:10.7554/eLife.24241.001

Uschkureit T, Spörkel O, Stracke J, Bü H, Stoffel W. 2000. Early Onset of Axonal Degeneration in Double (plp/mag/) and Hypomyelinosis in Triple (plp/mbp/mag/) Mutant Mice. *The Journal of Neuroscience* **20**:5225–5233. doi:10.1523/JNEUROSCI.20-14-05225.2000

van Bruggen D, Agirre E, Castelo-Branco G. 2017. Single-cell transcriptomic analysis of oligodendrocyte lineage cells. *Current Opinion in Neurobiology*. doi:10.1016/j.conb.2017.10.005

Wang J, Zhai Q, Chen Y, Lin E, Gu W, McBurney MW, He Z. 2005. A local mechanism mediates NAD-dependent protection of axon degeneration. *Journal of Cell Biology* **170**:349–355. doi:10.1083/jcb.200504028

Weil MT, Heibeck S, Töpperwien M, Tom Dieck S, Ruhwedel T, Salditt T, Rodicio MC, Morgan JR, Nave KA, Möbius W, Werner HB. 2018. Axonal ensheathment in the nervous system of lamprey: Implications for the evolution of myelinating glia. *Journal of Neuroscience* **38**:6586–6596. doi:10.1523/JNEUROSCI.1034-18.2018

Wieser GL, Gerwig UC, Adamcio B, Barrette B, Nave KA, Ehrenreich H, Goebbels S. 2013. Neuroinflammation in white matter tracts of Cnp1 mutant mice amplified by a minor brain injury. *GLIA* **61**:869–880. doi:10.1002/glia.22480

Williams PA, Harder JM, Foxworth NE, Cardozo BH, Cochran KE, John SWM. 2017. Nicotinamide and WLDS act together to prevent neurodegeneration in glaucoma. *Frontiers in Neuroscience* **11**. doi:10.3389/fnins.2017.00232

Williamson JM, Lyons DA. 2018. Myelin dynamics throughout life: An ever-changing landscape? *Frontiers in Cellular Neuroscience* **12**. doi:10.3389/fncel.2018.00424

Wolf NI, ffrench-Constant C, van der Knaap MS. 2021. Hypomyelinating leukodystrophies — unravelling myelin biology. *Nature Reviews Neurology* **17**:88–103. doi:10.1038/s41582-020-00432-1

Xiao Y, Yuan Y, Zhang Y, Li J, Liu Z, Zhang X, Sheng Z, Xu T, Wang X. 2015. CMTM5 is reduced in prostate cancer and inhibits cancer cell growth in vitro and in vivo. *Clinical and Translational Oncology* **17**:431–437. doi:10.1007/s12094-014-1253-z

Yin X, Crawford TO, Griffin JW, Tu P, M-Y Lee V, Li C, Roder J, Trapp BD. 1998. Myelin-Associated Glycoprotein Is a Myelin Signal that Modulates the Caliber of Myelinated Axons. doi:10.1523/JNEUROSCI.18-06-01953.1998

Yong Y, Gamage K, Cheng I, Barford K, Spano A, Winckler B, Deppmann C. 2019. p75NTR and DR6 regulate distinct phases of axon degeneration demarcated by spheroid rupture. *Journal of Neuroscience* **39**:9503–9520. doi:10.1523/JNEUROSCI.1867-19.2019

Yong Y, Gamage K, Cushman C, Spano A, Deppmann C. 2020. Regulation of degenerative spheroids after injury. *Scientific Reports* **10**. doi:10.1038/s41598-020-71906-x

Yuan Y, Sheng Z, Liu Z, Zhang X, Xiao Y, Xie J, Zhang Y, Xu T. 2020. CMTM5-v1 inhibits cell proliferation and migration by downregulating oncogenic EGFR signaling in prostate cancer cells. *Journal of Cancer* **11**:3762–3770. doi:10.7150/jca.42314

Zhang Y, Chen K, Sloan SA, Bennett ML, Scholze AR, O'Keeffe S, Phatnani HP, Guarnieri P, Caneda C, Ruderisch N, Deng S, Liddelow SA, Zhang C, Daneman R, Maniatis T, Barres BA, Wu JQ. 2014. An RNA-sequencing transcriptome and splicing database of glia, neurons, and vascular cells of the cerebral cortex. *Journal of Neuroscience* **34**:11929–11947. doi:10.1523/JNEUROSCI.1860-14.2014

Zheng Y, Wang C, Song A, Jiang F, Zhou J, Li G, Zhang W, Ye J, Ding X, Du Y, Zhang H, Wu H, Song X, Wu Y. 2020. CMTM6 promotes cell proliferation and invasion in oral squamous cell carcinoma by interacting with NRP1. *Am J Cancer Res* **10**:1691–1709.

Zhou Y, Song WM, Andhey PS, Swain A, Levy T, Miller KR, Poliani PL, Cominelli M, Grover S, Gilfillan S, Cella M, Ulland TK, Zaitsev K, Miyashita A, Ikeuchi T, Sainouchi M, Kakita A, Bennett DA, Schneider JA, Nichols MR, Beausoleil SA, Ulrich JD, Holtzman DM, Artyomov MN, Colonna M. 2020. Human and mouse single-nucleus transcriptomics reveal TREM2-dependent and TREM2-independent cellular responses in Alzheimer's disease. *Nature Medicine* **26**:131–142. doi:10.1038/s41591-019-0695-9

Zou Y, Wang A, Huang L, Zhu X, Hu Q, Zhang Y, Chen X, Li F, Wang Q, Wang H, Liu R, Zuo F, Li T, Yao J, Qian Y, Shi M, Yue X, Chen W, Zhang Z, Wang C, Zhou Y, Zhu L, Ju Z, Loscalzo J, Yang Y, Zhao Y. 2020. Illuminating NAD+ Metabolism in Live Cells and In Vivo Using a Genetically Encoded Fluorescent Sensor. *Developmental Cell* **53**:240-252.e7. doi:10.1016/j.devcel.2020.02.017